

Simulation of scanning tunneling microscopy from first principles

by

Gábor Mándi

Doctoral Thesis

presented to the Doctoral School of Physics of the
Budapest University of Technology and Economics
in fulfillment of the requirements for the degree of

Doctor of Philosophy in Physics

Supervisor:

Dr. Krisztián Palotás

senior research fellow

Institute for Solid State Physics and Optics
Wigner Research Center for Physics, Budapest

research associate professor

Department of Theoretical Physics
Budapest University of Technology and Economics



2020

“In loving memory of my Mother”

Contents

Acknowledgment	iii
1 Introduction	1
2 Theory of STM	5
2.1 Standard and earlier theories	6
2.1.1 Bardeen’s method	6
2.1.1.1 Spin-polarized current	8
2.1.2 Tersoff-Hamann model	10
2.1.2.1 Spin-polarized current	11
2.1.3 Chen’s method	12
2.1.4 Atom superposition method	13
2.1.4.1 Electrostatics of the transition	14
2.1.4.2 Spin-polarized current	16
2.2 New developments	16
2.2.1 Orbital-dependent 3D-WKB	16
2.2.1.1 Tip rotations	19
2.2.2 Revised Chen’s method	21
2.2.2.1 Tip orbital interference	23
2.2.2.2 Plane-wave expansion	24
2.2.2.3 Weighting coefficients	24
2.2.2.4 Tip rotations	27
3 3D–WKB results	29
3.1 W(110)	30
3.1.1 Computational details	30
3.1.2 Convergence properties	32

3.1.3	Orbital contributions: current histograms	34
3.1.4	Contrast inversion	35
3.1.5	Comparison to other methods	39
3.1.6	Computational efficiency	42
3.1.7	The effect of arbitrary tip-orientation	43
3.2	Fe(110)	51
3.2.1	Computational details	52
3.2.2	Electronic structure and current histograms	55
3.2.3	Contrast inversion	57
3.2.4	Simulated SP-STM images	63
3.3	HOPG	65
3.3.1	Computational details	66
3.3.2	Relative brightness maps	68
3.3.3	Comparison between 3D-WKB and Bardeen methods	69
3.3.4	Comparison between simulations and experiment	74
3.3.5	Simulated STM images	76
3.4	Tip orientation in STM	79
3.4.1	Method	81
3.4.2	Correlation analysis	83
4	bSKAN-Chen results	93
4.1	Computational details	95
4.2	Graphene – N	96
4.2.1	Comparison of simulation methods	96
4.2.2	The effect of strain	99
4.2.3	The effect of tip rotation	100
4.3	AgMn ₂ H	102
4.3.1	The effect of temperature	105
5	Summary, concluding remarks	107
5.1	Summary	107
5.2	Outlook	111
5.3	Thesis points	112
	Bibliography	115

Acknowledgment

First and foremost, I would like to express my gratitude to my supervisor, Dr. Krisztián Palotás for his guidance, support and patience throughout all these years. I consider our work together a very successful and fruitful collaboration.

I am very thankful to my co-authors for their contribution to my research. To Gilberto Teobaldi for providing substantial experimental and simulational data to my research and to Norbert Nagy for drawing our attention to the interesting topic of arbitrary STM-tip orientation and for his useful comments regarding this thesis.

Furthermore, I am grateful to the Department of Theoretical Physics for providing the conditions of my research and to the staff of the Faculty of Natural Sciences, especially to Mari Vida and Tünde Gyulai, whose kindness and helpfulness I always admired and their work made my and many other students' life much easier.

I would like to thank my fellow PhD students and to my friends for their indirect but huge contribution to this thesis. They set an example for me as a researcher and also as great human beings. Their kind words, encouragement and support meant a lot to me.

Last but not least I would like to thank my family, my parents and my sister for their love, encouragement and support, and for literally everything.

Chapter 1

Introduction

Scanning tunneling microscopy (STM) has been developed in the early 1980's based on the quantum-mechanical electron tunneling principle. Topographies of (110)-oriented surface reconstructions and monoatomic steps of CaIrSn_4 and Au were first reported in atomic resolution [1]. This development revolutionized the microscopy techniques of that time, and quickly resulted in a (half) Nobel Prize in Physics awarded to Gerd Binnig (25%) and Heinrich Rohrer (25%) for the design of the STM in 1986. This scanning probe technique has clearly contributed to the rapid development of nanoscience and nanotechnology in the last 35 years, and has been actively used in many subfields of surface science to study a wide spectrum of materials' surfaces. Recent applications are concerning both physics and chemistry, and are ranging from studying complex topological spin states in magnetic surfaces and thin films with spin-polarized STM [2, 3, 4] for the purpose of the development of energy-efficient ultra-high magnetic data storage technologies to surface chemistry for investigating molecular and supramolecular structures [5], and even chemical reactions in the field of catalysis [6, 7], which is relevant for energy-efficient „green” industry-scale production of precious chemicals, keeping in mind the sustainability and environmental issues humanity is facing nowadays. The role of the STM in these studies is vital.

Figure 1.0.1 illustrates the setup and basic operational principle of a typical STM device. An atomically sharp tip attached to a piezoelectric tube is moved above a conducting or semiconducting sample surface by piezoelectric electrodes. If the tip apex is close enough to the surface (≤ 1 nm distance) then a tunneling current starts to flow at a pre-set tunneling (bias) voltage. By moving the tip adjusting the control voltages for the piezo tube, sample surfaces of interest can

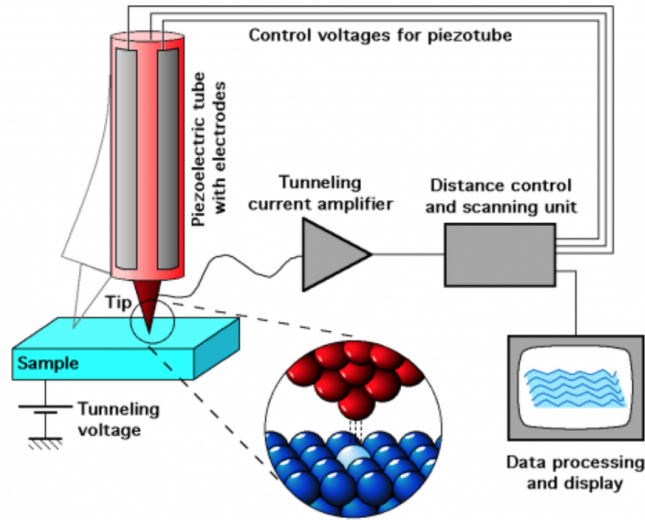


Figure 1.0.1: Schematic view of an STM device. Adapted from: Michael Schmid, TU Vienna, Austria. [https://www.iap.tuwien.ac.at/www/surface/stm_gallery/stm_schematic].

be scanned, and high-resolution topographic imaging can be achieved with ~ 1 Å lateral and ~ 0.1 Å vertical resolution. An atomically sharp tip and vibration-free environment are necessary for achieving a good resolution down to the atomic scale. Depending on the operational mode, constant height (the tip is scanning in a parallel plane above the surface) or constant current images can be recorded and analyzed. For the latter, after a proper amplification of the tunneling current, a feedback loop (distance control and scanning unit) is utilized to vertically move the tip keeping the constant current value above different lateral positions of the surface, thus the surface topography can be obtained after data processing and display. Note that the STM can operate under ultra-high vacuum conditions and at low temperature to capture exotic physical effects, but operation at ambient conditions or at higher temperatures in open air or at solid-liquid interfaces is also possible thanks to the developments of the last decades. It is important to mention that the STM can not only image but also manipulate surface structures with atomic precision [8, 9, 10, 11]. This latter functionality will definitely be used in future applications, for example in the design of a class of quantum computers.

An important point is that the STM does not image the geometric structure of the surface, but the combination of the atomic geometry of the sample and the convolution of electron densities of states of the sample and the scanning tip. This, together with tip-surface interactions can highly complicate the interpretation of experimental STM images. For such reasons, theoretical modeling of

the STM is highly required, which is the main topic of the present dissertation. The focus is on the development and implementation of computationally efficient electron tunneling theories capable of simulating high-resolution STM based on first-principles electronic structure methods (for example density-functional-theory (DFT)), and the tests on various surface structures to validate the newly developed STM methods.

The dissertation is organized as follows. Chapter 2 describes the theoretical models of STM, starting with traditional methods (Section 2.1), followed by new scientific results in the field (Section 2.2). During the PhD course, two different methods have been developed (Sections 2.2.1 and 2.2.2), and corresponding results are presented in Chapters 3 and 4, respectively, where the details of the electronic structure calculations of each surface system (and STM tips) are described. In particular, body centered cubic (bcc) flat metal surfaces were considered, where the electron orbitals involved in the tunneling were studied in great details concerning the STM contrast inversion and the effect of asymmetric tips on the STM images for the nonmagnetic W(110) surface (Section 3.1), and the interplay of electron orbitals and spin-polarized electronic structure on the STM contrast of the magnetic Fe(110) surface (Section 3.2). Since highly oriented pyrolytic graphite (HOPG) is very important for the calibration of STM, its STM contrast stability is analyzed in Section 3.3, followed by a statistical analysis taking a HOPG sample in combination with tungsten tips, where information on the local tip apex geometry and orientation can be obtained introducing a correlation analysis method to quantify the level of agreement between different simulation methods and real STM experiments (Section 3.4). The presently only existing method that can quantify tip-orbital interference contributions to the tunneling current is introduced in Section 2.2.2, and the effect of the tip-orbital interference and other factors (strain, tip rotation, and temperature) on the STM contrast are investigated in two sample surface structures: nitrogen-doped graphene (Section 4.2) and a Mn_2H molecule on the Ag(111) surface (Section 4.3). Finally, a summary of the dissertation and an outlook are given in Chapter 5, where the thesis points are also stated summarizing the new scientific results in connection to published works in scientific journals. The dissertation finishes with the used list of scientific literature.

Chapter 2

Theory of STM

In this chapter we briefly describe the basic theories of electron tunneling along with their assumptions, limitations and extensions. The tunneling junction problem was first described by Bardeen in the early '60s [12]. His model is based on first order time-dependent perturbation theory and serves as the basic theory of tunneling which was extended, modified or simplified several times through the years. The first notable application of Bardeen's theory was Tersoff and Hamann's work after the invention of STM [13, 14] explaining the atomic resolution achieved in STM experiments. Later, Chen developed his famous derivative rule explaining the unusually large corrugation of some surfaces and highlighted the crucial role of the tip-orbital character in the tunneling process [15]. As an extension of the popular and widely used Tersoff-Hamann model – motivated by Chen's work – Palotás *et.al.* developed the so called 3D-WKB model, which incorporates the orbital characters of the tip and sample atoms as well [P1].

There are tunneling models that are not related to Bardeen's work but based on multiple electron scattering theory and capable of modelling electron transport not only in the low conductance (tunneling) regime, but in the high conductance (contact) regime as well [16, 17, 18]. Such theories are out of the scope of this work, we focus only on theories that are directly or indirectly originated from Bardeen's theory, therefore have common limitations and using common assumptions. These have to be emphasized and kept in mind when any conclusion is made based upon a simulational or theoretical work. These assumptions are the following [19]:

1. *The electron tunneling is treated as a one-particle process.*

Any interaction between electrons is neglected during tunneling.

2. *The interaction of tip and sample regarding the electronic states is not taken into account.*

This means that the tip and sample electronic structure can be calculated separately, and occupation probabilities are independent of each other. If the tip-sample distance is large enough (*e.g.* larger than 3.5 - 4 Å), then this assumption should be valid.

3. *The tunneling is assumed to be elastic.*

No energy loss is considered due to interaction between electrons and quasi-particles *e.g.* plasmons, phonons, spin-excitations. Theories that deal with such effects can be found in the following works: [20, 21, 22, 23, 24, 25].

To avoid surface and tip instabilities and to achieve atomic resolution, STM experiments are usually performed at low temperature and low bias voltage with typical tip-sample distance of 4 – 14 Å. Hence any tip-sample interaction or multiple scattering effect can be neglected and the presented assumptions are valid in an ordinary STM experiment.

2.1 Standard and earlier theories

2.1.1 Bardeen's method

We introduce the basics of Bardeen's method and some elementary formulas that we rely on in the following chapters. Besides Bardeen's original work [12], there are some very detailed papers with rigorous derivations on this topic which can be recommended, *e.g.* Refs. [19, 26].

Starting from two separate electrodes (S – sample and T – tip) which are far apart, the unperturbed wavefunctions satisfy the time dependent Schrödinger equations

$$\left(-\frac{\hbar^2}{2m}\nabla^2 + U^S\right)\psi = i\hbar\frac{\partial\psi}{\partial t} \quad \left(-\frac{\hbar^2}{2m}\nabla^2 + U^T\right)\chi = i\hbar\frac{\partial\chi}{\partial t}, \quad (2.1.1)$$

while the time independent parts of the wavefunctions, denoted by ψ_μ for the

sample and χ_ν for the tip, satisfy the time-independent Schrödinger equations:

$$\left(-\frac{\hbar^2}{2m}\nabla^2 + U^S\right)\psi_\mu = E_\mu^S\psi_\mu \quad \left(-\frac{\hbar^2}{2m}\nabla^2 + U^T\right)\chi_\nu = E_\nu^T\chi_\nu. \quad (2.1.2)$$

U^S and U^T are the potential function, E_μ^S and E_ν^T are the eigenenergies of sample and the tip, respectively. When the sample is approached by the tip, the combined system can be described with Ψ , satisfying the Schrödinger equation containing the full potential $U^S + U^T$:

$$\left(-\frac{\hbar^2}{2m}\nabla^2 + U^S + U^T\right)\Psi = i\hbar\frac{\partial\Psi}{\partial t} \quad (2.1.3)$$

The process of tunneling of an electron (from the sample to the tip) can be interpreted as the transition from ψ_μ to χ_ν with $P_{\mu\nu}$ scattering rate (transitional probability over unit time). Assuming that the sample is approached slowly, and therefore the tip's potential is turned on adiabatically, one can apply first order time-dependent perturbation theory and arrive at Fermi's Golden Rule:

$$P_{\mu\nu} = \frac{2\pi}{\hbar}|M_{\mu\nu}|^2\delta(E_\mu - E_\nu). \quad (2.1.4)$$

$M_{\mu\nu} = \langle\chi_\nu|U^T|\psi_\mu\rangle$ is the matrix element between two single electron states involved in the tunneling, while the energy conservation is ensured by the Dirac-delta. The contribution of this single transition to the tunneling current can be calculated as $eP_{\mu\nu}$, where e is the elementary charge. The total current is simply the sum of all transitions between the occupied states of the sample and the unoccupied states of the tip. The distribution of the occupied states at finite temperature T is described by the Fermi-Dirac distribution $f(E)$ while the unoccupied states are described by $1 - f(E)$. Applying a finite bias voltage V the Fermi level of the tip (E_F^T) is shifted by eV with respect to the Fermi level of the sample (E_F^S). The net tunneling current is simply the difference of the total current from the sample to the tip ($I_{S\rightarrow T}$) and the current from the tip to the sample ($I_{T\rightarrow S}$). Assuming spin-independent tunneling, we have to account for the two possible spin states as well, introducing a factor of 2 in the current

formula:

$$\begin{aligned} I &= I_{S \rightarrow T} - I_{T \rightarrow S} = & (2.1.5) \\ &= \frac{4\pi e}{\hbar} \sum_{\mu\nu} [f(E_\mu - E_F^S) - f(E_\nu - E_F^T)] |M_{\mu\nu}|^2 \delta(E_\nu - E_\mu - eV). \end{aligned}$$

In Bardeen's approach the matrix element is approximated with an integral over the \mathcal{S} separation surface between the sample and the tip [12]:

$$M_{\mu\nu} = -\frac{\hbar^2}{2m} \int_{\mathcal{S}} (\chi_\nu^* \nabla \psi_\mu - \psi_\mu \nabla \chi_\nu^*) \mathbf{dS} \quad (2.1.6)$$

which can be interpreted as the overlap of the wavefunctions ψ_μ and χ_ν .

Assuming a continuous spectrum of states for both sample and tip, the discrete sum can be replaced by an integral introducing the density of states (DOS) of the tip $n^T(E)$ and of the sample $n^S(E)$:

$$\begin{aligned} I &= \frac{4\pi e}{\hbar} \int [f(E_F^T + E - eV) - f(E_F^S + E)] \times & (2.1.7) \\ &\times n^S(E_F^S + E) n^T(E_F^T + E - eV) |M(E_F^S + E, E_F^T + E - eV)|^2 dE. \end{aligned}$$

At low temperature the Fermi-functions become Heaviside functions and the energy integral has to be evaluated for a finite energy window determined by the bias voltage:

$$I = \frac{4\pi e}{\hbar} \int_0^{eV} n^S(E_F^S + E) n^T(E_F^T + E - eV) |M(E_F^S + E, E_F^T + E - eV)|^2 dE. \quad (2.1.8)$$

2.1.1.1 Spin-polarized current

If we want to extend Bardeen's formalism to include the spin dependence and calculate spin-polarized currents, it is necessary to describe the wavefunctions as two-component spinors:

$$\psi_{\mu\sigma} = \begin{pmatrix} \psi_{\mu\uparrow} \\ \psi_{\mu\downarrow} \end{pmatrix} \quad \chi_{\nu\sigma} = \begin{pmatrix} \chi_{\nu\uparrow} \\ \chi_{\nu\downarrow} \end{pmatrix}. \quad (2.1.9)$$

The potentials are described by two-by-two matrices and both stationary wavefunctions satisfy the Pauli-Schrödinger equations:

$$\left[-\frac{\hbar^2}{2m} \nabla^2 + \begin{pmatrix} U_{\uparrow\uparrow}^S & U_{\uparrow\downarrow}^S \\ U_{\downarrow\uparrow}^S & U_{\downarrow\downarrow}^S \end{pmatrix} \right] \begin{pmatrix} \psi_{\mu\uparrow} \\ \psi_{\mu\downarrow} \end{pmatrix} = E_\mu^S \begin{pmatrix} \psi_{\mu\uparrow} \\ \psi_{\mu\downarrow} \end{pmatrix} \quad (2.1.10)$$

$$\left[-\frac{\hbar^2}{2m} \nabla^2 + \begin{pmatrix} U_{\uparrow\uparrow}^T & U_{\uparrow\downarrow}^T \\ U_{\downarrow\uparrow}^T & U_{\downarrow\downarrow}^T \end{pmatrix} \right] \begin{pmatrix} \chi_{\nu\uparrow} \\ \chi_{\nu\downarrow} \end{pmatrix} = E_\nu^T \begin{pmatrix} \chi_{\nu\uparrow} \\ \chi_{\nu\downarrow} \end{pmatrix} \quad (2.1.11)$$

The matrix elements also become spin dependent

$$M_{\mu\nu\sigma\sigma'} = \langle \chi_{\nu\sigma'} | U_{\sigma\sigma'}^T | \psi_{\mu\sigma} \rangle, \quad (2.1.12)$$

and the tunneling current can be calculated using the previous formalism, resulting in

$$I = \frac{2\pi e}{\hbar} \sum_{\mu\nu} \sum_{\sigma\sigma'} [f(E_\mu - E_F^S) - f(E_\nu - E_F^T)] |M_{\mu\nu\sigma\sigma'}|^2 \delta(E_\nu - E_\mu - eV). \quad (2.1.13)$$

Similarly to (2.1.8), in the low temperature limit the tunneling current is

$$I = \frac{2\pi e}{\hbar} \sum_{\sigma\sigma'} \int_0^{eV} n_\sigma^S(E_F^S + E) n_{\sigma'}^T(E_F^T + E - eV) \times \quad (2.1.14)$$

$$\times |M_{\sigma\sigma'}(E_F^S + E, E_F^T + E - eV)|^2 dE,$$

where the spin-dependent DOS of the sample n_σ^S and of the tip $n_{\sigma'}^T$ have been introduced.

The method requires the exact electronic structure of tip and sample and the explicit form of the wavefunctions as well. In principle it is possible to calculate them for both systems independently with available *ab initio* methods, *e.g.* using density functional theory (DFT), but STM image simulations are still considered to be computationally heavy tasks. Besides, the tip's geometry is generally unknown which complicates the task of simulating the STM tip. To overcome this drawback, several simplifications of the model has been introduced.

2.1.2 Tersoff-Hamann model

Two years after the invention of STM, Tersoff and Hamann proposed their model of tunneling based on Bardeen's theory [13, 14]. The idea behind this approach is to simplify the tip's electronic structure and geometry as much as possible. Therefore the STM tip is modeled as a locally spherical potential well centered at the tip position \mathbf{r}_T . In the (2.1.6) formula of the matrix elements, the separation surface lies between the sample and the tip, far enough from both that the tip wavefunction satisfies the vacuum Schrödinger equation:

$$-\frac{\hbar^2}{2m}\nabla^2\chi_\nu = -\phi\chi_\nu, \quad (2.1.15)$$

where ϕ is the work function of the tip. Assuming a spherical wavefunction (s -wave), the regular solution is given by the modified Bessel function of the second kind:

$$\chi_\nu(\mathbf{r} - \mathbf{r}_T) = Ck_0(\kappa|\mathbf{r} - \mathbf{r}_T|) = C\frac{e^{-\kappa|\mathbf{r} - \mathbf{r}_T|}}{\kappa|\mathbf{r} - \mathbf{r}_T|}, \quad (2.1.16)$$

where $\kappa = \sqrt{2m\phi}/\hbar$ is the vacuum decay and C is a normalization constant. Substituting (2.1.16) into (2.1.6), the matrix element becomes

$$M_{\mu\nu} = \frac{2\pi C\hbar^2}{m\kappa}\psi_\mu(\mathbf{r}_T). \quad (2.1.17)$$

Using (2.1.5) in the limit of low temperature the tunneling current at tip position \mathbf{r}_T is:

$$I(\mathbf{r}_T) = \frac{16\pi^3 C^2 \hbar^3 e}{\kappa^2 m^2} n^T \int_0^{eV} n^S(\mathbf{r}_T, E_F^S + E) dE. \quad (2.1.18)$$

Since the tip's electronic structure is completely featureless in this s -wave approximation, n_T is a constant representing the average DOS of the tip in the selected energy window. We also introduced the local density of states (LDOS) of the sample:

$$n^S(\mathbf{r}_T, E) = \sum_{\mu} \delta(E_{\mu} - E) |\psi_{\mu}(\mathbf{r}_T)|^2. \quad (2.1.19)$$

Although the absolute value of the current cannot be determined (since C is unknown), the Tersoff-Hamann model became very popular in the STM community to simulate and interpret STM images. It is a very powerful tool for interpreting features of STM images on the characteristic scale of $\sim 10 \text{ \AA}$, but below that

resolution it often fails due to the complete lack of tip electronic structure. As we will see in the following chapters, the tip's orbital character and orientation can have a considerable effect on the STM image, therefore it is always necessary to check the validity of the Tersoff-Hamann model in a particular tip-sample configuration.

2.1.2.1 Spin-polarized current

Starting from Bardeen's formula of the spin-dependent case (2.1.14) one could derive a simple formula for the tunneling current using the assumptions of Tersoff and Hamann [27]. In this case the tunneling current is

$$I(\mathbf{r}_T) = \frac{8\pi^3 C^2 \hbar^3 e}{\kappa^2 m^2} \int_0^{eV} [n^S(\mathbf{r}_T, E_F^S + E) n^T(E_F^T + E - eV) + \mathbf{m}^S(\mathbf{r}_T, E_F^S + E) \cdot \mathbf{m}^T(E_F^T + E - eV)] dE. \quad (2.1.20)$$

The LDOS of the sample is simply the sum of the spin-decomposed LDOS

$$n^S(\mathbf{r}_T, E) = n_{\uparrow}^S(\mathbf{r}_T, E) + n_{\downarrow}^S(\mathbf{r}_T, E) = \sum_{\mu} \sum_{\sigma} \delta(E_{\mu} - E) |\psi_{\mu\sigma}(\mathbf{r}_T)|^2, \quad (2.1.21)$$

while the local magnetization DOS of the sample $\mathbf{m}^S(\mathbf{r}_T, E)$ is given by

$$\mathbf{m}^S(\mathbf{r}_T, E) = \sum_{\mu} \sum_{\sigma} \delta(E_{\mu} - E) \psi_{\mu\sigma}^{\dagger}(\mathbf{r}_T) \boldsymbol{\sigma} \psi_{\mu\sigma}(\mathbf{r}_T). \quad (2.1.22)$$

In collinear magnetic case, *e.g.* Fe(110) discussed in Sec. 3.2, the magnetization DOS simplifies to

$$\begin{aligned} \mathbf{m}^S(\mathbf{r}_T, E) &= [n_{\uparrow}^S(\mathbf{r}_T, E) - n_{\downarrow}^S(\mathbf{r}_T, E)] \hat{\mathbf{e}}^S = \\ &= \sum_{\mu} \delta(E_{\mu} - E) [|\psi_{\mu\uparrow}(\mathbf{r}_T)|^2 - |\psi_{\mu\downarrow}(\mathbf{r}_T)|^2] \hat{\mathbf{e}}^S \end{aligned} \quad (2.1.23)$$

where $\hat{\mathbf{e}}^S$ is the local spin quantization axis (vector) of the sample, the up (\uparrow) and down (\downarrow) components are defined with respect to that.

2.1.3 Chen's method

The first extension of the Tersoff-Hamann model was proposed by Chen in the early '90s. He considered the general solutions of the Schrödinger equation allowing the tip having more complex character and derived the famous *derivative rule* [15]. With his elegant model it was possible to explain the extremely large corrugation and corrugation reversal phenomena observed on several surfaces [28].

tip state	$M_{\mu\nu} \propto$ value at \mathbf{r}_T
s	ψ_μ
p_y	$\frac{\partial \psi_\mu}{\partial y}$
p_z	$\frac{\partial \psi_\mu}{\partial z}$
p_x	$\frac{\partial \psi_\mu}{\partial x}$
d_{xy}	$\frac{\partial^2 \psi_\mu}{\partial x \partial y}$
d_{yz}	$\frac{\partial^2 \psi_\mu}{\partial y \partial z}$
$d_{3z^2-r^2}$	$\frac{\partial^2 \psi_\mu}{\partial z^2} - \frac{1}{3} \kappa_\nu^2 \psi_\mu$
d_{xz}	$\frac{\partial^2 \psi_\mu}{\partial x \partial z}$
$d_{x^2-y^2}$	$\frac{\partial^2 \psi_\mu}{\partial x^2} - \frac{\partial^2 \psi_\mu}{\partial y^2}$

Table 2.1.1: tunneling matrix elements for different tip states according to Chen [15].

Chen's approach is based on the expansion of the tip wave function into spherical harmonic components on and beyond the separation surface:

$$\chi_\nu(\mathbf{r}) = \sum_{lm} C_{\nu,lm} k_l(\kappa_\nu r) Y_{lm}(\vartheta, \varphi), \quad (2.1.24)$$

where $r = |\mathbf{r} - \mathbf{r}_T|$, k_l is the spherical modified Bessel function of the second kind, Y_{lm} is the spherical harmonic function depending on the azimuthal (ϑ) and polar (φ) angles, and κ_ν is the vacuum decay of the tip wavefunction. Coefficient $C_{\nu,lm}$ has to be determined from first principle calculations. By selecting one component of the decomposed wavefunction and using the Green's-function method, Chen derived the so called *derivative rule*. The matrix elements $M_{\mu\nu}$ (see Bardeen's

formula in Eq. 2.1.6) are proportional to different derivatives of the sample wavefunction (ψ_μ) evaluated at the tip position (\mathbf{r}_T). These matrix elements are listed in Tab. 2.1.1 for different tip states.

2.1.4 Atom superposition method

Recently, Palotás *et al.* developed an atom superposition approach for simulating spin-polarized STM (SP-STM) [29] and spin-polarized STS (SP-STs) [30] based on previous theories [31, 27, 32, 33, 34]. In the model it is assumed that electrons tunnel through one tip apex atom, and contributions from individual transitions between this apex atom and each of the surface atoms are summed up assuming the one-dimensional (1D) Wentzel-Kramers-Brillouin (WKB) approximation (see subsection 2.1.4.1) for electron tunneling processes. Assuming that the wavefunctions decay exponentially to the vacuum with a vacuum decay constant κ , the atom superposition method approximates the LDOS as the superposition of atom-projected DOS (PDOS) weighted with these exponential factors:

$$n(\mathbf{r}, E) = \sum_i e^{-2\kappa|\mathbf{r}_T - \mathbf{r}_i|} \tilde{n}(\mathbf{r}_i, E), \quad (2.1.25)$$

where $\tilde{n}(\mathbf{r}_i, E)$ is the PDOS of the i th atom located at \mathbf{r}_i position. The atom-projected DOS is determined from *ab initio* electronic structure calculations as the average LDOS in the Wigner-Seitz sphere of the i th atom:

$$\tilde{n}(\mathbf{r}_i, E) = \sum_\mu \delta(E_\mu - E) \frac{1}{V_{(WS)_i}} \int_{(WS)_i} |\psi_\mu(\mathbf{r}')|^2 d\mathbf{r}'^3, \quad (2.1.26)$$

with \mathbf{r}_i being the center of the Wigner-Seitz sphere, *i.e.* the position of the i th atom. The integral is normalized by the volume of the Wigner-Seitz sphere, $V_{(WS)_i}$.

The model accounts for the tip's electronic structure as well, exceeding the Tersoff-Hamann model. The PDOS of the tip and the sample explicitly appears in the tunneling current formula:

$$I(\mathbf{r}_T) = \frac{2e^2}{h} \eta \sum_i \int_0^{eV} e^{-2\kappa|\mathbf{r}_T - \mathbf{r}_i|} \tilde{n}^S(\mathbf{r}_i, E_F^S + E) \tilde{n}^T(\mathbf{r}_T, E_F^T + E - eV) dE. \quad (2.1.27)$$

The factor η is introduced to ensure the correct dimensions after separating the conductance quantum $2e^2/h$. The value of η has to be determined from comparison to other methods, *e.g.* to the Bardeen method, but the specific value does not affect the qualitative features of the simulated STM image.

2.1.4.1 Electrostatics of the transition

The vacuum decay constant denoted by κ can be calculated applying the Wentzel-Kramers-Brillouin approximation for finding the solution of the 1D Schrödinger equation:

$$-\frac{\hbar^2}{2m}\nabla^2\psi(x) + \phi(x)\psi(x) = E\psi(x). \quad (2.1.28)$$

When the potential energy is greater than the total energy the approximate solution is

$$\psi(x) = \frac{C e^{-\int_0^x \sqrt{\frac{2m}{\hbar^2}(\phi(x')-E)} dx'}}{\sqrt[4]{\frac{2m}{\hbar^2}(\phi(x)-E)}} = \psi_0(x) e^{-\kappa(E)x}. \quad (2.1.29)$$

We can identify the vacuum decay as an integral depending on the potential function:

$$\kappa(E) = \frac{1}{x} \int_0^x \sqrt{\frac{2m}{\hbar^2}(\phi(x')-E)} dx'. \quad (2.1.30)$$

If we want to apply this formula to the electron tunneling in an STM setup some further approximations are needed, since the local potential is affected by the presence of the tip and also by the applied bias voltage. The simplest way is to assume a constant effective potential barrier between the sample and the tip that is determined by the work function of the sample (ϕ^S), the work function of the tip (ϕ^T) and the bias voltage (V): $\phi_{eff} = \frac{\phi^S + \phi^T + eV}{2}$. Using this effective potential function in Eq. (2.1.30) the vacuum decay is:

$$\kappa(E, V) = \sqrt{\frac{2m}{\hbar^2} \left[\frac{\phi^S + \phi^T + eV}{2} - (E - E_F^S) \right]}. \quad (2.1.31)$$

The schematic diagram of the potential function and the effective barrier is shown in Fig. 2.1.1

Assuming a linear potential function in the vacuum region we could apply (2.1.30) directly with $\phi(x) = \phi^S + \frac{\phi^T + eV - \phi^S}{d}x$. After performing the integration

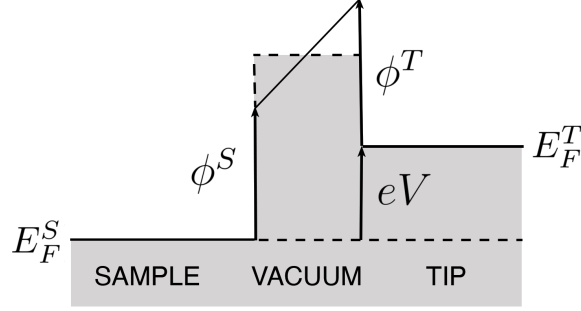


Figure 2.1.1: Schematic diagram of the potential function and the effective rectangular barrier (dotted line). The work functions are denoted by ϕ^S and ϕ^T for the sample and the tip, respectively. The applied bias voltage (V) shifts the Fermi level of the tip (E_F^T) with respect to the Fermi level of the sample (E_F^S).

the vacuum decay is:

$$\kappa(E, V) = \frac{2\sqrt{2m}}{3\hbar} \frac{(\phi^T + eV - (E - E_F^S))^{\frac{3}{2}} - (\phi^S - (E - E_F^S))^{\frac{3}{2}}}{\phi^T - \phi^S + eV}. \quad (2.1.32)$$

We should emphasize that for different tip and sample materials the difference of the work functions is generally small compared to their absolute values and to the applied bias voltage as well ($\phi^S \approx \phi^T \gg eV$). In this case the effective rectangular potential barrier is a good approximation, and the two formulas give similar results.

The work functions can be calculated from the local electrostatic potential data obtained from the electronic structure calculations. For a single atom it is simply the difference between the Fermi energy and the maximum of the electrostatic potential Φ (which corresponds to the potential of the free electron). Therefore the work function of the tip is:

$$\phi^T = \max_z \{\Phi(x_T, y_T, z)\} - E_F^T, \quad (2.1.33)$$

where the position of the tip apex is $\mathbf{r}_T = (x_T, y_T, z_T)$. We restricted the maximum search to the z -axis which is perpendicular to the sample surface. For the sample we can calculate the maximum value above fine $N_x \times N_y$ grid and use the average value as the work function:

$$\phi^S = \max_z \left\{ \frac{1}{N_x N_y} \sum_{x,y} \Phi(x, y, z) \right\} - E_F^S. \quad (2.1.34)$$

2.1.4.2 Spin-polarized current

The spin-polarized case can be treated similarly to the Tersoff-Hamann method. We can apply the atom superposition method to the local magnetic DOS as well:

$$\mathbf{m}(\mathbf{r}, E) = \sum_i e^{-2\kappa|\mathbf{r}_T - \mathbf{r}_i|} \tilde{\mathbf{m}}(\mathbf{r}_i, E), \quad (2.1.35)$$

where $\tilde{\mathbf{m}}(\mathbf{r}_i, E)$ is the atom-projected magnetic DOS of the i th atom, calculated as the average local magnetic DOS in the Wigner-Seitz sphere:

$$\tilde{\mathbf{m}}(\mathbf{r}_i, E) = \sum_{\mu} \delta(E_{\mu} - E) \frac{1}{V_{(WS)_i}} \int_{(WS)_i} \psi_{\mu\sigma}^+(\mathbf{r}') \boldsymbol{\sigma} \psi_{\mu\sigma}(\mathbf{r}') d\mathbf{r}'^3. \quad (2.1.36)$$

Combining the magnetic and non-magnetic contributions we get the formula of the tunneling current in the spin-polarized case:

$$\begin{aligned} I(\mathbf{r}_T) = & \frac{2e^2}{h} \eta \sum_i \int_0^{eV} e^{-2\kappa|\mathbf{r}_T - \mathbf{r}_i|} [\tilde{n}^S(\mathbf{r}_i, E_F^S + E) \tilde{n}^T(\mathbf{r}_T, E_F^T + E - eV) + \\ & + \tilde{\mathbf{m}}^S(\mathbf{r}_i, E_F^S + E) \cdot \tilde{\mathbf{m}}^T(\mathbf{r}_T, E_F^T + E - eV)] dE. \end{aligned} \quad (2.1.37)$$

2.2 New developments

2.2.1 Orbital-dependent 3D-WKB

The main advantage of the 3D-WKB method over the Tersoff-Hamann model is the inclusion of the tip's electronic structure. However, since it is originated from the Tersoff-Hamann model, it still lacks the consideration of the orbital characteristics of the tip and assumes a spherical tip wavefunction. We extend the tunneling model by taking advantage of the orbital decomposition of the electronic structure data and the real-space shape of the electron orbitals. We used the extended model to investigate corrugation inversion phenomena, tip-rotational and magnetic effects for various systems. The corresponding results are discussed in Chapter 3.

The PDOS and magnetic PDOS of the sample surface atoms and the tip apex

can be decomposed according to orbital symmetries (β), as

$$\begin{aligned}\tilde{n}^{S/T}(\mathbf{r}_i, E) &= \sum_{\beta} \tilde{n}_{\beta}^{S/T}(\mathbf{r}_i, E), \\ \tilde{\mathbf{m}}^{S/T}(\mathbf{r}_i, E) &= \sum_{\beta} \tilde{\mathbf{m}}_{\beta}^{S/T}(\mathbf{r}_i, E).\end{aligned}\quad (2.2.1)$$

Similar decomposition of the Green functions has been employed in the linear combination of atomic orbitals (LCAO) scheme by Refs. [16] and [17]. Using the decomposition described in (2.2.1) we can generalize the atom superposition formulas (2.1.25) and (2.1.35). Generally, the decay of the wavefunctions is orientation dependent and described by the real spherical harmonics $Y_{\beta}(\vartheta, \varphi)$:

$$\psi_{\beta}(\mathbf{r}) = e^{-\kappa|\mathbf{r}-\mathbf{r}_0|} Y_{\beta}(\vartheta, \varphi) \psi_{\beta}(\mathbf{r}_0). \quad (2.2.2)$$

ϑ and φ are the azimuthal and polar angles describing the orientation of the $\mathbf{r}-\mathbf{r}_0$ vector pointing from the center of the atom (\mathbf{r}_0) to an arbitrary position \mathbf{r} . Using this modified decay (2.2.2) and the decomposition of the charge and magnetic PDOS functions (2.2.1) the atom superposition formulas take the following form:

$$\begin{aligned}n^{S/T}(\mathbf{r}, E) &= \sum_i \sum_{\beta} e^{-2\kappa|\mathbf{r}_T-\mathbf{r}_i|} |Y_{\beta}(\vartheta, \varphi)|^2 \tilde{n}_{\beta}^{S/T}(\mathbf{r}_i, E), \\ \mathbf{m}^{S/T}(\mathbf{r}, E) &= \sum_i \sum_{\beta} e^{-2\kappa|\mathbf{r}_T-\mathbf{r}_i|} |Y_{\beta}(\vartheta, \varphi)|^2 \tilde{\mathbf{m}}_{\beta}^{S/T}(\mathbf{r}_i, E).\end{aligned}\quad (2.2.3)$$

Now we can generalize the tunneling current formula to account for different orbital characters:

$$\begin{aligned}I(\mathbf{r}_T) &= \frac{2e^2}{h} \eta \sum_i \sum_{\beta, \gamma} \int_0^{eV} T_{\beta\gamma}(\kappa, \mathbf{r}_T - \mathbf{r}_i) \times \\ &\times [\tilde{n}_{\beta}^S(\mathbf{r}_i, E_F^S + E) \tilde{n}_{\gamma}^T(\mathbf{r}_T, E_F^S + E - eV) + \\ &+ \tilde{\mathbf{m}}_{\beta}^S(\mathbf{r}_i, E_F^S + E) \cdot \tilde{\mathbf{m}}_{\gamma}^T(\mathbf{r}_T, E_F^S + E - eV)] dE\end{aligned}\quad (2.2.4)$$

Here, we introduced the transmission coefficient $T_{\beta\gamma}(\kappa, \mathbf{r}_T - \mathbf{r}_i)$ which gives the electron tunneling probability from the tip apex γ orbital to the β orbital of the i th surface atom at positive bias voltage ($V > 0$), and from the β orbital of the i th surface atom to the tip apex γ orbital at negative bias ($V < 0$). In the

orbital independent case the transmission coefficient is simply the exponential factor $T_{\beta\gamma}(\kappa, \mathbf{r}_T - \mathbf{r}_i) = e^{-2\kappa|\mathbf{r}_T - \mathbf{r}_i|}$ for every $\beta \leftrightarrow \gamma$ transition, while in the orbital dependent case it is weighted according to the orbital symmetries:

$$T_{\beta\gamma}(\kappa, \mathbf{r}_T - \mathbf{r}_i) = e^{-2\kappa|\mathbf{r}_T - \mathbf{r}_i|} |Y_\beta(\vartheta_i, \varphi_i)|^2 |Y_\gamma(\vartheta'_i, \varphi'_i)|^2 = e^{-2\kappa|\mathbf{r}_T - \mathbf{r}_i|} t_{\beta\gamma}. \quad (2.2.5)$$

We separated the geometrical factor $|Y_\beta(\vartheta_i, \varphi_i)|^2 |Y_\gamma(\vartheta'_i, \varphi'_i)|^2$ and denote it as $t_{\beta\gamma}$. The angular dependence of the wavefunctions (as a function of the azimuthal (ϑ) and polar (φ) angles) is defined in a local coordinate system, located at the center of the corresponding (i th surface or tip apex) atom. Therefore the $\mathbf{r}_T - \mathbf{r}_i$ vector is given with the polar coordinates $(d_i, \vartheta_i, \varphi_i)$ in the sample's reference frame, and with $(d_i, \vartheta'_i, \varphi'_i) = (d_i, \pi - \vartheta_i, \pi + \varphi_i)$ in the tip's reference frame, where $d_i = |\mathbf{r}_T - \mathbf{r}_i|$ is the distance between the tip apex and the i th sample surface atom. The geometry of a general tip-sample setup can be seen in Fig. 2.2.1. In (2.2.2) and (2.2.5) the real spherical harmonics can be normalized

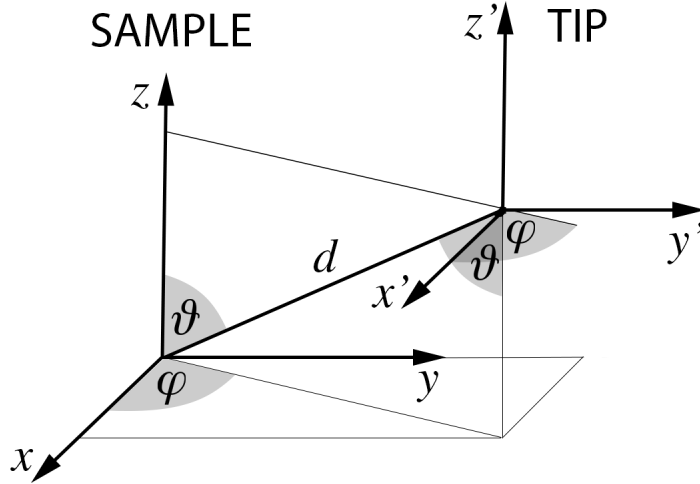


Figure 2.2.1: General tip-sample geometry. Adapted from Ref. [P1].

in such a way, that $0 \leq |Y_\beta(\vartheta, \varphi)|^2 \leq 1$, therefore the transmission coefficient $T_{\beta\gamma}(\kappa, \mathbf{r}_T - \mathbf{r}_i)$ can be represented as transmission probability for a given $\beta \leftrightarrow \gamma$ transition. The maximum probability is obtained if the angular distributions of the electron density according to the given orbital symmetries around both the sample surface atom and the tip apex have maxima along the line of the tunneling direction. This is always the case for the $s-s$ type of tunneling irrespective of the relative position of the tip apex and sample surface atoms; *i.e.*, we observe perfect

spherical exponential decay between tip and sample s orbitals. The s, p and d orbitals, the corresponding spherical harmonic functions and the normalized real spherical harmonic functions are summarized in Table 2.2.1 .

orbital (β)	definition	angular dependence
s	Y_0^0	1
p_y	$Y_1^1 - Y_1^{-1}$	$\sin(\vartheta) \sin(\varphi)$
p_z	Y_1^0	$\cos(\vartheta)$
p_x	$Y_1^1 + Y_1^{-1}$	$\sin(\vartheta) \cos(\varphi)$
d_{xy}	$Y_2^2 - Y_2^{-2}$	$\sin^2(\vartheta) \sin(2\varphi)$
d_{yz}	$Y_2^1 - Y_2^{-1}$	$\sin(2\vartheta) \sin(\varphi)$
$d_{3z^2-r^2}$	Y_2^0	$\frac{1}{2} (3 \cos^2(\vartheta) - 1)$
d_{xz}	$Y_2^1 + Y_2^{-1}$	$\sin(2\vartheta) \cos(\varphi)$
$d_{x^2-y^2}$	$Y_2^2 + Y_2^{-2}$	$\sin^2(\vartheta) \cos(2\varphi)$

Table 2.2.1: Real-space orbitals, their definition from spherical harmonics $Y_l^m(\vartheta, \varphi)$, and the angular dependence of their wave functions. Adapted from Ref. [P1].

As we mentioned in Sec. 2.1.4, the value of η does not affect the qualitative features of simulated STM images, or any of the conclusions made by using this orbital-dependent 3D-WKB method. Thus, we used $\eta = 1 \text{ eV}^2\text{m}^6$ for all simulation presented in Chapter 3, which gives comparable current values for W(110) (see Sec. 3.1.5).

2.2.1.1 Tip rotations

If the symmetry of the tip orbitals has a considerable effect on the STM image, it follows naturally that so does the tip orientation. All simulation methods require a well-defined tip geometry and orientation. Usually a simple geometry is chosen, *e.g.* a pyramid-shaped tip apex, but the local tip geometry at the apex and the relative orientation of the sample and the tip are unknown and hardly controllable in experiments. In separate electronic structure calculations of the sample and the tip their local coordinate systems are usually set up in such

a way that they represent the corresponding crystallographic symmetries. The electronic structure data are defined in the given local coordinate systems and used in the STM simulations. Thus, the relative orientation of the tip and the sample is fixed and it usually corresponds to a very symmetrical setup, which is unlikely in experiments. Hagelaar *et al.* studied a wide range of tip geometries and spatial orientations in the imaging of the NO adsorption on Rh(111) in combination with STM experiments [35] and their analysis is quite unique among the published STM simulations. The inclusion of the orbital symmetries in the 3D-WKB method gives us the opportunity to account for arbitrary tip orientation and investigate its effect on the STM image.

An arbitrary tip orientation corresponds to a rotated local tip coordinate system with respect to the coordinate system of the sample surface, and thus the i th surface atom. We have to distinguish between these two coordinate systems (as we did previously in Fig. 2.2.1), so that the coordinates of a given vector are denoted with primes ($'$) if they are defined in the (rotated) coordinate system of the tip: (x', y', z') or $(r', \vartheta', \varphi')$, and without primes if defined in the coordinate system of the sample (x, y, z) or (r, ϑ, φ) . The rotation of the axes of these two coordinate systems with respect to each other is given by the Euler angles $(\vartheta_0, \varphi_0, \psi_0)$ shown in Fig. 2.2.2. The transformation of local coordinates, which eventually defines the geometrical factor in the transmission coefficient (2.2.5) via ϑ' and φ' , can be described by the rotation matrix \mathcal{R} :

$$\begin{bmatrix} x' \\ y' \\ z' \end{bmatrix} = \mathcal{R} \begin{bmatrix} x \\ y \\ z \end{bmatrix}, \quad (2.2.6)$$

where the rotation matrix has the following form:

$$\mathcal{R} = \begin{bmatrix} \cos \varphi_0 \cos \psi_0 - & \cos \varphi_0 \sin \psi_0 + & \sin \varphi_0 \sin \vartheta_0 \\ \sin \varphi_0 \sin \psi_0 \cos \vartheta_0 & \sin \varphi_0 \cos \psi_0 \cos \vartheta_0 & \\ - \sin \varphi_0 \cos \psi_0 - & - \sin \varphi_0 \sin \psi_0 + & \cos \varphi_0 \sin \vartheta_0 \\ \cos \varphi_0 \sin \psi_0 \cos \vartheta_0 & \cos \varphi_0 \cos \psi_0 \cos \vartheta_0 & \\ \sin \psi_0 \sin \vartheta_0 & - \cos \psi_0 \sin \vartheta_0 & \cos \vartheta_0 \end{bmatrix}. \quad (2.2.7)$$

The angular dependence of the rotated tip orbitals then can be expressed

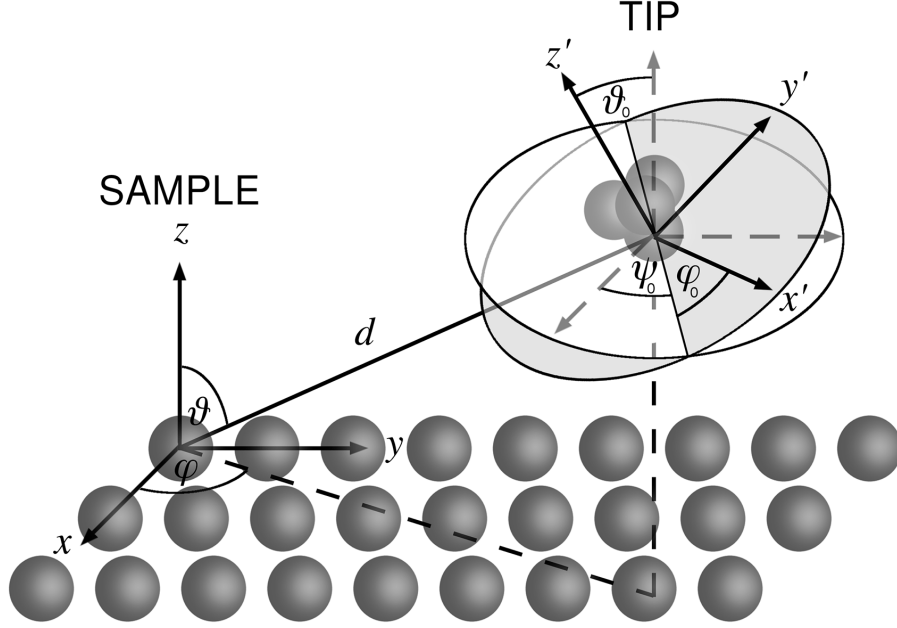


Figure 2.2.2: Geometry of a general tip-sample setup. The rotation of the tip coordinate system is described by the Euler angles . Adapted from Ref. [P1].

using the definitions in Table (2.2.1). with the modified ϑ'_i and φ'_i angles:

$$\begin{aligned}\vartheta'_i &= \arccos\left(\frac{z'_i}{d_i}\right) \\ \varphi'_i &= \arccos\left(\frac{x'_i}{d_i \sin \vartheta'_i}\right) \\ d_i &= \sqrt{x_i'^2 + y_i'^2 + z_i'^2},\end{aligned}\tag{2.2.8}$$

where $d_i = |\mathbf{r}_i - \mathbf{r}_T|$ is the distance between the tip apex and the i th sample surface atom and $\mathbf{r}_i - \mathbf{r}_T = (x'_i, y'_i, z'_i)$.

The effect of tip rotation is discussed in Chapter 3.1 for W(110), and in Chapters 3.3 and 3.4 for HOPG.

2.2.2 Revised Chen's method

The expansion of the tip wavefunction (Eq. 2.1.24) can also be done according to the orbital characters if we introduce the composite index $\beta = (l, m)$ and the real spherical harmonics (Y_β):

$$\chi_\nu(\mathbf{r}) = \sum_{\beta} C_{\nu,\beta} k_{\beta}(\kappa_{\nu} r) Y_{\beta}(\vartheta, \varphi). \quad (2.2.9)$$

Using this expansion of the tip wavefunction and the calculated matrix elements from Table 2.1.1 the derivative rule can be formulated in a more compact form:

$$|M_{\mu\nu}|^2 = \frac{4\pi^2 \hbar^4}{\kappa_{\nu}^2 m^2} \left| \sum_{\beta} C_{\nu,\beta} \hat{\partial}_{\beta} \psi_{\mu}(\mathbf{r}_T) \right|^2. \quad (2.2.10)$$

The differential operator $\hat{\partial}_{\beta}$ acts on the sample wavefunction and has to be evaluated at the tip apex position (\mathbf{r}_T). Note that $\hat{\partial}_{\beta}$ contains a factor κ_{ν}^{-l} (l is the angular quantum number), hence it is dimensionless. The differential operators for the given orbital characters are summarized in Table 2.2.2.

orbital character (β)	$\hat{\partial}_{\nu\beta}$
s	1
p_y	$\frac{1}{\kappa_{\nu}} \frac{\partial}{\partial y}$
p_z	$\frac{1}{\kappa_{\nu}} \frac{\partial}{\partial z}$
p_x	$\frac{1}{\kappa_{\nu}} \frac{\partial}{\partial x}$
d_{xy}	$\frac{1}{\kappa_{\nu}^2} \frac{\partial^2}{\partial x \partial y}$
d_{yz}	$\frac{1}{\kappa_{\nu}^2} \frac{\partial^2}{\partial y \partial z}$
$d_{3z^2-r^2}$	$\frac{3}{\kappa_{\nu}^2} \frac{\partial^2}{\partial z^2} - 1$
d_{xz}	$\frac{1}{\kappa_{\nu}^2} \frac{\partial^2}{\partial x \partial z}$
$d_{x^2-y^2}$	$\frac{1}{\kappa_{\nu}^2} \left(\frac{\partial^2}{\partial x^2} - \frac{\partial^2}{\partial y^2} \right)$

Table 2.2.2: Differential operators $\hat{\partial}_{\nu\beta}$ for given orbital symmetries (β). Adapted from Ref. [P6]

The applicability of the model depends on whether one could calculate the coefficients explicitly or not. In the later case, it is possible to use simplified tip models with a specific orbital character, *i.e.* using the same set of coefficients $\{C_{\beta}\}$ regardless of the energy. In the study of Gross *et al.* CO-functionalized tips with s and p orbitals were considered, although the interference terms were neglected[36].

Siegert *et al.* calculated the tunneling current using the reduced density matrix formalism, which accounts for the interference, but using a simplified tip model: the linear combinations of s and p orbitals were still energy independent [37]. Another possible case is when the coefficients are not known explicitly, but we have some information on the tip electronic structure, *e.g.* the atom projected density of states (PDOS) decomposed according to orbital symmetries. In this Section we will show how Chen's method can be combined with *ab initio* electronic structure calculations to give a powerful tool for simulating STM images and also investigating tip interference and orientational effects. The new theoretical developments - presented in this section 2.2.2 - were implemented in the bSKAN code [38, 39]. The corresponding simulational results are presented in Chapter 4.

2.2.2.1 Tip orbital interference

Introducing a new notation, $M_{\mu\nu\beta} = C_{\nu\beta}\hat{\partial}_{\nu\beta}\psi_{\mu}(\mathbf{r}_T)$ - that corresponds to the tunneling matrix element of a given orbital symmetry (β) - we can rewrite the formula of the matrix elements in (2.2.10):

$$\begin{aligned} |M_{\mu\nu}|^2 &= \frac{4\pi^2\hbar^4}{\kappa_{\nu}^2 m^2} \sum_{\beta} \sum_{\beta'} M_{\mu\nu\beta}^* M_{\mu\nu\beta'} = \\ &= \frac{4\pi^2\hbar^4}{\kappa_{\nu}^2 m^2} \left[\sum_{\beta} |M_{\mu\nu\beta}|^2 + \sum_{\beta \neq \beta'} 2\text{Re}\{M_{\mu\nu\beta}^* M_{\mu\nu\beta'}\} \right] \end{aligned} \quad (2.2.11)$$

By decomposing the tip wavefunction and matrix elements according to orbital symmetries we are also able to investigate different contributions to the tunneling current separately. Contributions of "pure" orbitals ($\beta = \beta'$) are always positive, hence increase the tunneling current, while the cross-terms ($\beta \neq \beta'$) combined with their complex conjugates can cause destructive interference. The analysis of the ratios and polarities of these contributions could lead to a better understanding of the tunneling process. The effect of tip orbital interference is investigated in Chapter 4. Note that in (2.2.10) the sample wavefunction ψ_{μ} can be expanded according to the spherical harmonics, similarly to (2.2.9). This way the interference of the sample orbitals and also the interference between sample and tip orbitals can be investigated. A similar decomposition of matrix elements was used by Jurczyszyn [40, 41] and Mingo [16].

2.2.2.2 Plane-wave expansion

There are many DFT codes which use a plane wave basis set, *e.g.*, VASP [42], ABINIT [43] and Quantum-Espresso [44] to name a few popular ones. The plane-wave expansion makes it relatively easy to implement Chen's derivative rule since the calculation of spatial derivatives (see Table 2.2.2) of the sample wavefunction is straightforward. The presented forms of the spatial derivatives can be potentially useful for implementing the revised method into other STM simulation codes as well. Let us assume that the single electron wavefunctions of the sample surface are given in the vacuum at position vector \mathbf{r} on a two-dimensional (2D) Fourier-grid as

$$\psi_\mu(\mathbf{r}) = \psi_{n^S \mathbf{k}_\parallel^S \sigma^S}(\mathbf{r}) = \sum_{\mathbf{G}_\parallel} A_{n^S \mathbf{k}_\parallel^S \sigma^S}(\mathbf{G}_\parallel, z) \exp [i(\mathbf{k}_\parallel^S + \mathbf{G}_\parallel)\mathbf{r}_\parallel], \quad (2.2.12)$$

where $\mu = (n^S \mathbf{k}_\parallel^S \sigma^S)$ is the composite index for single electron states of the sample with $\mathbf{k}_\parallel^S = (k_x^S, k_y^S)$ the lateral component of the wave vector. The derivation with respect to z (the direction perpendicular to the sample surface) acts on the expansion coefficients only,

$$\frac{\partial}{\partial z} \psi_{n^S \mathbf{k}_\parallel^S \sigma^S}(\mathbf{r}) = \sum_{\mathbf{G}_\parallel} \left(\frac{\partial}{\partial z} A_{n^S \mathbf{k}_\parallel^S \sigma^S}(\mathbf{G}_\parallel, z) \right) \exp [i(\mathbf{k}_\parallel^S + \mathbf{G}_\parallel)\mathbf{r}_\parallel], \quad (2.2.13)$$

while the x - and y -derivatives act on the phase factor,

$$\frac{\partial}{\partial x} \psi_{n^S \mathbf{k}_\parallel^S \sigma^S}(\mathbf{r}) = \sum_{\mathbf{G}_\parallel} i(k_x^S + G_x) A_{n^S \mathbf{k}_\parallel^S \sigma^S}(\mathbf{G}_\parallel, z) \exp [i(\mathbf{k}_\parallel^S + \mathbf{G}_\parallel)\mathbf{r}_\parallel], \quad (2.2.14)$$

$$\frac{\partial}{\partial y} \psi_{n^S \mathbf{k}_\parallel^S \sigma^S}(\mathbf{r}) = \sum_{\mathbf{G}_\parallel} i(k_y^S + G_y) A_{n^S \mathbf{k}_\parallel^S \sigma^S}(\mathbf{G}_\parallel, z) \exp [i(\mathbf{k}_\parallel^S + \mathbf{G}_\parallel)\mathbf{r}_\parallel]. \quad (2.2.15)$$

The same procedure can be applied for higher order derivatives listed in Table 2.2.2.

2.2.2.3 Weighting coefficients

We consider three ways for the choice of the weighting coefficients $C_{\nu\beta}$ for matrix elements $M_{\mu\nu\beta} = C_{\nu\beta} \hat{\partial}_{\nu\beta} \psi_\mu(\mathbf{r}_T)$.

- (i) The simplest choice is the assumption of an idealized tip with a given set

of energy independent weighting factors $\{C_\beta\}$. Such examples can be found in the literature. We previously mentioned (see Sec. 2.2.2.3) the works of Gross *et al.* [36] and Siegert *et al.* [37] for using this simplified tip model. Generally, C_β can be a complex number. We restrict the choice of the set of $\{C_\beta\}$ to fulfill the condition: $\sum_\beta |C_\beta|^2 = 1$. Moreover, in this idealized tip model case we choose the vacuum decay of the tip states $\kappa_\nu = 1 \text{ \AA}^{-1}$ for all ν . Examples of the effect of idealized tips as pure s and pure p_z orbitals and a combination of $(s + p_z)/\sqrt{2}$ on the STM image of N-doped graphene will be shown in section 4.2. We will also point out that the effect of interference is remarkable in this case causing a significant contrast change.

(ii) Based on Eq. (2.2.9), $C_{\nu\beta}$ complex numbers can be obtained as

$$C_{\nu\beta} = \left\langle \tilde{Y}_{\nu\beta}(\mathbf{r}) \middle| \chi_\nu(\mathbf{r}) \right\rangle = \langle k_\beta(\kappa_\nu r) Y_\beta(\vartheta, \varphi) | \chi_\nu(\mathbf{r}) \rangle \quad (2.2.16)$$

with $\nu = (n^T \mathbf{k}_\parallel^T \sigma^T)$ composite index for single electron states of the tip, where \mathbf{k}_\parallel^T is the lateral component of the wave vector. We calculate these coefficients explicitly in the Wigner-Seitz sphere ($W - S$) of the tip apex atom with the VASP code. Since symmetry properties of the model tip geometry are taken into account in VASP, we obtain a reduced set of $C_{\nu\beta}$ corresponding to \mathbf{k}_\parallel^T being in the irreducible part of the Brillouin zone. We can calculate how these coefficients change under 2D transformations (\mathcal{T}) of the tip's symmetry group in order to obtain $C_{\nu\beta}$ in the full 2D Brillouin zone. For this, the plane wave expansion of the tip wavefunction is needed,

$$\chi_\nu(\mathbf{r}) = \chi_{n^T \mathbf{k}_\parallel^T \sigma^T}(\mathbf{r}) = \sum_{\mathbf{G}_\parallel} B_{n^T \mathbf{k}_\parallel^T \sigma^T}(\mathbf{G}_\parallel, z) \exp [i(\mathbf{k}_\parallel^T + \mathbf{G}_\parallel) \mathbf{r}_\parallel], \quad (2.2.17)$$

similarly to Eq. (2.2.12). Since the B expansion coefficients are invariant under the \mathcal{T} transformation, *i.e.*, $B_{n^T \mathbf{k}_\parallel^T \sigma^T} = B_{n^T \mathcal{T}(\mathbf{k}_\parallel^T) \sigma^T}$, the transformation of the tip wavefunction comes from that of the phase factors. Using Eqs. (2.2.16) and (2.2.17) we obtain the following for the transformed coefficients,

$$\begin{aligned} C_{n^T \mathcal{T}(\mathbf{k}_\parallel^T) \sigma^T \beta} &= \int_{W-S} k_\beta(\kappa_\nu r) Y_\beta(\mathbf{r}) \sum_{\mathbf{G}_\parallel} B_\nu(\mathbf{G}_\parallel, z) \exp [i\mathcal{T}(\mathbf{k}_\parallel^T + \mathbf{G}_\parallel) \mathbf{r}_\parallel] d^3 r \\ &= \int_{W-S} k_\beta(\kappa_\nu r) Y_\beta(\mathcal{T} \mathbf{r}) \chi_\nu(\mathbf{r}) d^3 r. \end{aligned} \quad (2.2.18)$$

Note that \mathcal{T} are represented by 2×2 real matrices and the transformation of the coordinates is $\mathcal{T}\mathbf{r} = (\mathcal{T}_{11}x + \mathcal{T}_{12}y, \mathcal{T}_{21}x + \mathcal{T}_{22}y, z)$. Using the real spherical harmonics in Cartesian coordinates, we can calculate their transformations by substituting the transformed lateral coordinates into their normalized form. The results are shown in Table 2.2.3. Thus, $C_{\nu\beta}$ is determined in the full 2D Brillouin zone, and we can directly apply them in the formula of the tunneling matrix elements in Eq. (2.2.10).

Orbital	$Y(x, y, z)$	Transformed orbital
s	$\frac{1}{2\sqrt{\pi}}$	s
p_y	$\frac{1}{2}\sqrt{\frac{3}{\pi}}\frac{y}{r}$	$\mathcal{T}_{21}p_x + \mathcal{T}_{22}p_y$
p_z	$\frac{1}{2}\sqrt{\frac{3}{\pi}}\frac{z}{r}$	p_z
p_x	$\frac{1}{2}\sqrt{\frac{3}{\pi}}\frac{x}{r}$	$\mathcal{T}_{11}p_x + \mathcal{T}_{12}p_y$
d_{xy}	$\frac{1}{2}\sqrt{\frac{15}{\pi}}\frac{xy}{r^2}$	$(\mathcal{T}_{11}\mathcal{T}_{22} + \mathcal{T}_{12}\mathcal{T}_{21})d_{xy} + 2\mathcal{T}_{11}\mathcal{T}_{21}d_{x^2-y^2}$
d_{yz}	$\frac{1}{2}\sqrt{\frac{15}{\pi}}\frac{yz}{r^2}$	$\mathcal{T}_{21}d_{xz} + \mathcal{T}_{22}d_{yz}$
$d_{3z^2-r^2}$	$\frac{1}{4}\sqrt{\frac{5}{\pi}}\frac{3z^2-r^2}{r^2}$	$d_{3z^2-r^2}$
d_{xz}	$\frac{1}{2}\sqrt{\frac{15}{\pi}}\frac{xz}{r^2}$	$\mathcal{T}_{11}d_{xz} + \mathcal{T}_{12}d_{yz}$
$d_{x^2-y^2}$	$\frac{1}{4}\sqrt{\frac{15}{\pi}}\frac{x^2-y^2}{r^2}$	$(\mathcal{T}_{11}^2 - \mathcal{T}_{21}^2)d_{x^2-y^2} + 2\mathcal{T}_{11}\mathcal{T}_{12}d_{xy}$

Table 2.2.3: Transformation of real spherical harmonics under 2D symmetry operations (\mathcal{T}) of the tip. . Adapted from Ref. [P6].

(iii) The third suggestion for $C_{\nu\beta}$ is based on the orbital-decomposed DOS projected to the tip apex atom, $n^{TIP}(E) = \sum_{\beta} n_{\beta}^{TIP}(E) = \sum_{\beta} \sum_{\nu} n_{\nu\beta}^{TIP} \delta(E - E_{\nu})$ obtained from first principles calculation. Using the expansion of the tip wavefunction in Eq. (2.2.9) and the approximation of orthonormality for $\tilde{Y}_{\nu\beta}(r, \vartheta, \varphi)$ within the Wigner-Seitz ($W - S$) sphere of the tip apex atom,

$$\left\langle \tilde{Y}_{\nu\beta}(r, \vartheta, \varphi) \left| \tilde{Y}_{\nu\beta'}(r, \vartheta, \varphi) \right. \right\rangle_{W-S} \approx \delta_{\beta\beta'}, \quad (2.2.19)$$

the following is obtained,

$$\begin{aligned} n^{TIP}(E) &= \sum_{\nu} \sum_{\beta} n_{\nu\beta}^{TIP} \delta(E - E_{\nu}) = \sum_{\nu} \langle \chi_{\nu} | \chi_{\nu} \rangle_{W-S} \delta(E - E_{\nu}) \approx \\ &\approx \sum_{\nu} \sum_{\beta} |C_{\nu\beta}|^2 \delta(E - E_{\nu}). \end{aligned} \quad (2.2.20)$$

Thus, we can approximate the complex $C_{\nu\beta}$ coefficients with real values, $C_{\nu\beta} \approx \sqrt{n_{\nu\beta}^{TIP}}$. This way Eq. (2.2.10) is recast to

$$|M_{\mu\nu}|^2 = \frac{4\pi^2 \hbar^4}{\kappa_{\nu}^2 m^2} \left| \sum_{\beta} \sqrt{n_{\nu\beta}^{TIP}} \hat{\partial}_{\nu\beta} \psi_{\mu}(\mathbf{r}_0) \right|^2. \quad (2.2.21)$$

Since the calculation of the orbital-decomposed atom-projected DOS is routinely available in DFT codes, the presented approximation applied to the tip apex atom gives a widely accessible choice for the weighting coefficients in the revised Chen's derivative rule. In section 4.2 we will demonstrate that the STM images obtained by the $C_{\nu\beta} \approx \sqrt{n_{\nu\beta}^{TIP}}$ approximation provide good agreement with those calculated using the proper complex $C_{\nu\beta}$ coefficients according to Eq. (2.2.16).

2.2.2.4 Tip rotations

Since the electronic structures of the sample surface and the tip are generally calculated independently to allow more flexibility with their geometries, arbitrary orientations of the tip can be included into the revised Chen's method. This can be done by redefining the spatial derivatives of the sample wavefunctions corresponding to the orbital characters in the rotated coordinate system of the tip with respect to the sample surface. This rotation is described by a coordinate transformation, which is represented by the same 3×3 matrix \mathcal{R} that we introduced previously (2.2.7). We use the explicit form of \mathcal{R} with the Euler angles $(\vartheta_0, \varphi_0, \psi_0)$, \mathcal{R}_i^j being the matrix elements. Using the Einstein summation convention, the relationship between the two set of coordinates, the rotated tip coordinates $x'^j \in \{x', y', z'\}$ and the sample coordinates $x^i \in \{x, y, z\}$, is the following:

$$x'^j = \frac{\partial x'^j}{\partial x^i} x^i = \mathcal{R}_i^j x^i; \quad x^i = \frac{\partial x^i}{\partial x'^j} x'^j = (\mathcal{R}^{-1})_j^i x'^j. \quad (2.2.22)$$

With the help of these, we can relate the derivatives of the sample wavefunction ψ with respect to the rotated tip coordinates x'^j to the derivatives with respect to the sample coordinates x^i as

$$\frac{\partial\psi}{\partial x'^j} = \frac{\partial\psi}{\partial x^i} \frac{\partial x^i}{\partial x'^j} = \frac{\partial\psi}{\partial x^i} (\mathcal{R}^{-1})_j^i. \quad (2.2.23)$$

Similarly, the second derivatives are

$$\frac{\partial^2\psi}{\partial x'^k \partial x'^j} = \left(\frac{\partial^2\psi}{\partial x^l \partial x^i} \right) (\mathcal{R}^{-1})_j^i (\mathcal{R}^{-1})_k^l. \quad (2.2.24)$$

Using Eqs. (2.2.23) and (2.2.24) the transformed $\hat{\partial}'_{\nu\beta}$ differential operators corresponding to the rotated tip coordinate system can be constructed and employed in Eq. (2.2.10) for the tunneling matrix elements. Since the transformation is linear, this, in turn, results in redefined $C_{\nu\beta}$ weighting coefficients in Eq. (2.2.10) for the $\hat{\partial}_{\nu\beta}$ operators given in the coordinate system of the sample listed in Table 2.2.2.

Chapter 3

3D–WKB results

In this Chapter we will demonstrate the reliability of our orbital-dependent tunneling model and investigate some interesting phenomena observed in STM experiments. As the main advantage of our model over the Tersoff-Hamann or the orbital-independent 3D-WKB model is the inclusion of the tip electronic structure and the orbital symmetries, we will focus on the *corrugation inversion* (or contrast inversion) phenomenon which occurs on several surfaces. Introducing the so called *inversion maps* and *current histograms* we can determine when the inversion will occur depending on the bias voltage and the tip-sample distance, and can also give a quantitative and quantitative explanation to the phenomenon. In Sec. 3.1 we will consider the W(110) surface and - beside the corrugation inversion - we will demonstrate the effect of tip rotations to the STM image. In Sec. 3.2 the magnetic Fe(110) surface is investigated. In this case the contrast inversion is more complex as the STM image is determined by the interplay of the topographic and magnetic contributions of the tunneling current. Sec. 3.3 focuses on the widely used HOPG surface and its contrast changes and stability. We will show that the experimentally observed “stripe” formation is a combined effect of the electronic structure and the tip orbital symmetries, and also point out that triangular-hexagonal contrast change can be achieved by tip rotations alone, not just by bias change. Finally, making use of the remarkable computational efficiency of our method, we will introduce a statistical approach to determine the tip orientation and geometry in a real experiment.

3.1 W(110)

This surface has technological importance as it is widely used as substrate for thin film growth (see, *e.g.*, Refs. [45, 46]). As was pointed out by Heinze *et al.*, [45] the determination of the position of surface atomic sites is not straightforward as atomic resolution is lost at negative bias voltages, and a bias-dependent corrugation reversal has been predicted. This means that normal and anticorrugated constant-current STM images can be obtained in certain bias voltage ranges, and the W atoms do not always appear as protrusions in the images. It was shown that a competition between states from different parts of the surface Brillouin zone is responsible for this effect [47, 45]. We reinvestigate this corrugation-reversal effect with our orbital-dependent tunneling model and compare our results to those obtained by the Tersoff-Hamann and Bardeen methods.

3.1.1 Computational details

The electronic structure calculations were based on the density functional theory (DFT) within the generalized gradient approximation (GGA) implemented in VASP. A plane-wave basis set for electronic wave function expansion together with the projector-augmented wave (PAW) method [48] has been applied, and the exchange-correlation functional is parametrized according to Perdew and Wang (PW91) [49]. The electronic structures of the sample surface and the tip have been calculated separately. We modeled the W(110) surface by a slab of nine layers, where the two topmost W layers have been fully relaxed. After relaxation the W-W interlayer distance between the two topmost layers is reduced by 3.3%, while the underneath W-W interlayer distance is increased by 1.1% compared to bulk W. A separating vacuum region of 18 Å width in the surface normal (z) direction has been set up between neighboring supercell slabs. The average electron work function above the surface is calculated to be $\phi_S = 4.8$ eV. We used a $41 \times 41 \times 5$ Monkhorst-Pack [50] k -point grid for obtaining the orbital-decomposed PDOS onto the surface i th W atom, $\tilde{n}_\beta^S(\mathbf{r}_i, E)$. The same k set has been used for calculating the sample electron wave functions for the Tersoff-Hamann and Bardeen simulations. The unit cell of the W(110) surface (rhombus) and the rectangular scan area for the tunneling current simulation are shown in Fig. 3.1.1. In our calculations we used the experimental lattice constant $a_W = 316.52$ pm.

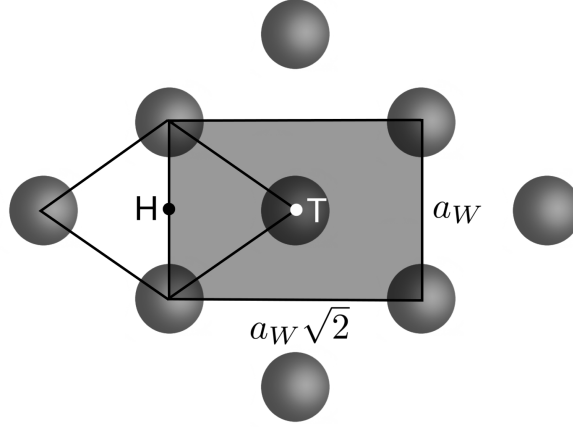


Figure 3.1.1: The surface unit cell of W(110) (rhombus) and the rectangular scan area (shaded) for the tunneling current simulations. Grey spheres denote the W atoms. The top (T) and hollow (H) positions are explicitly shown.

To capture the importance of the orbital symmetries of the tip we considered different tip models:

- The *orbital-independent ideal tip* is characterized by a constant geometrical factor $t_{\beta\gamma} = 1$ for all $\beta \leftrightarrow \gamma$ transitions, and its electronic structure is completely featureless: $\tilde{n}_\gamma^T(\mathbf{r}_T, E) = 1/9 \text{ (eV)}^{-1}$, so that $\tilde{n}^T(\mathbf{r}_T, E) = \sum_\gamma \tilde{n}_\gamma^T(\mathbf{r}_T, E) = 1 \text{ (eV)}^{-1}$.
- *Ideal tip* models having a particular orbital symmetry γ_0 . In this case $t_{\beta\gamma}$ is calculated following Eq. (2.2.5) and for the energy dependence of the tip PDOS, $\tilde{n}_{\gamma_0}^T(\mathbf{r}_T, E) = 1 \text{ (eV)}^{-1}$, and $\tilde{n}_{\gamma_0 \neq \gamma}^T(\mathbf{r}_T, E) = 0$ are assumed. In the simulations we considered three different tip symmetries: $\gamma_0 \in \{s, p_z, d_{3z^2-r^2}\}$.
- *Realistic blunt W(110) tip*. Motivated by a previous simulation [51] it was modeled by a slab consisting of three atomic layers having one W apex atom on both surfaces, *i.e.*, with a double vacuum boundary. The schematic model of the tip is presented in Fig. 3.1.2. In this system the apex atoms are relaxed on both sides. The vertical distance between the adatom and the topmost layer decreased by 19.3% compared to bulk W. The interaction between apex atoms in neighboring supercells in the lateral direction is minimized by choosing a 3×3 surface cell, and a 17.9 Å-wide separating vacuum region in the z direction. The local electron work function above

the tip apex was assumed to be $\phi_T = 4.8$ eV. An $11 \times 15 \times 5$ MP k -point grid has been chosen for calculating the orbital-decomposed projected DOS onto the apex atom, $\tilde{n}_\gamma^T(\mathbf{r}_T, E)$. The same k -point sampling was used for obtaining the tip electron wave functions for the Bardeen calculation.

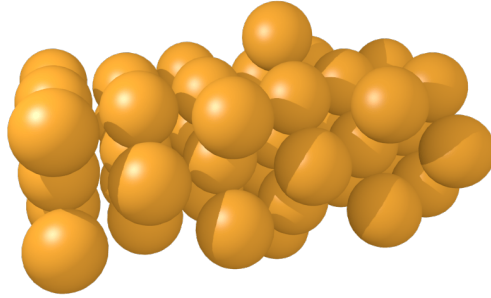


Figure 3.1.2: Schematic model of the blunt W(110) tip consisting of three atomic layers having one W apex atom on both sides.

STM images were simulated employing our orbital-dependent 3D-WKB model, and the Tersoff-Hamann and Bardeen methods implemented in the bSKAN code [38, 39]. Using our model the tunneling current was calculated in a box above the rectangular scan area shown in Fig. 3.1.1 containing 99 000 ($30 \times 22 \times 150$) grid points with a 0.149 Å lateral and 0.053 Å vertical resolution. The electron local density of states (LDOS) was calculated above the same scan area with the same spatial resolution as above. In case of the Bardeen calculations the lateral resolution remains 0.149 Å, and the vertical resolution is 0.106 Å. The constant current contours (STM images) are extracted following the method described in Ref. [29]. All of the STM images are presented above the full rectangular scan area.

3.1.2 Convergence properties

In principle, the summation in the atom superposition method (2.2.4) contains all surface atoms. However, due to the exponentially decaying wavefunctions, a finite and - as we will see later - relatively small number of atoms included in the summation provides reliable, converged results. We also compared the convergence speed of simulations using tips with different symmetries. We considered ideal tips of the orbital-independent model, and with s , p_z , and $d_{3z^2-r^2}$ symmetry, as well as the W(110) tip. To take into account a wide energy range

around the Fermi level, we calculated the tunneling current at -2.5 V and $+2.5$ V bias voltages at $z = 4.5$ Å above a surface W atom (TOP position), and averaged these current values. We also normalized the averaged current to obtain comparable results. Contributions from surface atoms within a radius of $d_{||}$ - measured from the W atom below the tip apex - are considered. We present the normalized, averaged current values as a function of $d_{||}$ in Fig. 3.1.3. We find

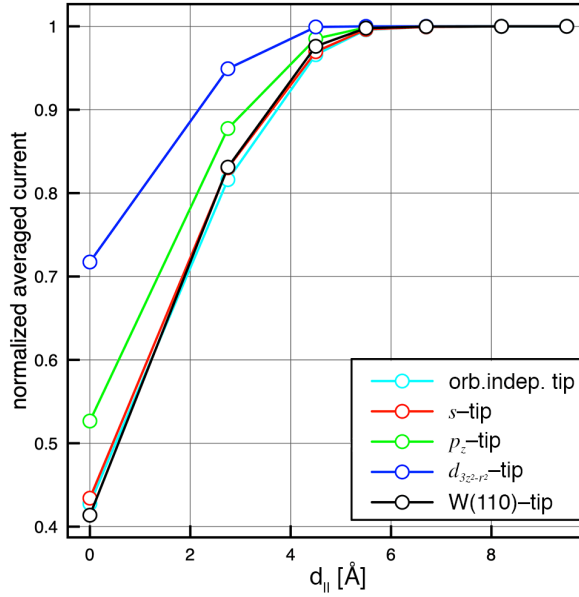


Figure 3.1.3: Convergence of the normalized averaged current calculated with different tip models. Adapted from Ref. [P1].

that the orbital-independent, the s -type, and the W(110) tips behave similarly concerning the current convergence, while for the p_z and $d_{3z^2-r^2}$ tips a faster convergence is found. This rapid convergence can be explained by the more localized character of these tip orbitals in the surface normal direction (z). The orbital-independent and the s -type tip produce similar results. Both tip models neglect the tip's electronic structure and with the s -tip the orbital symmetries come into play only via the sample orbitals leaving the spherically decaying function part dominant in the expression of the transmission coefficient (2.2.5). In the W(110) tip case, electronic states of all considered symmetries have a contribution, and their relative importance is determined not only by the transmission function via the orbital shapes but also by the product of the symmetry-decomposed PDOS of the surface and the tip. In general, the orbitals localized in directions different than the z direction, *e.g.* d_{xy} , d_{xz} etc. can show a slower current convergence than

the s orbitals. However, the partial PDOS of such states is relatively low, and we obtain a similar current convergence in the studied energy range as for the s -type tip. Choosing different bias voltage, and thus different electron states involved in the tunneling, can change this slightly resulting a bit slower or faster convergence compared to the s -tip. However, this does not affect the number of atoms we should include in the simulation. Based on these convergence tests, considering atom contributions within at least $d_{\parallel} = 3a \approx 9.5 \text{ \AA}$ distance from the surface-projected tip position produce well converged results for all tip symmetries and wide bias range. In the case of calculating STM images, d_{\parallel} has to be measured from the edge of the scan area in all directions in order to avoid distortion of the image, thus involving 67 surface atoms in the atomic superposition.

3.1.3 Orbital contributions: current histograms

From Eq. (2.2.4) we can calculate the tunneling current of the $\beta \longleftrightarrow \gamma$ transitions ($I_{\beta\gamma}$) separately:

$$\begin{aligned}
I_{\beta\gamma}(\mathbf{r}_T, V) &= \frac{2e^2}{h} \eta \sum_i \int_0^{eV} T_{\beta\gamma}(\kappa, \mathbf{r}_T - \mathbf{r}_i) \times \\
&\times [\tilde{n}_{\beta}^S(\mathbf{r}_i, E_F^S + E) \tilde{n}_{\gamma}^T(\mathbf{r}_T, E_F^T + E - eV) + \\
&+ \tilde{\mathbf{m}}_{\beta}^S(\mathbf{r}_i, E_F^S + E) \cdot \tilde{\mathbf{m}}_{\gamma}^T(\mathbf{r}_T, E_F^T + E - eV)] dE. \quad (3.1.1)
\end{aligned}$$

The total current is simply the sum of the contributions from all $\beta \longleftrightarrow \gamma$ transitions

$$I(\mathbf{r}_T, V) = \sum_{\beta, \gamma} I_{\beta\gamma}(\mathbf{r}_T, V), \quad (3.1.2)$$

while the relative contribution of a given transition is: (3.3.2)

$$\tilde{I}_{\beta\gamma}(\mathbf{r}_T, V) = \frac{I_{\beta\gamma}(\mathbf{r}_T, V)}{I(\mathbf{r}_T, V)} \quad (3.1.3)$$

With these quantities we can analyze the relative importance of the transitions at different tip positions and bias voltages. From this analysis we obtain a qualitative picture about the role of the different atomic orbitals in the construction of the tunneling current. These can be represented by a current histogram that gives the contributions of the individual transitions to the total current. We calculated such histograms using the W(110) tip at $V = -0.1 \text{ V}$ bias voltage $z = 4.5 \text{ \AA}$

above two different tip positions: above the top (T) position, and above the surface hollow (H) position, see Fig. 3.1.1. The results are shown in Fig. 3.1.4. We find that most contributions are due to the s , p_z , d_{yz} , $d_{3z^2-r^2}$, and d_{xz} orbitals

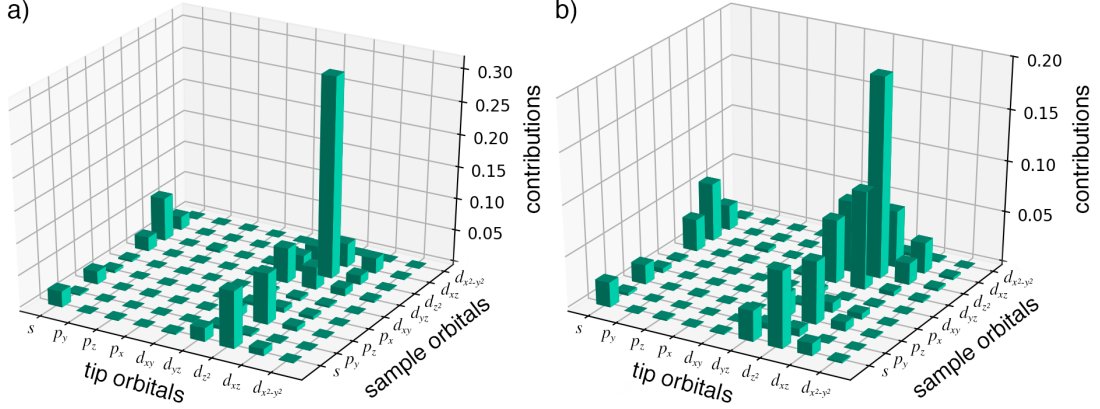


Figure 3.1.4: Histograms of the relative current contributions ($\tilde{I}_{\beta\gamma}$) from all tip-sample transitions with different orbital symmetries using the W(110) tip at $V = -0.1$ V bias. (a) Tip apex $z = 4.5$ Å above the surface top (T) position (W atom); (b) tip apex $z = 4.5$ Å above the surface hollow (H) position. Adapted from Ref. [P1]

and their combinations. The largest contribution to the current is given by the $d_{3z^2-r^2} - d_{3z^2-r^2}$ transition, 31% and 20% above the top and hollow positions, respectively. Concomitantly, above the hollow position, the relative importance of both tip and sample d_{yz} and d_{xz} orbitals is increased as it is expected from the geometrical setup; *i.e.*, the $d_{yz} - d_{yz}$, $d_{yz} - d_{3z^2-r^2}$, $d_{xz} - d_{xz}$, and $d_{xz} - d_{3z^2-r^2}$ contributions correspond to larger orientational overlap of the mentioned tip and sample orbitals if the tip is above the hollow position rather than above the top position as suggested by the geometry in Fig. 3.1.1 and Eq. (2.2.5). Thus, our simple orbital-dependent tunneling model captures the effect of the localized orbitals and goes beyond the spherical Tersoff-Hamann model. Note that if a larger bias voltage is considered, *i.e.*, the electronic states are somewhat averaged, then the independent orbital approach might turn out to be a good approximation [34].

3.1.4 Contrast inversion

The role of the localized orbitals can best be demonstrated by reinvestigating the corrugation-inversion phenomenon found, *e.g.*, on (100) [16], (110) [45], and (111) [52] metal surfaces. Chen explained this effect as a consequence of $m \neq 0$ tip states

[28]. According to Heinze *et al.* [45], under certain circumstances the apparent height of W atoms at the surface top position (T) can be larger or smaller than the apparent height of the surface hollow position (H) at constant current condition. Thus, the sign change of $\Delta z(I) = z_T(I) - z_H(I)$ is indicative for the corrugation inversion. Obviously, $\Delta z(I) > 0$ corresponds to a normal STM image, where the W atoms appear as protrusions, and $\Delta z(I) < 0$ to an anticorrugated image. Since the tunneling current is monotonically decreasing with the increasing tip-sample distance, we can obtain information about the occurrence of the corrugation inversion simply by calculating the current difference between tip positions above the top and hollow sites of the W(110) surface. The current difference at tip-sample distance z and at bias voltage V is defined as

$$\Delta I(z, V) = I_T(z, V) - I_H(z, V). \quad (3.1.4)$$

This quantity can be calculated for specific tips, and we refer to the $\Delta I(z, V) = 0$ contour as the corrugation inversion map. This gives the (z, V) combinations where the corrugation inversion occurs. The sign of $\Delta I(z, V)$ provides the corrugation character of an STM image in the given (z, V) regime. Owing to the monotonically decreasing character of the tunneling current, $\Delta I(z, V) > 0$ corresponds to $\Delta z(I(V)) > 0$, *i.e.*, normal corrugation, and similarly $\Delta I(z, V) < 0$ corresponds to $\Delta z(I(V)) < 0$ and anticorrugation.

First, we calculated $\Delta I(z, V)$ using the independent orbital approximation and Eq. (2.1.27) for the tunneling current and found that $\Delta I(z, V)$ is always positive. This means that the spherical exponential decay itself cannot account for the observed corrugation-inversion effect, and the W atoms always appear as protrusions in STM images calculated with this model. However, considering the orbital-dependent tunneling transmission in Eq. (2.2.4), we find evidence for the corrugation-inversion effect, thus highlighting the role of the real-space shape of electron orbitals involved in the tunneling.

Figure 3.1.5 shows $\Delta I(z, V) = 0$ contours calculated with different tip models in the $[0 \text{ \AA}, 14 \text{ \AA}]$ tip-sample distance and $[-2 \text{ V}, +2 \text{ V}]$ bias voltage range. Before turning to the analysis of the results obtained with previously unconsidered tip models, let us compare our results with those of Heinze *et al.* [45] where an *s*-wave tip model was used. They found corrugation reversal at around -0.4 V at $z = 4.6 \text{ \AA}$ tip-sample distance, and above that voltage normal while below

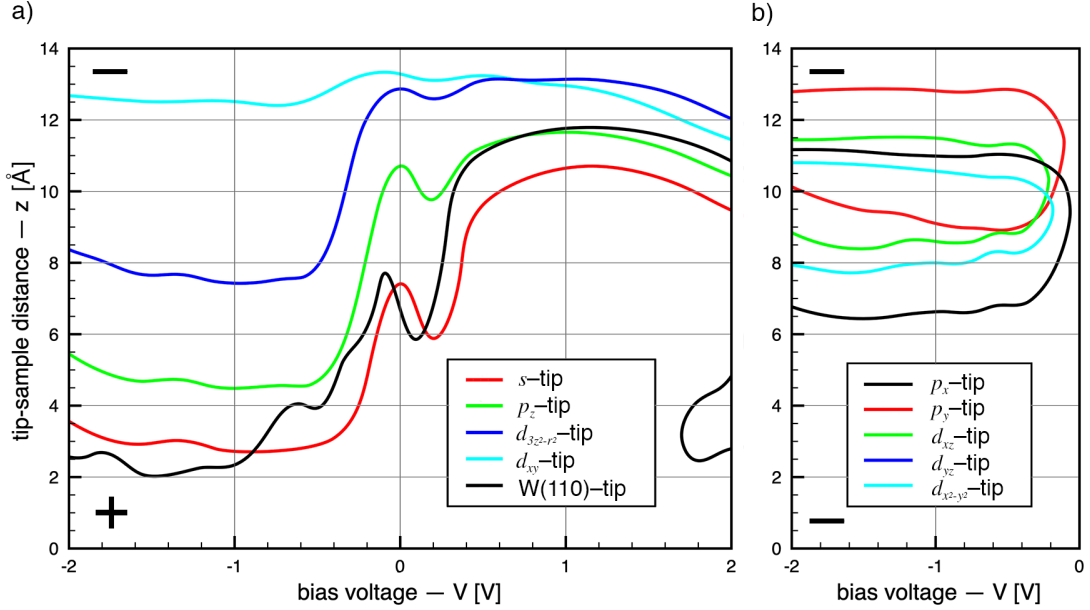


Figure 3.1.5: The $\Delta I(z, V) = I_T(z, V) - I_H(z, V) = 0$ contours indicative for the corrugation inversion calculated with different tip models above the W(110) surface. (a), (b) shows two distinct behaviors depending on the tip orbital composition. The sign of $\Delta I(z, V)$ is explicitly shown: (a) positive (+) below the curves, and negative (-) above them; (b) positive inside the loop of a given curve, and negative (-) outside the loop. Note that positive $\Delta I(z, V)$ corresponds to normal, whereas negative corresponds to inverted atomic contrast. Adapted from Ref. [P1]

anticorrugated STM images were obtained. Our model with an s tip provides the same type of corrugation reversal at -0.21 V at the same distance as can be seen in Fig. 3.1.5(a) (red curve). These bias values are in reasonable agreement, particularly concerning their negative sign. At this range atomic resolution is difficult to achieve experimentally, which is an indication for being close to the corrugation-inversion regime [45]. On the other hand, a linear dependence of the corrugation-reversal voltage and the tip-sample distance was reported by Heinze *et al.*: ($z = 4.6$ Å, $V = -0.4$ V) to ($z = 7.2$ Å, $V = 0$ V). Our model qualitatively reproduces this linear dependence in the same bias range though the quantitative values are somewhat different.

Calculating the corrugation-inversion maps with more tip models, we find two distinct behaviors depending on the tip orbital composition. Figures 3.1.5(a) and 3.1.5(b) show these. While the tip models in Fig. 3.1.5(a) can show corrugation inversion in the whole studied bias range, this effect does not occur at positive bias voltages for tips in Fig. 3.1.5(b). Moreover, anticorrugation is observed in the large tip-sample distance region ($z > 13.5$ Å) in both parts. This is in

accordance with the prediction of Ref. [47] based on the analysis of the competing electron states in the surface Brillouin zone of an Fe(001) surface. In the $z < 13.5 \text{ \AA}$ range, however, the corrugation character in the two parts of Fig. 3.1.5 is remarkably different. In Fig. 3.1.5(a), normal corrugation is found close to the surface, which reverts only once with increasing tip-sample distance for the tip models with a single orbital symmetry in the full studied bias range. The W(110) tip behaves similarly below +1.7 V, while above there is a double reversal of the corrugation character as the tip-sample distance increases. This indicates that anticorrugation can be expected at short tip-sample distances (3.5–5 Å) at around +2 V. On the other hand, the tip models in Fig. 3.1.5(b) always show anticorrugation at positive bias voltages, and below -0.05 V they provide corrugation characters starting from anticorrugation, then normal corrugation, and again anticorrugation with increasing tip-sample distance. These different behaviors can be attributed to the tip orbital characters. It is interesting to notice that none of the considered tip orbitals in Fig. 3.1.5(b) are localized in the z direction, and they have nodal planes either in the yz plane (p_x and d_{xz}) or in the xz plane (p_y and d_{yz}) or in the $x = y$ and $x = -y$ planes ($d_{x^2-y^2}$). On the other hand, in Fig. 3.1.5(a) there are tips which are localized in the z direction (p_z and $d_{3z^2-r^2}$) or having nodal planes in both the xz and yz planes (d_{xy}) as well as the spherical s tip and the W(110) tip that contains all types of orbitals with energy-dependent partial PDOS functions. The particular tip nodal planes restrict the collection of surface atom contributions to specific regions on the sample surface. Furthermore, by changing the tip-sample distance, the orientational overlaps between the tip and sample orbitals change, and according to our model some localized orbitals gain more importance in the tunneling contribution (see also Fig. 3.1.4). Since we calculate the current difference between tip positions above the surface top and hollow sites, the complex tip-sample-distance- and bias-voltage-dependent effect of the real-space orbitals on the tunneling can be visualized via the corrugation-inversion maps.

Concerning tips with p_z and $d_{3z^2-r^2}$ orbital symmetry, Heinze *et al.* [45] calculated a corrugation enhancement factor of 2 and 6.25, respectively, based on Chen's derivative rule [15]. Moreover, they argued that the corrugation-inversion map should be practically identical to the one obtained by using the s -tip model, and the corrugation values just have to be scaled up by these factors. On the contrary, based on our orbital-dependent tunneling model we find that the p_z and

$d_{3z^2-r^2}$ tips provide qualitatively different corrugation inversion maps, although their bias-dependent shape is similar to the one of the s -tip, their tip-sample distance is systematically pushed to larger values [see Fig. 3.1.5(a)]. This is due to the more localized character of these tip orbitals in the z direction. Corrugation inversion with the d_{xy} -tip occurs at the largest tip-sample distance. A possible explanation can be based on its xz and yz nodal planes. While above the top position only the underlying W atom gives zero contribution to the current, above the hollow position all four nearest-neighbor W atoms; thus, I_T is expected to be higher than I_H at small tip-sample distances. To overcome this effect the tip has to be moved farther from the surface since then the relative importance of the nearest-neighbor contributions decays rapidly compared to other parts of the surface.

Apart from the above findings we obtain corrugation inversion also in the positive bias range at enlarged tip-sample distances for the s , p_z , $d_{3z^2-r^2}$, and W(110) tips considered in Fig. 3.1.5(a). This is most probably due to the surface electronic structure. Note that this effect is even more difficult to capture in experiments as the corrugation values themselves decay rapidly with increasing tip-sample distance.

3.1.5 Comparison to other methods

To demonstrate the corrugation inversion more apparently, constant-current STM images can be simulated. As is clear from Fig. 3.1.5, any type of crossing of the $\Delta I(z, V) = 0$ contour results in the occurrence of the corrugation reversal. In experiments two ways can be considered to record STM images in the normal and anticorrugated regimes: (1) keep the tip-sample distance z constant and change the bias voltage V , or (2) keep the bias voltage V constant and change the tip-sample distance. Respectively, these modes correspond to a horizontal and a vertical crossing of the $\Delta I(z, V) = 0$ contour in the (z, V) plane in Fig. 3.1.5. Heinze *et al.* followed the first method in their simulations [45]. However, as the second option seems to be experimentally more feasible and needs less calculations as well, we simulated STM images at a fixed bias voltage of -0.25 V.

In Fig. 3.1.6 STM images are compared using our model assuming an s -type tip [(a)–(c)] to those calculated by the Tersoff-Hamann method [(d)–(f)]. We find

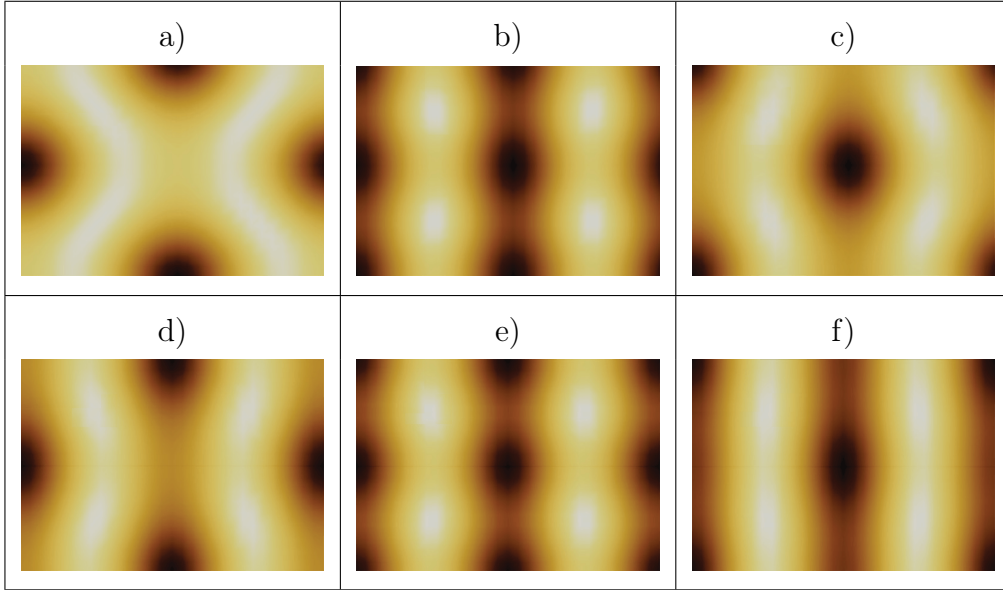


Figure 3.1.6: Comparison of simulated STM images of the W(110) surface using our model with an *s*-type tip (a)–(c) and the Tersoff-Hamann model (d)–(f) at $V = -0.25$ V bias voltage. The scan area corresponds to the rectangle shown in Fig. 3.1.1. Light and dark areas denote higher and lower apparent heights, respectively. The apparent heights of the W atom (z_T), and the corrugation of the contours ($\Delta z'$) are as follows. Our model: (a) $z_T = 3.80$ Å, $\Delta z' = 0.23$ pm; (b) corrugation inversion, $z_T = 4.15$ Å, $\Delta z' = 0.10$ pm; and (c) $z_T = 4.35$ Å, $\Delta z' = 0.12$ pm. Tersoff-Hamann model: (d) $z_T = 3.80$ Å, $\Delta z' = 1.63$ pm; (e) corrugation inversion, $z_T = 4.21$ Å, $\Delta z' = 1.82$ pm; and (f) $z_T = 4.70$ Å, $\Delta z' = 1.79$ pm. Adapted from Ref. [P1]

that the images are in good qualitative agreement for the corresponding pairs. In Figs. 3.1.6(a) and 3.1.6(d), at a tip-sample distance of about 3.80 Å, the apparent height of the W atom is larger than the one of the hollow position, *i.e.*, $\Delta z = z_T - z_H > 0$. This resembles normal corrugation. Moving the tip farther from the surface, we obtain the corrugation inversion and striped images. These are shown in Figs. 3.1.6(b) and (e). We find that our method reproduces the corrugation-inversion effect at almost the same tip-sample distance (4.15 Å) as the Tersoff-Hamann model predicts (4.21 Å). Increasing the tip-sample distance further, we enter the anticorrugation regime, and the apparent height of the W atom is smaller than the one of the hollow position, *i.e.*, $\Delta z = z_T - z_H < 0$. Such images are shown in Figs. 3.1.6(c) and (f). Note that all of the simulated STM images in Fig. 3.1.6 are in good qualitative agreement with [45]. The corrugation of the individual current contours has also been calculated: $z' = 0.23$ pm [Fig. 3.1.6(a)], $z' = 0.10$ pm [Fig. 3.1.6(b)], $z' = 0.12$ pm [Fig. 3.1.6(c)], $z' = 1.63$ pm

[Fig. 3.1.6(d)], $z' = 1.82$ pm [Fig. 3.1.6(e)], and $z' = 1.79$ pm [Fig. 3.1.6(f)]. We find that our model gives approximately one order of magnitude less corrugation than the Tersoff-Hamann method. Note, however, that the small corrugation amplitudes using our method are in good agreement with [45], where they report $z' < 1$ pm, close to the contrast reversal.

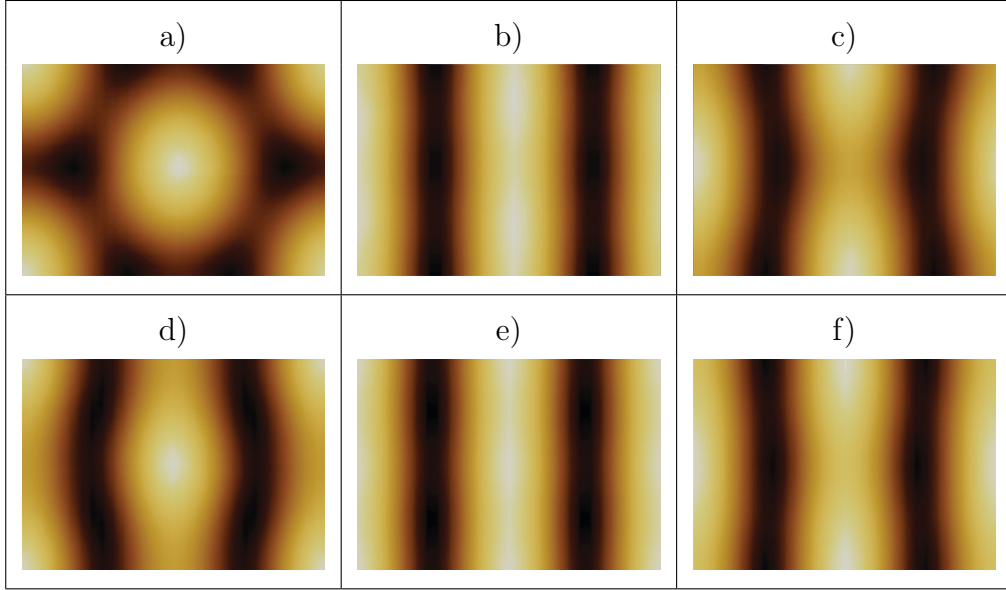


Figure 3.1.7: Comparison of simulated STM images of the W(110) surface using our model (a)–(c) and the Bardeen method (d)–(f) with the W(110) tip at $V = -0.25$ V bias voltage. The scan area corresponds to the rectangle shown in Fig. 3.1.1. Light and dark areas denote higher and lower apparent heights, respectively. The current values (I), the apparent heights of the W atom (z_T), and the corrugation of the contours (z') are as follows. Our model: (a) $I = 6.3$ nA, $z_T = 4.50$ Å, $z' = 0.36$ pm; (b) corrugation inversion, $I = 0.43$ nA, $z_T = 5.80$ Å, $z' = 0.02$ pm; and (c) $I = 0.35$ nA, $z_T = 5.90$ Å, $z' = 0.02$ pm. Bardeen method: (d) $I = 4.4$ nA, $z_T = 4.50$ Å, $z' = 0.07$ pm; (e) corrugation inversion, $I = 0.7$ nA, $z_T = 5.55$ Å, $z' = 0.03$ pm; and (f) $I = 0.19$ nA, $z_T = 6.25$ Å, $z' = 0.02$ pm. Adapted from Ref. [P1]

As we have seen, the corrugation-inversion effect already occurs considering the electronic structure of the sample only. However, Fig. 3.1.5 indicates that different tips can modify its tip-sample distance and bias-voltage dependence quite dramatically. In Fig. 3.1.7 STM images are compared using our model [Figs. 3.1.7(a)–(c)] to those calculated by the Bardeen method [Figs. 3.1.7(d)–(f)], explicitly taking the electronic structure of the W(110) tip in both cases into account. We find that the images are in good qualitative agreement for the pairs Figs. 3.1.7(b) and (e) and Figs. 3.1.7(c) and (f). In Figs. 3.1.7(a) and (d), at a tip-sample distance of about 4.50 Å, the agreement is weaker; however, the

normal corrugation is more pronounced in our model: The corrugation amplitude of Fig. 3.1.7(a), $z' = 0.36$ pm, is much larger than that of Fig. 3.1.7(d), $z' = 0.07$ pm. Moreover, as the current values of 6.3 nA (our model) and 4.4 nA (Bardeen model) are comparable to each other at the given tip-sample separation, the choice of $\eta = 1$ eV²m⁶ in Eq. (2.2.4) is confirmed. Note that by employing our model, a better qualitative agreement to the image of Fig. 3.1.7(d) has been found at a larger tip-sample separation, *i.e.*, closer to the corrugation inversion. This inversion is demonstrated in Figs. 3.1.7(b) and (e). Again, we obtain striped images. Note, however, that the stripes with larger apparent height correspond to the atomic rows, in contrast to what has been found in Figs. 3.1.6(b) and (e), where the atomic and hollow sites appeared as depressions. This difference is definitely due to the effect of the W tip, which was not considered in Fig. 3.1.6. On the other hand, we find good agreement concerning the tip-sample distance of the corrugation inversion: 5.80 Å in our model, and 5.55 Å calculated by the Bardeen method. Figures 3.1.7(c) and (f) correspond to anticorrugated images. In this tip-sample distance regime the extremely small corrugation amplitudes are in good agreement between our model and the Bardeen method: $z' = 0.02$ pm in Figs. 3.1.7(b), (c), and (f), and $z' = 0.03$ pm in Fig. 3.1.7(e).

3.1.6 Computational efficiency

Finally, we compared computational times between our model and the Bardeen method, and found the following: Our orbital-dependent model used $30 \times 22 \times 150$ grid points, one CPU and consumed 229 seconds, while the Bardeen method in bSKAN code used $31 \times 10 \times 100$ grid points, four CPUs and consumed 173866 seconds. Normalizing to the same real-space grid points we obtain that our method is 2425 times faster using one CPU than using four CPUs for the Bardeen calculation. As the four CPUs' calculations are roughly 3.5 times faster than the calculations on one CPU in our computer cluster, a remarkable one-CPU equivalent time boost of about 8500 is obtained for our method compared to the Bardeen method for the given surface-tip combination. While the k -point samplings of the surface and tip Brillouin zones affect the computational time of the Bardeen method due to the enhanced number of transitions as the number of k -points increases, the computational time of our model is insensitive to the number of k -points as the PDOS of the tip apex and surface atoms are used. The

energy-dependent PDOS functions have the same data structure, no matter what the number of the constituting electron states obtained by the k -summation [29]. This is a great computational advantage of our model. Of course, the quality of the results depends on the k -point samplings. Moreover, please note the further potential that our method can be parallelized in the future.

3.1.7 The effect of arbitrary tip-orientation

Convergence properties

We report a similar convergence test for the tungsten tip comparing different tip orientations. To take into account a wide energy range around the Fermi level, we calculated the tunneling current at -2.0 and $+2.0$ V bias voltages at $z = 4.5$ Å above a surface W atom, and averaged these current values. The averaged currents were normalized for each tip calculation to obtain comparable results. The convergences of the normalized averaged current with respect to the lateral distance on the surface, $d_{||}$, characteristic for the number of atoms involved in the atom-superposition summation, are shown in Fig. 3.1.8.

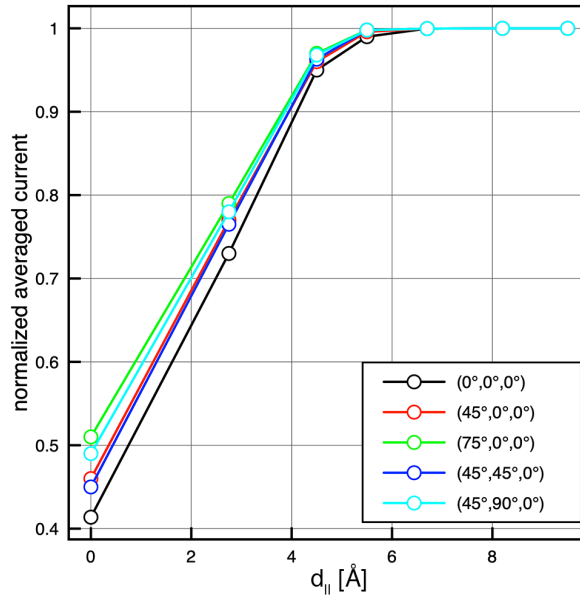


Figure 3.1.8: Convergence of the normalized averaged current $z = 4.5$ Å above the surface top (T) position (W atom) calculated with different tungsten tip orientations described by the Euler angles $(\vartheta_0, \varphi_0, \psi_0)$ given in degrees (see also Fig. 2.2.2). Adapted from Ref. [P2]

$d_{||}$ represents the radius of a surface section measured from the W atom below the tip apex, from which area the surface atomic contributions to the tunneling

importance in the tunneling as the tilting increases, since they can hybridize easily with the dominant orbitals of the sample: s , p_z , and $d_{3z^2-r^2}$. This finding is demonstrated in the top right part of Fig. 3.1.9. Concomitantly, the tip p_z and $d_{3z^2-r^2}$ orbitals lose their contribution, as they give a transmission maximum in the z' direction that is not in line with z because of the tilting. Starting from the $(45^\circ, 0^\circ, 0^\circ)$ tip orientation, we can rotate the tip around the sample z direction with angles $\psi_0 \in [0^\circ, 90^\circ]$. We find that this type of rotation does not considerably affect the convergence character of the current compared to the $(45^\circ, 0^\circ, 0^\circ)$ orientation (not shown). This is due to the practically unchanged dominant current contributions by rotating with ψ_0 (see the bottom left part of Fig. 3.1.9). On the other hand, rotating the local tip coordinate system around z' , *i.e.*, changing φ_0 , results in slight convergence changes. First, the convergence speed drops slightly at $(45^\circ, 45^\circ, 0^\circ)$, and then increases at the orientation $(45^\circ, 90^\circ, 0^\circ)$. This effect is related to the tip d_{xz} and d_{yz} orbitals, as their contribution changes the most by this type of rotation (see also the bottom right part of Fig. 3.1.9). We found that the tip rotation effects do not change the suggestion that atom contributions within at least $d_{||} = 3a_W \approx 9.5 \text{ \AA}$ distance from the surface-projected tip position have to be considered, as we have also seen in Sec. 3.1.2. The reason is that the exponentially decaying part of the transmission function is dominant over the orbital-dependent part. In the case of calculating STM images, $d_{||} = 3a_W \approx 9.5 \text{ \AA}$ has to be measured from the edge of the scan area in all directions to avoid distortion of the image, thus involving 67 surface atoms in the atomic superposition. For brevity, in the following we use the same surface atoms to calculate single-point tunneling properties as well.

Orbital contributions

Let us analyze the tip orientation effects on the relative importance of selected $\beta \leftrightarrow \gamma$ transitions in determining the total tunneling current above a surface W atom. The $\tilde{I}_{\beta\gamma}$ relative current contributions can be calculated according to Eq. 3.1.3. This quantity gives the percentage contribution of the individual transition to the total tunneling current. Fig. 3.1.9 shows selected relative current contributions using the tungsten tip at a bias voltage $V = -0.1 \text{ V}$ and distance $z = 4.5 \text{ \AA}$ above a surface W atom. Note that only those transitions are reported which have either a significant contribution, or show considerable changes upon the tip rotations. We find that by rotating the tip using ψ_0 around the $z' = z$

axis (top left part of Fig. 3.1.9), the dominant contributions are due to the tip $d_{3z'^2-r'^2}$ orbital combined with the sample s , p_z , and $d_{3z^2-r^2}$ orbitals, and they do not change by the mentioned tip rotation. On the other hand, the $d_{yz} - d_{yz}$ and $d_{xz} - d_{xz}$ contributions lose, while the $d_{yz} - d_{xz}$ and $d_{xz} - d_{yz}$ gain importance upon this type of tip rotation. The top right part of Fig. 3.1.9 corresponds to rotations around the $x' = x$ axis with ϑ_0 , and the evolution of the dominant contributions. It can be seen that the dominant sample contributions remain unchanged, *i.e.*, they are the s , p_z , and $d_{3z^2-r^2}$ orbitals, while the dominant tip orbitals change from $d_{3z'^2-r'^2}$ at $(0^\circ, 0^\circ, 0^\circ)$ to d_{yz} at $(45^\circ, 0^\circ, 0^\circ)$, and to $d_{x^2-y^2}$ at $(75^\circ, 0^\circ, 0^\circ)$. The bottom left part of Fig. 3.1.9 shows the relative current contribution changes with respect to tip rotations by ψ_0 around the sample z direction, starting from the $(45^\circ, 0^\circ, 0^\circ)$ orientation. We find that this type of rotation does not affect the dominant current contributions with d_{yz} tip orbital character. The biggest changes in other transitions are found for the sample d_{yz} orbital, *i.e.*, the contributions in combination with the tip d_{xy} , d_{yz} , and d_{xz} orbitals slightly increase, while the $d_{yz} - d_{3z^2-r^2}$ and $d_{yz} - d_{x^2-y^2}$ transitions show decreasing importance upon this kind of tip rotation. Finally, by rotating the local tip coordinate system around the z' axis with φ_0 starting from the $(45^\circ, 0^\circ, 0^\circ)$ orientation results in decreased d_{yz} and increased d_{xz} contributions in combination with the sample s , p_z , and $d_{3z^2-r^2}$ orbitals. This is shown in the bottom right part of Fig. 3.1.9. It is interesting to find that the $d_{3z^2-r^2} - s$ relative contribution increases by rotating φ_0 . This, however, does not mean an absolute increment of this current contribution since the tip s state is insensitive to the rotation.

Atomic contrast changes

We have seen in Sec. 3.1.4 that changing the bias voltage or tip-sample distance can result in contrast inversion of the STM images ($I = \text{const. contours}$). Now we demonstrate that tip rotation effects also play an important role in the formation of the STM image.

Figure 3.1.10 shows tip rotation effects on the $\Delta I(z, V) = 0$ contours in the $[0 \text{ \AA}, 14 \text{ \AA}]$ tip-sample distance and $[-2 \text{ V}, +2 \text{ V}]$ bias voltage range. We find that by rotating the tip using ψ_0 around the $z' = z$ axis (top left part of Fig. 3.1.10), the contours shift to larger tip-sample distances close to zero bias, and their shapes remain qualitatively unchanged. It is interesting to see

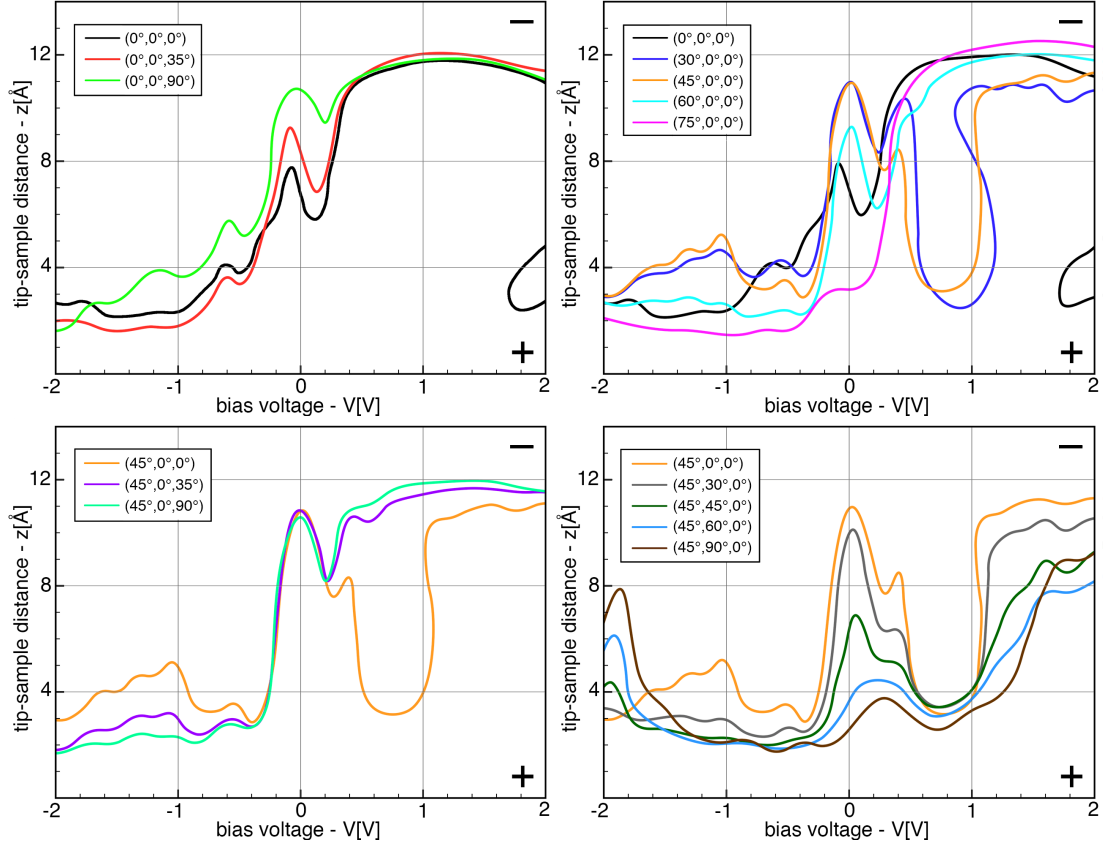


Figure 3.1.10: $\Delta I(z, V) = 0$ contours indicative of the relative apparent heights of the surface top (T) and hollow (H) positions (see equation (3.1.4), and its meaning in the text) calculated using a tungsten tip with different tip orientations described by the Euler angles $(\vartheta_0, \varphi_0, \psi_0)$ given in degrees (see also Fig. 2.2.2). The sign of $\Delta I(z, V)$ (+ or -) is explicitly shown at the corners on the right hand side of each part of the figure: it is positive below the curves, and negative above them. Adapted from Ref. [P2]

that the $\Delta I(z, V) < 0$ region found for the $(0^\circ, 0^\circ, 0^\circ)$ tip orientation at around $z = 3.5 \text{ \AA}$ close to $+2 \text{ V}$ disappears with this type of tip rotation. The same finding is obtained in the top right part of Fig. 3.1.10, which corresponds to rotations around the $x' = x$ axis using ϑ_0 . Here, the quality of the contours change considerably. The $(30^\circ, 0^\circ, 0^\circ)$ and $(45^\circ, 0^\circ, 0^\circ)$ tip orientations result in $I(z, V) = 0$ contours at enlarged tip-sample distances close to zero bias, and a $\Delta I(z, V) < 0$ region opens at small tip-sample distances between bias voltages of $+0.5 \text{ V}$ and $+1 \text{ V}$. On further rotation this region disappears, and concomitantly the contours shift to lower tip-sample distances close to $V = 0 \text{ V}$. For the $(75^\circ, 0^\circ, 0^\circ)$ tip orientation, we obtain $\Delta I(z, V) < 0$ at $z > 3.5 \text{ \AA}$ around zero bias. The bottom left part of Fig. 3.1.10 shows the evolution of the $\Delta I(z, V) = 0$ contours with respect to tip rotations by ψ_0 around the sample z direction starting from

the $(45^\circ, 0^\circ, 0^\circ)$ orientation. The contours do not change considerably close to $V = 0$ V, but the $\Delta I(z, V) < 0$ region at small tip-sample distances between +0.5 V and +1 V disappears. Finally, the effect of the rotation of the local tip coordinate system around the z' axis with φ_0 starting from the $(45^\circ, 0^\circ, 0^\circ)$ orientation is shown in the bottom right part of Fig. 3.1.10. The contours are shifted to lower tip-sample distances close to zero bias and at high positive bias voltages, whereas the shift is towards larger tip-sample distances at high negative bias. Moreover, this type of rotation does not affect the presence of the $\Delta I(z, V) < 0$ region at small tip-sample distances between +0.5 V and +1 V. As was suggested earlier, particular tip nodal planes restrict the collection of surface atom contributions to specific regions on the sample surface. By changing the tip-sample distance, the orientational overlaps between the tip and sample orbitals change, and according to our model some localized orbitals gain more importance in the tunneling contribution (see also Fig. 3.1.9). The complex tip-sample distance, bias voltage, and tip orientation dependent effect of the real-space orbitals on the tunneling can be visualized as the zero contours of the current difference between tip positions above the surface top and hollow sites, as shown in Fig. 3.1.10.

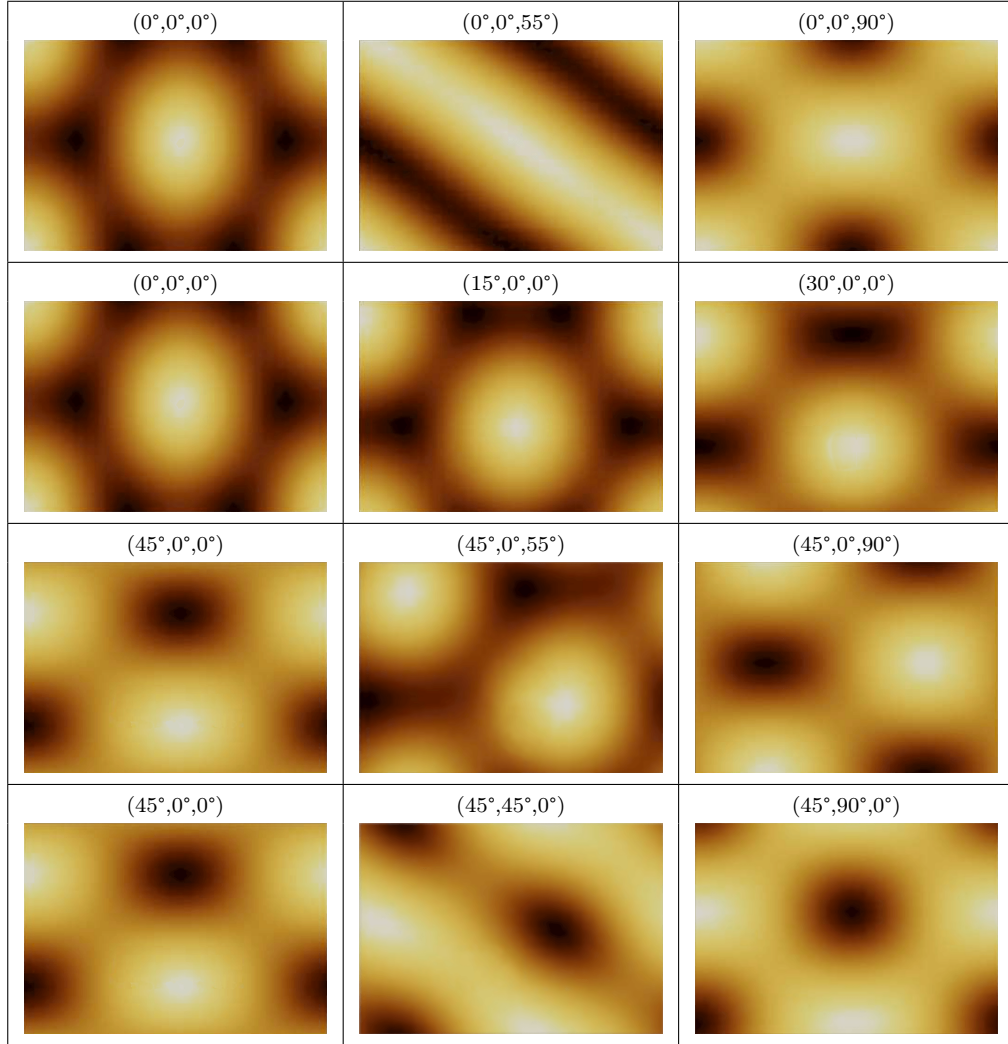


Figure 3.1.11: Tip orientation effect on the simulated STM images: Constant-current contours at $I = 6.3$ nA and $V = -0.25$ V bias voltage about $z = 4.5$ Å above the W(110) surface, using the tungsten tip with different orientations described by the Euler angles $(\vartheta_0, \varphi_0, \psi_0)$ given in degrees (see also Fig. 2.2.2). The scan area corresponds to the rectangle shown in Fig. 3.1.1. Light and dark areas denote larger and smaller apparent heights, respectively. Adapted from Ref. [P2]

To demonstrate the atomic contrast changes depending on the tip orientation $(\vartheta_0, \varphi_0, \psi_0)$ more clearly, constant-current STM images are simulated. The scan area is the rectangular section shown in Fig. 3.1.1. Selected results obtained at $I = 6.3$ nA current and $V = -0.25$ V bias voltage are shown in Fig. 3.1.11. These tunneling parameters correspond to a tip-sample distance of $z = 4.5$ Å above the surface W atoms, and with an unrotated tip a normal corrugation is expected, see Sec. 3.1.4. Moving the unrotated tip farther from the surface results in lower tunneling currents, and the atomic contrast is inverted at $I = 0.43$ nA ($z = 5.8$

Å), in reasonable agreement with calculations employing the Bardeen tunneling model (Sec. 3.1.5). Alternatively, a corrugation inversion can be observed at a fixed tip-sample distance by changing the bias voltage. Such an effect was reported in [45], where $z = 4.6$ Å was assumed. We find that by rotating the tip with ψ_0 around the $z' = z$ axis (top row of Fig. 3.1.11), the elongated feature located on the W atoms initially in the y direction is rotated. This results in a striped image for the $(0^\circ, 0^\circ, 55^\circ)$ tip orientation. The stripes with larger apparent height correspond to the atomic rows and are oriented along the diagonal of the rectangle. Turning the tip to the $(0^\circ, 0^\circ, 90^\circ)$ orientation, the elongated feature located on the W atoms turns to the x direction. The reason is the rearrangement of the importance of the $d_{yz} - d_{yz}$ and $d_{xz} - d_{xz}$ transitions towards the $d_{yz} - d_{xz}$ and $d_{xz} - d_{yz}$ transitions upon this type of rotation, as shown in Fig. 3.1.9. Tip rotation around the $x' = x$ axis using ϑ_0 results in apparent atom positions shifted towards the bottom edge of the image, *i.e.*, towards the $-y$ direction. This effect is demonstrated for the set of images with $(0^\circ, 0^\circ, 0^\circ)$ to $(45^\circ, 0^\circ, 0^\circ)$ tip orientations (second row, and first image of the third row of Fig. 3.1.11). During this rotation the dominant tip orbital character changes from $d_{3z^2-r^2}$ to d_{yz} (see Fig. 3.1.9). The third row of Fig. 3.1.11 shows the effect of tip rotations by ψ_0 around the sample z direction starting from the $(45^\circ, 0^\circ, 0^\circ)$ orientation. We find that the apparent atom positions that were shifted away towards the $-y$ direction are now rotated on the images with respect to the z axis centered on the real W atom positions. The STM image corresponding to the $(45^\circ, 0^\circ, 55^\circ)$ tip orientation shows apparent W atom positions shifted along the diagonal of the rectangle with respect to the real atomic positions. Similarly, the $(45^\circ, 0^\circ, 90^\circ)$ tip orientation corresponds to apparent W atom positions shifted towards the $+x$ direction. As was shown in Fig. 3.1.9, the tip d_{yz} orbital is always dominant, and the biggest changes are found for the sample d_{yz} orbital contributions upon this type of rotation. The last row of Fig. 3.1.11 considers the tip rotation around the z' axis by φ_0 starting from the $(45^\circ, 0^\circ, 0^\circ)$ orientation. The obtained complex rearrangement of apparent atom positions on the STM images is due to the changing effect of the d_{yz} and d_{xz} contributions of the tunneling tip, as demonstrated in Fig. 3.1.9.

3.2 Fe(110)

In the previous chapter we have seen that in non-magnetic STM, at certain bias voltage and tip-sample distance ranges, constant-current STM images can show atomic contrast inversion above flat metal surfaces, and tip-rotational effects can also play an important role. This phenomenon was widely studied in the literature [16, 52, 45, P1, P2]. Chen theoretically explained the corrugation inversion found on low Miller index metal surfaces by the presence of $m \neq 0$ tip states [28]. On the other hand, Heinze *et al.* [45] pointed out that a competition between electron states from different surface Brillouin zone parts is responsible for the corrugation inversion effect. A similar explanation was given on the contrast inversion above the magnetic Fe(001) surface in the presence of an external electric field [47]. Following the real-space electron orbital picture, we expect that beside orbital-dependent effects magnetic characteristics also play an important role in the determination of the corrugation quality of SP-STM images on magnetic surfaces. This expectation is supported by the reported bias voltage dependent magnetic contrast reversals in two different magnetic systems [53, 29] obtained by using spherical tunneling models. Note that the magnetic effect can be tuned in different ways, *e.g.*, the magnetic contrast can be enhanced by properly adjusting the bias voltage and/or the tip magnetization direction [54], or by using chemically modified magnetic STM tips [55].

To capture the effect of magnetic characteristics we can separate the topographic (TOPO) and magnetic (MAGN) part of the total STM current:

$$I(\mathbf{r}_T, V) = I_{TOPO}(\mathbf{r}_T, V) + I_{MAGN}(\mathbf{r}_T, V), \quad (3.2.1)$$

where the two components – using Eq. (2.2.4) – are the following:

$$\begin{aligned} I_{TOPO}(\mathbf{r}_T, V) &= \frac{2e^2}{h} \eta \sum_i \sum_{\beta, \gamma} \int_0^{eV} T_{\beta\gamma}(\kappa, \mathbf{r}_T - \mathbf{r}_i) \times \\ &\times \tilde{n}_\beta^S(\mathbf{r}_i, E_F^S + E) \tilde{n}_\gamma^T(\mathbf{r}_T, E_F^T + E - eV) dE, \end{aligned} \quad (3.2.2)$$

$$\begin{aligned}
I_{MAGN}(\mathbf{r}_T, V) &= \frac{2e^2}{h} \eta \sum_i \sum_{\beta, \gamma} \int_0^{eV} T_{\beta\gamma}(\kappa, \mathbf{r}_T - \mathbf{r}_i) \times \\
&\times \tilde{\mathbf{m}}_{\beta}^S(\mathbf{r}_i, E_F^S + E) \cdot \tilde{\mathbf{m}}_{\gamma}^T(\mathbf{r}_T, E_F^T + E - eV) dE. \quad (3.2.3)
\end{aligned}$$

Using these quantities a similar investigation can be performed as it was done in the case of W(110).

3.2.1 Computational details

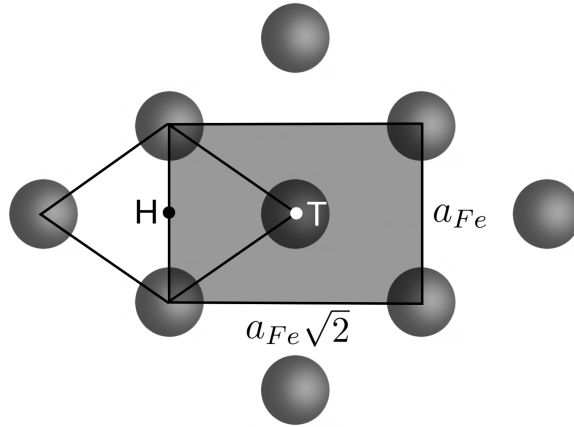


Figure 3.2.1: The surface unit cell of Fe(110) (rhombus) and the rectangular scan area (shaded) for the tunneling current simulations. Grey spheres denote the Fe atoms. The top (T) and hollow (H) positions are explicitly shown.

We particularly focus on tip effects, and consider ideal magnetic tip models with different orbital symmetries, and a more realistic iron tip. The effect of three different tip magnetization orientations is also investigated. We choose 27 Fe(110) surface atoms involved in the atomic superposition in combination with the ideal tips, and 112 Fe(110) surface atoms combined with the iron tip including the simulation of SP-STM images. We performed geometry relaxation and electronic structure calculations within the generalized gradient approximation (GGA) of the density functional theory implemented in VASP [42]. A plane wave basis set for electronic wave function expansion in combination with the projector augmented wave (PAW) method [48] was applied, and the exchange-correlation functional is parametrized by Perdew and Wang (PW91) [49]. The electronic structures of the sample surface and the tip were calculated separately.

We model the Fe(110) surface by a slab of nine atomic layers with the theoretically determined lattice constant of $a_{Fe} = 2.829 \text{ \AA}$, obtained at the total energy minimum of a bulk body-centered cubic Fe cell, in agreement with Ref. [56]. In the surface slab calculations we set up a separating vacuum region of 24 \AA width in the surface normal (z) direction between neighboring supercell slabs to minimize slab–slab interaction. After geometry relaxation the Fe–Fe interlayer distance between the two topmost layers is reduced by 0.39%, and the underneath Fe–Fe interlayer distance is increased by 0.36% in comparison to bulk Fe. These are in excellent agreement with the findings of Ref. [56]: -0.36% , and $+0.46\%$, respectively. The size of the in-plane magnetic moment of the surface Fe atoms is $2.50 \mu_B$, in agreement with Refs. [56, 45]. The unit cell of the Fe(110) surface (rhombus) and the rectangular scan area for the tunneling current simulations are shown in Fig. 3.2.1 where the surface top (T) and hollow (H) positions are explicitly indicated. The average electron work function above the Fe(110) surface is $\phi_S = 4.84 \text{ eV}$ calculated from the local electrostatic potential. We used a $41 \times 41 \times 5$ Monkhorst–Pack [50] k -point grid for obtaining the orbital-decomposed projected charge and magnetization electron DOS onto the surface Fe atom, $\tilde{n}^S(E)$ and $\tilde{\mathbf{m}}^S(E)$, respectively.

We used three different tip models: ideal magnetic tip models with a particular γ_0 orbital symmetry where the PDOS of the tip is energy-independent: $n_{T_{\gamma_0}} = 1(\text{eV})^{-1}$ and $n_{T_{(\gamma \neq \gamma_0)}} = 0$. Another characteristic for ideal magnetic tips is that their absolute spin polarization is maximal ($|P_T| = |m_T|/n_T = 1$) in the full energy range, *i.e.*, combined with a particular γ_0 orbital symmetry: $\mathbf{m}_{T_{\gamma_0}} = 1(\text{eV})^{-1} \mathbf{e}_T$ (\mathbf{e}_T is the unit vector of the tip spin quantization axis that is parallel to the assumed tip magnetization direction, an input parameter in our method) and $\mathbf{m}_{T_{(\gamma \neq \gamma_0)}} = 0$. We took $\gamma_0 \in \{s, p_z, d_{3z^2-r^2}\}$ tip orbital symmetries into consideration.

More realistic tips can be employed by explicitly calculating the orbital decomposition of the tip apex PDOS in model tip geometries. In the present work a blunt iron tip is used, where a single Fe apex atom is placed on the hollow position of the Fe(001) surface, similarly as in Ref. [57]. We took an Fe(001) slab consisting of nine atomic layers with the theoretically determined lattice constant of $a_{Fe} = 2.829 \text{ \AA}$, and placed an adatom on each side of a 3×3 surface cell. A separating vacuum region of 20 \AA width in the surface normal direction was chosen to minimize slab–slab interaction. After geometry relaxation of the adatom

and the first surface layer performed by the VASP code, the orbital-decomposed electronic structure data projected to the tip apex atom, $n_{T_\gamma}(E)$ and $\mathbf{m}_{T_\gamma}(E)$, were calculated using a $13 \times 13 \times 3$ Monkhorst-Pack k -point grid. We obtained the local electron work function of $\phi_T = 3.96$ eV above the iron tip apex atom that was used in the tunneling simulations.

3.2.2 Electronic structure and current histograms

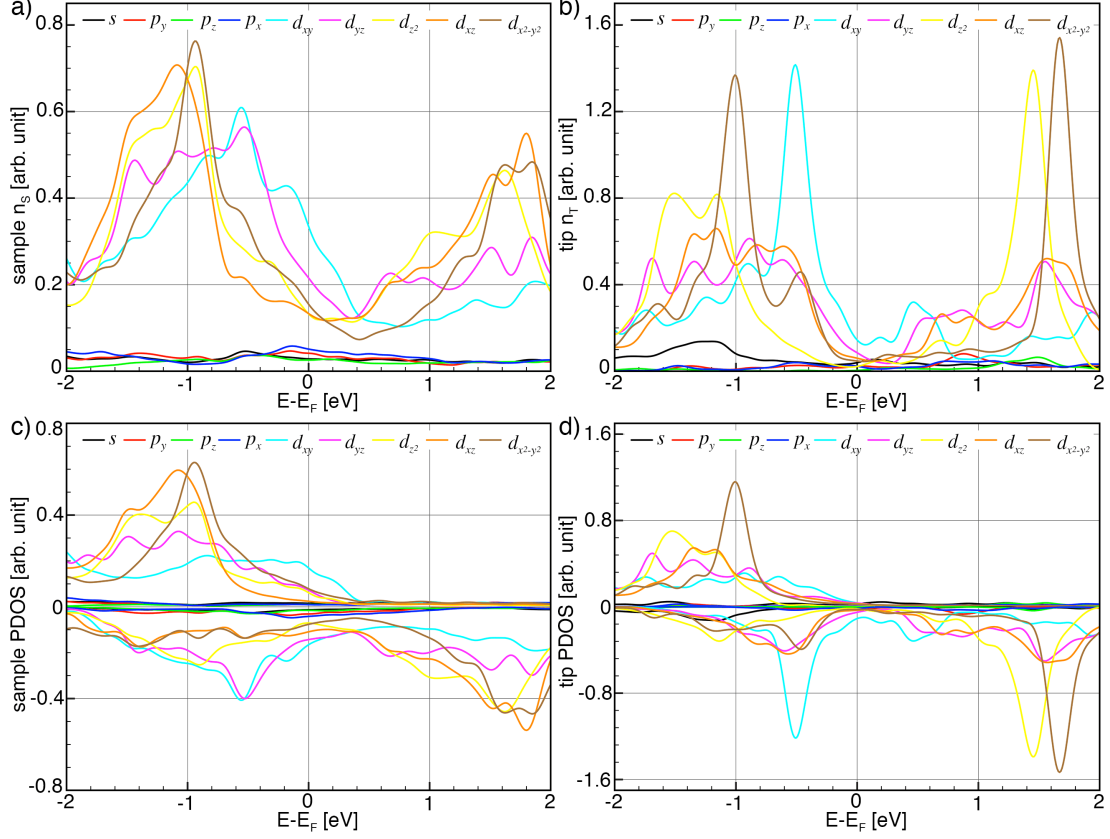


Figure 3.2.2: Orbital-decomposed projected electron density of states (PDOS) of the Fe(110) surface atom and the iron tip apex atom. (a) surface charge PDOS: $\tilde{n}_\beta^S(E)$; (b) tip charge PDOS: $\tilde{n}_\gamma^T(E)$; (c) surface spin-resolved $\tilde{n}_\beta^{S\uparrow\downarrow}(E)$; (d) tip spin-resolved $\tilde{n}_\gamma^{T\uparrow\downarrow}(E)$. Orbitals $\beta, \gamma \in \{s, p_y, p_z, p_x, d_{xy}, d_{yz}, d_{3z^2-r^2}, d_{xz}, d_{x^2-y^2}\}$ are indicated. Adapted from Ref. [P3]

Fig. 3.2.2 shows the energy-dependent orbital-decomposed charge (n) and spin-resolved (\uparrow, \downarrow) PDOS functions of the Fe(110) surface atom (S) and the Fe(001) tip apex atom (T) as follows: Fig. 3.2.2(a) $\tilde{n}_\beta^S(E)$, Fig. 3.2.2(b) $\tilde{n}_\gamma^T(E)$, Fig. 3.2.2(c) $\tilde{n}_\beta^{S\uparrow\downarrow}(E)$, Fig. 3.2.2(d) $\tilde{n}_\gamma^{T\uparrow\downarrow}(E)$, with tip and sample orbitals $\beta, \gamma \in \{s, p_y, p_z, p_x, d_{xy}, d_{yz}, d_{3z^2-r^2}, d_{xz}, d_{x^2-y^2}\}$. We find that the d partial PDOS is dominating over s and p partial PDOS with the exception of the majority spin (\uparrow) PDOS above the Fermi levels. The obtained results are in good agreement with Refs. [57, 45], where the full potential linearized augmented plane wave (FLAPW) method was employed.

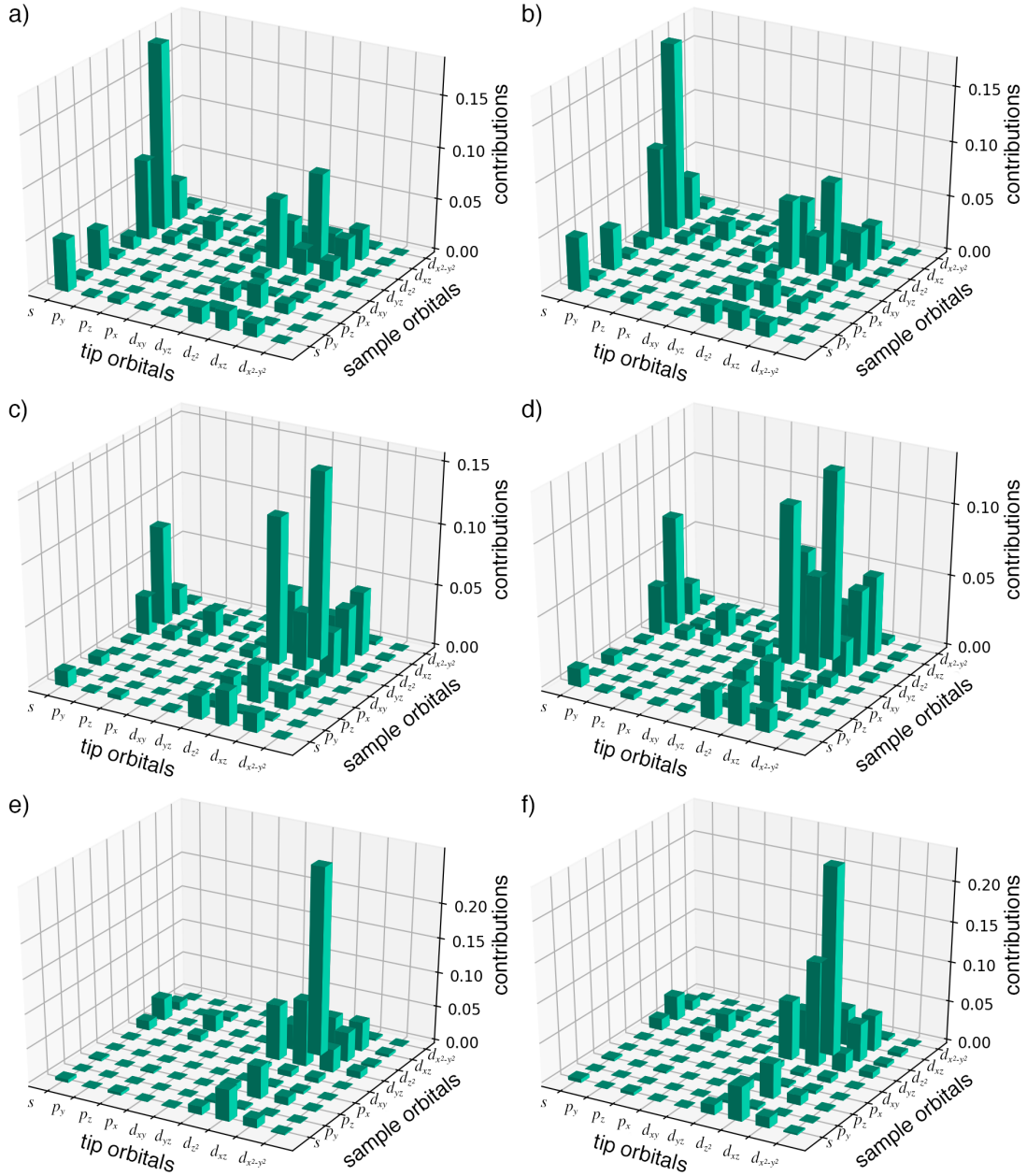


Figure 3.2.3: Histograms of the orbital-dependent relative current contributions ($\tilde{I}_{\beta\gamma}(\mathbf{r}_T, V)$ in Eq. (3.1.3)) using the iron tip placed $z = 5 \text{ \AA}$ above two Fe(110) surface positions [top (T) and hollow (H), see Fig. 3.2.1] at different bias voltages: (a) T position, $V = -0.1 \text{ V}$; (b) H position, $V = -0.1 \text{ V}$; (c) T position, $V = -1.0 \text{ V}$; (d) H position, $V = -1.0 \text{ V}$; (e) T position, $V = -2.0 \text{ V}$; (f) H position, $V = -2.0 \text{ V}$. Adapted from Ref. [P3]

The relative contributions of all $\beta \leftrightarrow \gamma$ orbital-dependent transitions to the total tunneling current, $\tilde{I}_{\beta\gamma}(\mathbf{r}_T, V)$, can be calculated according to Eq. (3.1.3). Fig. 3.2.3 shows representative histograms at different bias voltages and iron tip positions above the Fe(110) surface. We set the tip magnetization parallel to the in-plane Fe(110) surface magnetic moment. Parts (a) and (b) of Fig. 3.2.3 correspond to the tip apex $z = 5 \text{ \AA}$ above the surface top (T) and hollow (H) positions, respectively (for T and H see Fig. 3.2.1), and the bias voltage is set to $V = -0.1 \text{ V}$. We find that the tip s orbital provides the dominating contributions combined with the sample d_{yz} and $d_{3z^2-r^2}$ orbitals. The $d_{3z^2-r^2} - d_{3z^2-r^2}$ and $d_{yz} - d_{yz}$ transitions also give sizable contributions. The main difference between the T and H tip positions is that above the Fe(110) hollow site the $d_{yz} - d_{3z^2-r^2}$ contributions gain, while the $d_{3z^2-r^2} - d_{3z^2-r^2}$ contribution loses weight, similarly to the finding above the W(110) surface. This is due to the different orientational overlap of the mentioned tip and sample orbitals at the two tip positions, and it is not affected by the bias voltage. On the other hand, at a larger negative bias $V = -1.0 \text{ V}$ [Fig. (3.2.3)(c) and (d)] we observe that the tip s orbital loses and the d_{yz} , $d_{3z^2-r^2}$, and d_{xz} orbitals and their tip-sample combinations gain weight. The largest contribution is now found for the $d_{3z^2-r^2} - d_{3z^2-r^2}$ transition. We find an enhancement of this effect at $V = -2.0 \text{ V}$ Fig. 3.2.3(e and f), and here the tip s orbital contributions are tiny. This bias-trend can be explained by the surface and tip partial charge PDOS in Fig. 3.2.2. At large negative bias voltages the combination of the surface occupied d partial PDOS with the tip unoccupied d partial PDOS clearly dominates over the tip s partial contributions. We find similar trends for a tip magnetization perpendicular to the surface, and also for positive bias voltages (consider the combination of the surface unoccupied with the tip occupied d partial charge PDOS in Fig. 3.2.2).

3.2.3 Contrast inversion

As demonstrated in Sec 3.1, the current difference between tip positions above the top (T) and hollow (H) surface sites is indicative for the corrugation character of a constant-current STM image. The total (TOPO + MAGN) current difference at tip-sample distance z and bias voltage V is defined as $\Delta I(z, V) = I_T(z, V) - I_H(z, V)$. Positive $\Delta I(z, V)$ corresponds to an STM image with normal corrugation where the atomic sites appear as protrusions, and negative $\Delta I(z, V)$

to an inverted STM image with anticorrelation and atomic sites appearing as depressions. The $\Delta I(z, V) = 0$ contour gives the (z, V) combinations where the corrugation inversion occurs. Fig. 3.2.4 shows such zero current difference

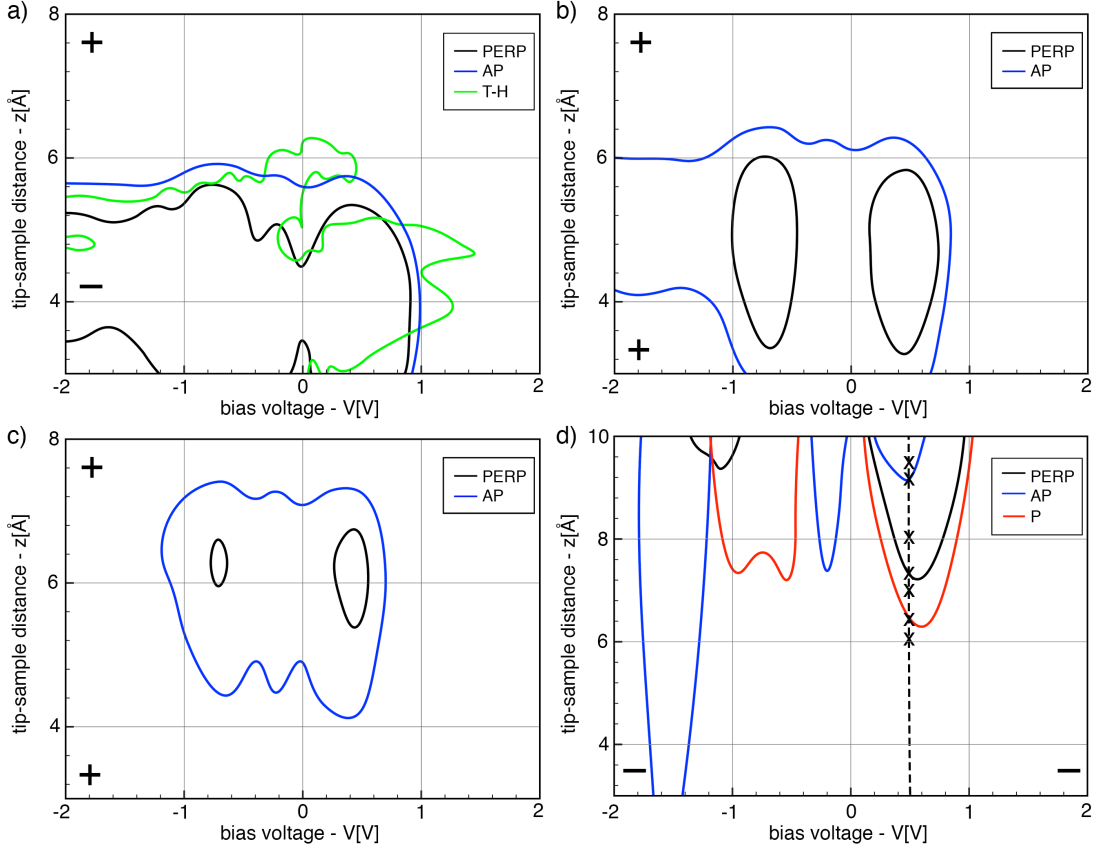


Figure 3.2.4: The $\Delta I(z, V) = I_T(z, V) - I_H(z, V) = 0$ contours indicative for the corrugation inversion calculated with four tip models above the Fe(110) surface: (a) s -tip, (b) p_z -tip, (c) $d_{3z^2-r^2}$ -tip, and (d) Fe(001)-tip. The tip magnetization directions are explicitly shown with respect to the Fe(110) surface magnetic moment: parallel (P), perpendicular (PERP), and antiparallel (AP). For comparison, the $\Delta I(z, V) = 0$ curves are shown in (a) obtained by using the Tersoff–Hamann (T–H) approach. The sign of ΔI (+ or –) is shown in selected (z, V) sections, and crossing the $\Delta I(z, V) = 0$ curve always means inversion of the sign. Note that positive $\Delta I(z, V)$ corresponds to normal, and negative to inverted atomic contrast in the SP–STM images, see also Fig. 3.2.5. In (d) seven crosses at 0.5 V mark the apparent heights of the Fe atom on the constant-current contours shown in Fig. 3.2.5. Adapted from Ref. [P3]

contours calculated with four different tip models and three tip magnetization orientations (parallel (P), perpendicular (PERP), and antiparallel (AP) with respect to the Fe(110) surface magnetic moment) in the $[-2 \text{ V}, +2 \text{ V}]$ bias voltage range. We consider the $[3 \text{ \AA}, 8 \text{ \AA}]$ tip-sample distance regime in Fig. 3.2.4(a–c) for the ideal tips with s , p_z , and $d_{3z^2-r^2}$ orbital character, respectively, and the $[3 \text{ \AA}, 10 \text{ \AA}]$ range in Fig. 3.2.4(d) for the iron tip. Note that the validity of our

tunneling model is restricted to about $z > 3.5 \text{ \AA}$. Let us first focus on the zero current difference contours obtained by the s -tip in Fig. 3.2.4(a). The contrast inversion of the Fe(110) surface with an s -tip at a fixed $z = 4.5 \text{ \AA}$ tip-sample distance was already studied with a different theoretical approach by Heinze *et al.* in Ref. [45]. Comparing these results with ours we find good qualitative agreement: The P tip magnetization does not show any contrast inversion in the studied (z, V) range. This corresponds to the majority spin+ data of Fig. 15 in Ref. [45]. On the other hand, the PERP and AP tip magnetizations result in $\Delta I(z, V) = 0$ curves shifted away from each other, and the direction of the shift qualitatively agrees with the findings of Ref. [45]. Note, however, that the corrugation inversions at $z = 4.5 \text{ \AA}$ are found at different bias voltages: 0.87 V (our model, PERP) vs. 0.4 V (Total, Fig. 15 in Ref. [45]), and 0.94 V (our model, AP) vs. 0.7 V (minority spin-, Fig. 15 in Ref. [45]). This difference can be attributed to the nonequal lattice constants used and the different theoretical approaches. As a further test of the reliability of our tunneling model, we compared the $\Delta I(z, V) = 0$ contour using the PERP tip magnetization with that obtained by the Tersoff–Hamann method, the curve denoted by T–H in Fig. 3.2.4(a). We find that our model reproduces the (z, V) region with the inverse corrugation denoted by the ‘-’ sign qualitatively well. Quantitative agreement is not present due to the approximations in the 3D-WKB method. Note that the PERP tip magnetization corresponds to an equal 0.5–0.5 weighting of the majority and minority spin channels contributing to the tunneling and, thus, to a zero spin-polarized (MAGN) contribution of the current ($I_{MAGN} = 0$, $I = I_{TOPO}$), and solely orbital-dependent effects play a role in the tunneling without spin-polarization effects. Altogether, the results obtained by the s -tip indicate that the Fe(110) surface always appears to be normally corrugated taking a P tip magnetization with respect to the surface magnetic moment, whereas changing the tip magnetization to PERP and AP result in anticorrugation below about 1 V bias and 6 \AA tip-sample distance.

To understand these results, we give the following interpretation: it is known that there is a competition between the tunneling contributions from $m = 0$ ($s, p_z, d_{3z^2-r^2}$) and $m \neq 0$ orbitals in the formation of the corrugation character of an STM image [28]. Generally, $m = 0$ states prefer normal corrugation, whereas $m \neq 0$ states prefer anticorrugation. Based on our model, we suggest that the corrugation inversion can be understood as an interplay of the real-space or-

orbital shapes involved in the tunneling and their corresponding energy-dependent partial PDOS. For the PERP Fig. 3.2.2(a) and AP [minority spin (\downarrow) in Fig. 3.2.2(c)] cases the d partial PDOS of the Fe(110) surface is dominating over the s and p partial PDOS in the whole energy range. Therefore, considering only d orbital shapes of the surface, the leading current contribution is expected from the $d_{3z^2-r^2}$ orbital of the underlying Fe atom when the tip is placed above the surface T position, and from the $d_{3z^2-r^2}$, d_{xz} , d_{yz} orbitals of the four nearest-neighbor surface Fe atoms when the tip is above the surface H position. Note that the weight of d_{yz} is larger than of d_{xz} due to the geometry of the (110) surface, see Fig. 3.2.1. By changing the tip-sample distance there is a competition between the contributions of these d states due to the orbital-dependent transmission, and there is a range ($z < 6 \text{ \AA}$) where I_H dominates over I_T , thus anticorruagation is obtained. At large distances the d_{xz} , d_{yz} orbitals lose and the $d_{3z^2-r^2}$ orbital gains importance, and normal corrugation is found. This simple orbital-picture has to be combined with the energy-dependence of the PDOS of the contributing spin channels for an accurate interpretation. As can be seen in Fig. 3.2.2(a) and (c) (\downarrow), there is a large $d_{3z^2-r^2}$ -type PDOS peak at about 1.5 eV above the Fermi level. The existence of this PDOS feature results in the disappearance of the anticorruagated region above around 1 V. Note that although the d_{xz} -type PDOS is comparable in size with the $d_{3z^2-r^2}$ -type PDOS in this energy range, the weighted contribution of d_{xz} orbitals is much smaller due to the orbital shapes and the tip-sample geometry. For the P tip magnetization, below the Fermi level the orbital-shape-weighted contribution of $d_{3z^2-r^2}$ is dominating compared to d_{xz} , d_{yz} ; for the PDOS see Fig. 3.2.2(c) (\uparrow). Above the Fermi level the importance of the d states decreases rapidly, and concomitantly $m = 0$ s and p_z states gain more importance, resulting in normal corrugation in the full energy and tip-sample distance range.

Comparing Fig. 3.2.4(a-c) we find that the anticorruagation regime is shifted to larger tip-sample distances following the order s , p_z , and $d_{3z^2-r^2}$, similarly as found for the W(110) surface. This is due to the increasingly localized character of these tip orbitals in the z -direction. It means that the dominating current contributions originate from less and less surface atoms that are located directly below the tip position. Considering the orbital-dependent transmission and these z -localized ($m = 0$) tip orbitals, it follows naturally that the maximal effect of the surface d_{xz} , d_{yz} orbitals preferring anticorruagation is found at larger tip-sample

distances. On the other hand, there are certain energy regimes where this orbital overlap effect results in the occurrence of normal corrugation since the complex competition between d_{xz} , d_{yz} and $d_{3z^2-r^2}$ surface orbitals weighted with their partial PDOS is won by the corrugating $d_{3z^2-r^2}$ state. For all considered ideal magnetic tips the P tip magnetization corresponding to the majority spin channel does not show any contrast inversion in the studied (z, V) range. Taking the PERP and AP tip magnetization directions we expect normal corrugation above approximately 1.0 V (s -tip), 0.9 V (p_z -tip), and 0.8 V ($d_{3z^2-r^2}$ -tip) irrespective of the tip-sample distance. The reasons are outlined above, and see the discussion for the s -tip. The series of Fig. 3.2.4(a–c) demonstrate the orbital-dependent tunneling and tip orbital effects on the corrugation inversion.

Taking the iron tip having all nine orbital characters with weighted energy-dependent PDOS, it is clearly seen in Fig. 3.2.4(d) that the $\Delta I(z, V) = 0$ contours are considerably affected by the tip electronic structure. We find that all considered tip magnetization directions result in the appearance of corrugation inversions in the studied bias voltage and tip-sample distance range. Close to the surface anticorrugation is observed for the same reason as discussed for the s -tip, with the exception of the approximate $[-1.7 \text{ V}, -1.4 \text{ V}]$ range where the AP tip magnetization shows normal corrugation and no inversion at all. The reasons for this finding are the observed $d_{3z^2-r^2}$ peaks in the surface majority spin (\uparrow) PDOS at around 1 eV and 1.5 eV below the sample Fermi energy and the tip minority spin (\downarrow) PDOS at around 1.5 eV above the tip Fermi level, see Fig. 3.2.2(c) and (d). Such a combination of electronic structures gives a robust normal corrugation in the given bias range. By moving the tip away from the surface, contrast inversions are indicated by the $\Delta I = 0$ contours at large tip-sample distances, *i.e.*, the anticorrugation ($\Delta I < 0$) changes to normal corrugation ($\Delta I > 0$). It is clearly seen that these inversion contours vary considerably depending on the tip magnetization orientation. This is due to the complex combined effect of the orbital-dependent tunneling and spin-polarization originating from the electronic structures of the sample surface and the tip. For instance, the minority spin (\downarrow) d_{xy} PDOS peak of the tip located at 0.5 eV below its Fermi level in Fig. 3.2.2(d) is mainly responsible for the set of observed inversions at around 0.5 V bias. The d_{xy} tip orbital prefers normal corrugation in the studied tip-sample distance range due to its xz and yz nodal planes since above the H position the anticorrugating d_{xz} , d_{yz} surface orbitals do not contribute to the current, and I_T is expected to

be larger than I_H . Considering other orbital contributions weighted with their partial PDOS, however, results in anticorruagation below about $z = 6 \text{ \AA}$. In effect, we point out that the complex interplay of the real-space orbital shapes and the energy-dependent PDOS of the contributing spin channels of both the surface and the tip results in the observed corrugation inversion maps in Fig. 3.2.4. The above findings demonstrate the tunability of the height of the observable atomic contrast inversion depending on the spin-polarized tunneling via the tip magnetization orientation.

3.2.4 Simulated SP-STM images

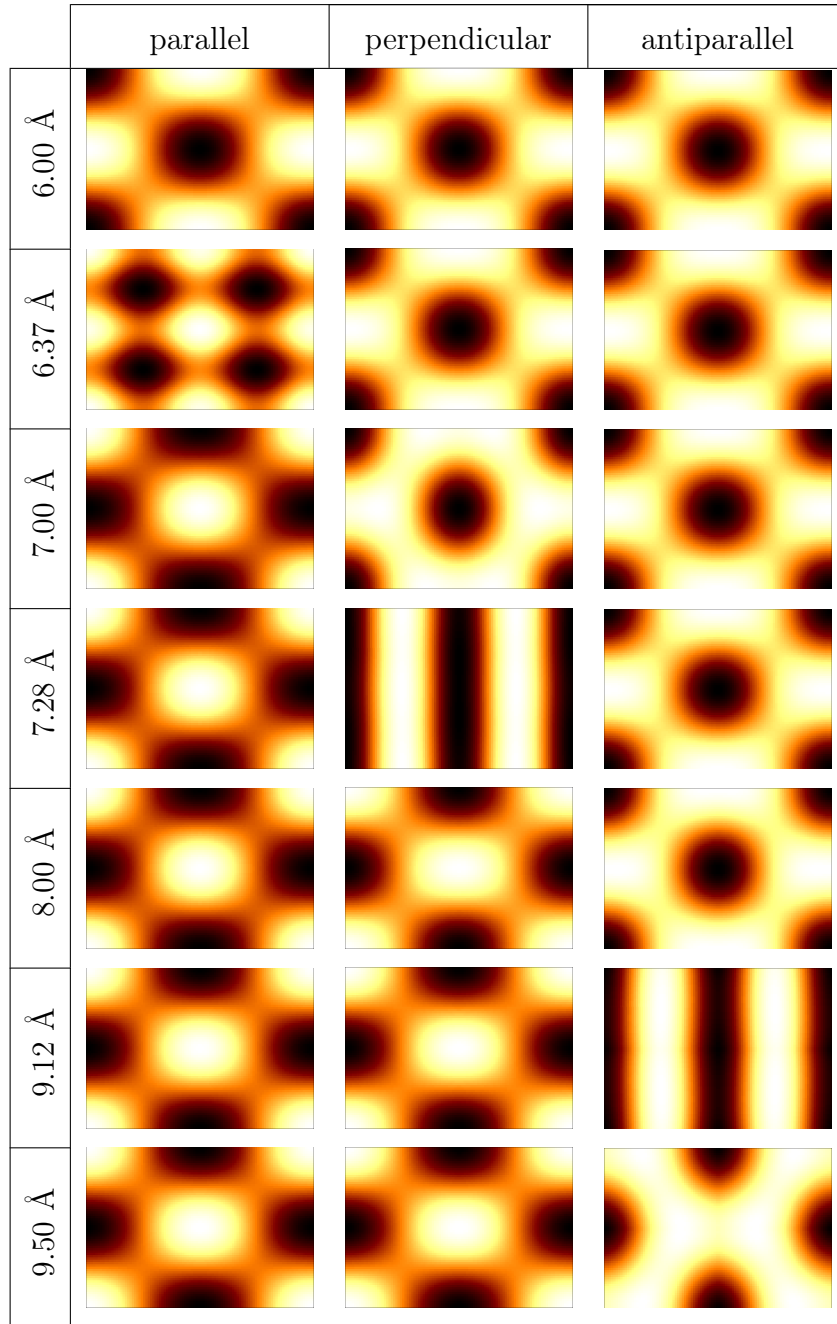


Figure 3.2.5: Simulated constant-current SP-STM images of the $Fe(110)$ surface at $V = 0.5$ V bias voltage and three magnetic orientations of the iron tip: parallel, perpendicular, and antiparallel to the $Fe(110)$ surface magnetic moment. The apparent heights of the Fe atom denoted by crosses in Fig. 3.2.4(d) are the same in each row. The SP-STM scan area corresponds to the rectangle shown in Fig. 3.2.1. Light and dark areas denote larger and smaller apparent heights, respectively. Adapted from Ref. [P3]

In order to show the dependence of the atomic contrast inversion on the tip-sample distance and on the tip magnetization orientation more apparently, constant-current SP-STM images are simulated. We choose the iron tip and the bias voltage of $V = 0.5$ V. The total tunneling current is calculated in sheets of 0.01 Å vertical width centered at seven selected tip heights between 6 and 9.5 Å marked by crosses in Fig. 3.2.4(d) above the rectangular scan area shown in Fig. 3.2.1. The lateral resolution is 0.04 Å by taking 100×70 points in each sheet. The constant-current contours are extracted following the method described in Ref. [29]. Fig. 3.2.5 shows the simulated constant-current SP-STM images of the Fe(110) surface at seven apparent heights of the surface Fe atom (seven rows) and three magnetic orientations of the iron tip (three columns): parallel (P, first column), perpendicular (PERP, second column), and antiparallel (AP, third column) to the Fe(110) surface magnetic moment. It can clearly be seen that the contrast inversion occurs at different tip heights depending on the tip magnetization orientation: P – 6.37 Å, PERP – 7.28 Å, AP – 9.12 Å, see also Fig. 3.2.4(d). We find that the SP-STM image of the contrast inversion with P tip magnetization orientation is markedly different from the striped images in the PERP and AP case. Note, that such striped STM images of the contrast inversion were found above the nonmagnetic W(110) surface as well. Below the inversion we observe anticorrugation, *i.e.*, the surface atoms appear as depressions, and above the inversion normal corrugation is obtained, in accordance with Fig. 3.2.4(d).

3.3 HOPG

Recent interest in different carbon allotropes (fullerenes, nanotubes, graphene, graphite) and nanostructures [58] and their potential for a wide spectrum of technological applications [59, 60, 61], for example biological and chemical sensors [62, 63], nano- and molecular electronics [64, 65], photovoltaics [66] and catalysis [67, 68], make atomically resolved investigation of carbon substrates – such as highly oriented pyrolytic graphite (HOPG) – of great relevance across many different scientific fields.

HOPG(0001) is one of the most frequently probed surface, where the tip orbital symmetries play a crucial role. The tip-dependent corrugation was discussed by Tersoff and Lang and the role of the orbital composition of the tip atom was highlighted [69]. The two nonequivalent carbon atomic sites of HOPG (α and β) are responsible for different patterns in STM images. Depending on the applied bias voltage and tunneling current both triangular and hexagonal honeycomb patterns can be observed. The selective imaging of the α and β atoms results in a triangular pattern [70, 71], which is mostly observed under typical tunneling conditions, although a honeycomb pattern can be recorded as well [72, 73]. Chaika *et al.* showed that using a [001]-oriented tungsten tip allows for the control of the tip orbitals responsible for the imaging, hence different patterns in the STM image can be obtained [74, 75]. Ondráček *et al.* showed that multiple scattering effects can also play an important role in the near contact regime and they can result in a triangular pattern in the STM image with hollow sites appearing as bright spots, instead of the carbon atoms [76]. Teobaldi *et al.* rationalized the bias dependent STM contrast mechanisms observed on the HOPG(0001) surface by modelling a set of tungsten tips taking the effects of tip electronic structure, termination, composition and sharpness into account [51].

Note that in Hungary experimental scanning probe methods (mostly STM) have been applied with great success to study intriguing phenomena at the surfaces of carbon-based materials in the group of László Péter Biró [64, 77, 78, 79, 80, 81, 82].

It is clear that the tip geometry and electronic structure cannot be neglected in an accurate STM simulation method. If the symmetry of the tip orbitals has a considerable effect on the STM image, it follows naturally that so does the tip orientation. All simulation methods require a well-defined tip geometry and ori-

entation. Usually a simple geometry is chosen, *e.g.* a pyramid-shaped tip apex, but the local tip geometry at the apex and the relative orientation of the sample surface and the tip apex are unknown and hardly controllable in experiments. Moreover, these tip apex characteristics can even change during the experimental STM scan, see *e.g.* [55, 83] for magnetic surfaces. In separate electronic structure calculations of the sample surface and the tip their local coordinate systems are usually set up in such a way that they represent the corresponding crystallographic symmetries. The electronic structure data, either the single electron wave-functions or the density of states (DOS), are defined in the given local coordinate systems and they are used in the STM simulations. Thus, the relative orientation of the tip and the sample is fixed and it usually corresponds to a very symmetrical setup, which is unlikely in experiments. Hagelaar et al studied a wide range of tip geometries and spatial orientations in the imaging of the NO adsorption on Rh(111) in combination with STM experiments [35] and their analysis is quite unique among the published STM simulations.

In this section we mainly focus on the contrast changes and stability of the HOPG surface. By calculating relative brightness maps we compare our 3D-WKB method to the Bardeen method and experimental data as well. We will show that the observed “stripe” formation is a combined effect of the electronic structure and the tip orbital symmetries, and demonstrate that the triangular-hexagonal contrast change can be achieved by - apart from bias voltage change - tip rotations alone.

3.3.1 Computational details

The HOPG(0001) surface and a set of tungsten tips were modelled in [51]. Employing the bSKAN code [38, 39] it was pointed out in [51] that the tunneling current depends on the relative orientation of the tip and the surface and two orthogonal orientations were considered for three tip models with different sharpnesses and compositions: blunt tungsten tip - $(r)W_{\text{blunt}}$, sharp tungsten tip - $(r)W_{\text{sharp}}$ and carbon-contaminated tungsten tip - $(r)W_{\text{C-apex}}$, with ‘r’ marking the tips rotated by 90 degrees around the z axis normal to the surface plane. Slab geometry relaxations were performed and the PDOS of the tip apex and sample surface atoms were calculated within the generalized gradient approximation Perdew-Burke-Ernzerhof (GGA-PBE) [84] projector augmented wave (PAW)

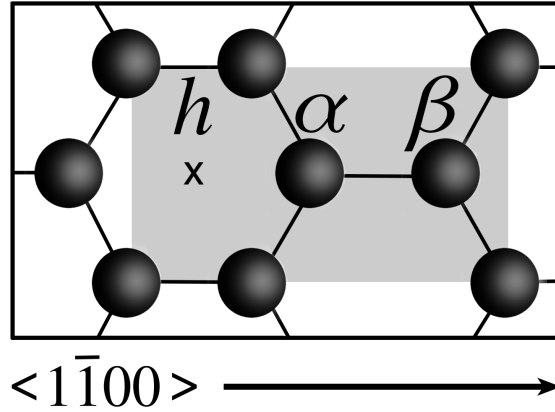


Figure 3.3.1: The shaded rectangle shows the considered scanning area of the HOPG surface for STM simulations. The positions of the characteristic h , α and β sites of the HOPG(0001) surface are explicitly shown. Adapted from Ref. [P4]

scheme implemented in the plane-wave VASP code [42, 85, 86]. Details on the geometries of the HOPG surface and the W tips as well as on the performed electronic structure calculations are found in Fig. 3.3.1 and section II B of [51]. For the 3D-WKB STM simulations we chose $\phi_S = \phi_T = 4.8$ eV electron work function for both the HOPG surface [87] and the tungsten tips. The tunneling current was calculated in a box above the rectangular scan area of the HOPG(0001) surface shown as the shaded area in Fig. 3.3.1 containing 31×21 lateral grid points in accordance with the STM calculations of [51] using the Bardeen approach. This corresponds to 0.142 \AA and 0.123 \AA resolution in the x and y direction, respectively and in the surface-normal z direction we used a finer, 0.02 \AA resolution. The constant-current contours are extracted following the method described in [29] and we report STM images above the mentioned rectangular scan area. Similarly to the W(110) and Fe(110) surfaces we performed convergence tests to determine the suitable number of atoms to include in the superposition. Based on the results we considered carbon atoms which are at most $d_{\parallel} = 7.5 \text{ \AA}$ far from the edge of the scan area, thus involving altogether 117 surface atoms in the atomic superposition.

In the 3D-WKB model an arbitrary tip rotation can be performed by setting the corresponding Euler angles $(\vartheta_0, \varphi_0, \psi_0)$, see also Fig. 2.2.2. Due to our choice of the fixed sample and tip geometries the rotated (rW) tips of [51] correspond to $(0^\circ, 0^\circ, 0^\circ)$ and the unrotated (W) tips to $(0^\circ, 0^\circ, 90^\circ)$ Euler angles. Note that when changing the Euler angles, tunneling through one tip apex atom was considered

only and contributions from other tip atoms were not taken into account. High degrees of tilting the tip ($\vartheta_0 > 30^\circ$) could, in fact, result in multiple tip apices [88] depending on the local geometry, which can increase the tunneling current, but can also lead to the destruction of the atomic resolution in STM images.

3.3.2 Relative brightness maps

As in the previous sections – to demonstrate the reliability of the 3D-WKB approach – first we perform a systematic comparison of bias-dependent normalized constant-current topographs (relative brightnesses) calculated above the HOPG surface with those obtained by Bardeen’s tunneling approach. We discuss the differences and their origins. Comparing the simulated relative brightnesses with experimental data [51] we find that the two tunneling methods perform at the same quantitative reliability. Turning to STM images, we show that the local tip orientation has a considerable effect on the obtained constant-current contrast.

For the analysis of the topographic contrast we calculate brightness profiles along the $\langle 1\bar{1}00 \rangle$ direction of the HOPG(0001) surface, following the methods described in [51]. These brightness profiles are line sections of the constant-current contour at a given bias voltage, which contain the three characteristic positions of the HOPG surface: hollow (h), carbon- α and carbon- β , see Fig. 3.3.1. In order to compare the brightness profiles of different tip geometries and bias voltages, the profiles are scaled to the $[0,1]$ interval. The definition of the relative brightness of a given point (\mathbf{x}) along the scan line is the following:

$$B(\mathbf{x}, V) = \frac{z(\mathbf{x}, V) - z(\mathbf{x}_{\min}, V)}{z(\mathbf{x}_{\max}, V) - z(\mathbf{x}_{\min}, V)}, \quad (3.3.1)$$

where $z(\mathbf{x}, V)$ is the height of the constant-current contour above the \mathbf{x} point at bias voltage V , $z(\mathbf{x}_{\min}, V)$ and $z(\mathbf{x}_{\max}, V)$ respectively have the smallest and largest apparent heights along the scan line, thus $B(\mathbf{x}_{\min}, V) = 0$ and $B(\mathbf{x}_{\max}, V) = 1$. The current values were chosen for each bias voltage in the interval of $[-1V, 1V]$ in steps of 0.1 V in such a way that the lowest apparent height of each constant-current contour was 5.5 Å.

Using the same lateral resolution of the scanning area employing two different methods M and N , it is possible to quantitatively compare the relative brightness

profiles B_M and B_N by calculating the correlation coefficient as

$$r_{M,N}(V) = \frac{\sum_{i=1}^n [B_M(x_i, V) - \bar{B}_M(V)] [B_N(x_i, V) - \bar{B}_N(V)]}{\sqrt{\sum_{i=1}^n [B_M(x_i, V) - \bar{B}_M(V)]^2} \times \sqrt{\sum_{i=1}^n [B_N(x_i, V) - \bar{B}_N(V)]^2}}. \quad (3.3.2)$$

Here, $\bar{B}_M(V) = \frac{1}{n} \sum_{i=1}^n B_M(x_i, V)$ is the mean value of the brightness profile obtained by method M at bias voltage V and $B_M(x_i, V)$ denotes the relative brightness of the i th point of the B_M profile, which consists of n points. $M, N \in \{3D - WKB, \text{Bardeen, Experiment}\}$ methods were compared, the data for the last two were taken from [51].

3.3.3 Comparison between 3D-WKB and Bardeen methods

Using the correlation coefficient defined in Eq. (3.3.2), we compare the relative brightness profiles obtained by the 3D-WKB and Bardeen methods. Figure 3.3.2 shows bias-dependent relative brightnesses above the $h - \alpha - \beta - h$ line along the $\langle 1\bar{1}00 \rangle$ direction of the HOPG(0001) surface in the bias voltage range of $[-1V, 1V]$ in steps of 0.1 V for each considered W and rW tip models using the 3D-WKB method. The corresponding relative brightness profiles obtained by the Bardeen method can be found in Fig. 9 of [51].

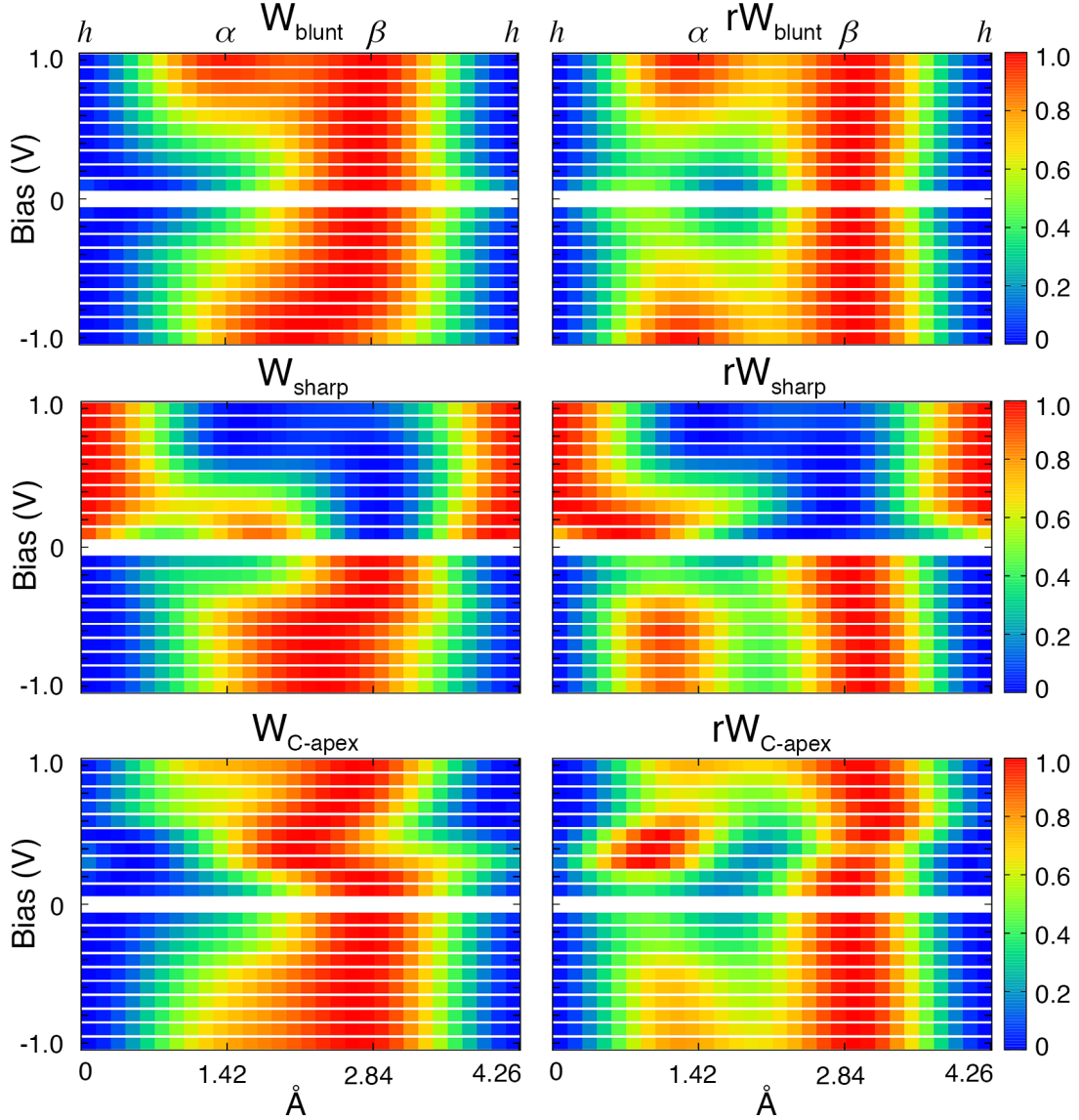


Figure 3.3.2: Relative brightness profiles $B(\mathbf{x}, V)$ in Eq. (3.3.1) along the $\langle h\bar{1}100 \rangle$ direction ($h-\alpha-\beta-h$ line) of the HOPG(0001) surface calculated by the 3D-WKB method in the $[-1V, 1V]$ range for different tip models: W_{blunt} , rW_{blunt} , W_{sharp} , rW_{sharp} , $W_{\text{C-apex}}$, and $rW_{\text{C-apex}}$, see text for details. Adapted from Ref. [P4]

We also calculate correlations considering the negative ($-1V \leq V < 0V$), positive ($0V < V \leq 1V$) and full ($-1V \leq V \leq 1V$) bias ranges. In these cases the $B_{3D-WKB}(x_k, V)$ and $B_{\text{Bardeen}}(x_k, V)$ brightness data consist of ten (negative or positive bias) or twenty (full bias range) times the number of points ($n = 31$) of a single bias brightness profile. The results are listed in table 3.3.1.

Considering the obtained correlations, we find an excellent agreement between the 3D-WKB and the Bardeen brightness results in the case of the W_{blunt} and

3D-WKB vs. Bardeen	W_{blunt}	rW_{blunt}	W_{sharp}	rW_{sharp}	$W_{\text{C-apex}}$	$rW_{\text{C-apex}}$
Negative bias	97.1	98.3	96.1	92.4	62.0	3.4
Positive bias	98.3	96.5	-27.1	8.9	-4.9	27.3
Full bias range	97.5	97.3	36.6	48.8	29.2	16.0

Table 3.3.1: Percentual relative brightness correlations according to equation (3.3.2) between the 3D-WKB and Bardeen methods for different tip models in the negative ($-1 \text{ V} \leq V < 0 \text{ V}$), positive ($0 \text{ V} < V \leq 1 \text{ V}$) and full ($-1 \text{ V} \leq V \leq 1 \text{ V}$) bias ranges. Adapted from Ref. [P4]

rW_{blunt} tips. All of the single bias profiles show at least 90% correlation and in the full bias range the correlation is more than 97% for both orientations. For the W_{sharp} and rW_{sharp} tips a good agreement between the two models is found at negative bias voltages only, where the brightness profiles are qualitatively similar to the ones obtained by the blunt tip models. In the positive bias range the 3D-WKB model shows that the h position has the largest apparent height at almost each considered bias voltage and in effect, the STM contrast is reversed at positive compared to negative bias voltages. We return to this asymmetry later on. For the $W_{\text{C-apex}}$ and $rW_{\text{C-apex}}$ tips the agreement is the poorest between the two tunneling models.

These results can be rationalized on the basis of the different contributions of the orbital-decomposed tip electronic states to the tunneling current and can be explained by the atomic geometry of the STM tip models in view of the different concepts of the tunneling models. The Bardeen method uses the Kohn–Sham single electron states in the vacuum to construct the transmission matrix elements, *i.e.* outside the localization radii of the PAW projectors. On the other hand, in the 3D-WKB model it is assumed that electrons tunnel through one tip apex atom and the PDOS of this apex atom is used for describing the tip electronic structure which is constructed based on the PAW projectors. The exponential decay of the electron states into the vacuum is taken into account by the transmission coefficient in equation 2.2.5. The PDOS of the tip apex atom is sensitive to the chemical environment, *i.e.* to the quality and geometrical arrangement of the surrounding atoms. In case of the $(r)W_{\text{blunt}}$ tips the PDOS of the tip apex atom represents well the electronic structure of the whole tip and there is practi-

cally no significant difference in the description of the tunneling process between the two methods. For the $(r)W_{\text{sharp}}$ and $(r)W_{\text{C-apex}}$ tips a pyramidal atomic arrangement was considered and the transmission functions differ considerably in the two methods. For example, in case of the $(r)W_{\text{C-apex}}$ tips the W atoms from the pyramid itself are expected to contribute much more to the tunneling due to their relatively large d -DOS compared to the C-apex p -DOS, see Fig. 6 of [51]. These electron states are considered in the Bardeen but not in the 3D-WKB model.

To understand the practically reversed brightness profiles at positive with respect to negative bias voltages for the $(r)W_{\text{sharp}}$ tips a deeper analysis is needed. As a first indication, it was found that the local density of states (LDOS) 3 Å above the tip apex is much more asymmetric in the bias voltage for the W_{sharp} than for the W_{blunt} tip, see Fig. 6(d) of [51]. The 3D-WKB method allows for the decomposition of the tunneling current according to the orbital symmetries σ (sample) and τ (tip): $I_{\sigma\tau}$. The electronic structure calculation of the HOPG sample showed that the p_z -like PDOS is at least an order of magnitude larger than the s -, p_x - and p_y - like PDOS for both α - and β -type carbon atoms in the range of ± 1 eV around the Fermi energy. This means that the HOPG electronic structure can safely be approximated by taking the p_z -like PDOS only and we fixed the orbital index of the sample as $\sigma = p_z$. On the other hand, the W-apex has $\tau \in \{s, p_y, p_z, p_x, d_{xy}, d_{yz}, d_{3z^2-r^2}, d_{xz}, d_{x^2-y^2}\}$ and the C-apex has $\tau \in \{s, p_y, p_z, p_x\}$ orbital symmetries in the considered tip models.

Using Eq. (3.1.3) we calculate the relative contribution of all $\sigma \leftrightarrow \tau$ transitions to the tunneling current, $\tilde{I}_{\sigma\tau}$, 5.5 Å above the β carbon atom at ± 1 V bias voltages. The current histograms shown in Fig. 3.3.3 give the percentual contributions of the different tip orbitals to the current for the three tip models. First, let us focus on the bias-asymmetry of the contributions of the W_{sharp} tip. For this case the s , d_{yz} , $d_{3z^2-r^2}$ and d_{xz} tip states are dominant and the largest contribution comes from the $d_{3z^2-r^2}$ state. As can clearly be seen, the main difference in the positive and negative bias ranges shows up in the increasing d_{yz} and d_{xz} contributions with a concomitant decreasing of the $d_{3z^2-r^2}$ contribution at positive bias. Since $m \neq 0$ tip states are responsible for a contrast inversion on metal surfaces [28, P1], these current histograms explain the observed contrast inversion with respect to the bias polarity above the β carbon atom of the HOPG surface found in Fig. 3.3.2. Based on the current histograms, we also expect that

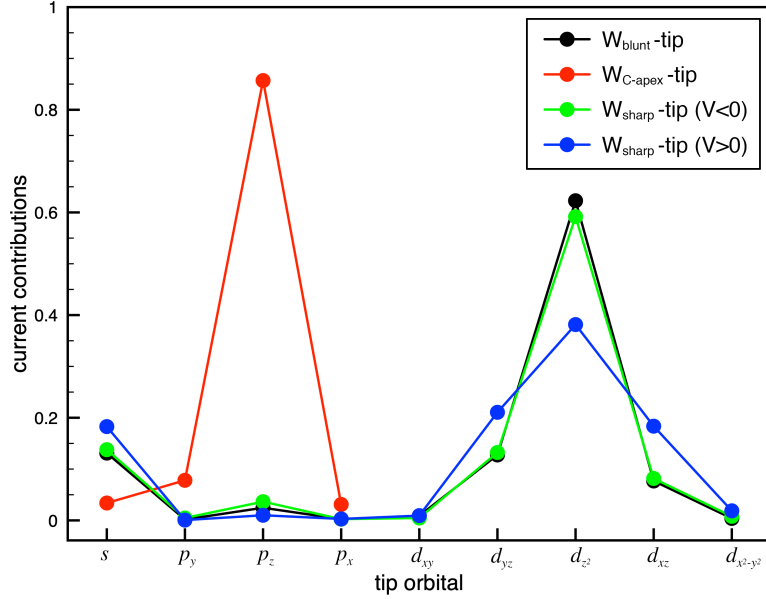


Figure 3.3.3: Orbital-dependent relative current contributions $\tilde{I}_{\sigma\tau}$ defined in Eq. (3.1.3) for $\sigma = p_z$, 5.5 Å above the β atom of the HOPG(0001) surface at ± 1 V bias voltages using three different tip models. The tip orbitals (τ) are explicitly shown. For brevity, we used the notation of d_{z^2} for the $d_{3z^2-r^2}$ orbital. Adapted from Ref. [P4]

the W_{sharp} and W_{blunt} tips provide similar contrast at negative bias voltages. This is confirmed by Fig. 3.3.2. Note that changing the bias voltage in the respective negative ($-1 \text{ V} \leq V < 0 \text{ V}$), positive ($0 \text{ V} < V \leq 1 \text{ V}$) ranges does not influence the quality of the current histograms. For the W_{blunt} and $W_{\text{C-apex}}$ tips no qualitative difference of the current histograms were found at positive bias voltages, therefore, the $V < 0 \text{ V}$ results are shown only. Moreover, it is seen in Fig. 3.3.3 that the largest contribution is due to the $p_z - p_z$ transition for the $W_{\text{C-apex}}$ tip: it gives 85% of the total current.

These features of the current histograms can be understood from the energy dependence of the PDOS of the tip apices and also from the angular dependence of the electron states. In Fig. 6 of [51] one can see that for the W_{blunt} and $W_{\text{C-apex}}$ tips the PDOS functions are fairly symmetric with respect to the Fermi energy, thus the bias voltage does not affect the current contributions significantly. Although some of the orbitals have rather asymmetric PDOS, these give small contributions to the tunneling current due to their angular dependence, thus they do not affect the histograms, *e.g.* the p_x state of the $W_{\text{C-apex}}$ tip, or the $d_{x^2-y^2}$ state of the W_{blunt} tip. On the other hand, the PDOS functions of the W_{sharp} tip apex are rather asymmetric, particularly for the $d_{3z^2-r^2}$ state, which has the

largest contribution. For $E > E_F^T$, which is relevant at negative bias, it is larger than for $E < E_F^T$, thus the current contribution of this particular $d_{3z^2-r^2}$ state is also larger for negative bias, as seen in Fig. 3.3.3. All in all, this asymmetric behaviour of the PDOS of the W_{sharp} tip apex is responsible for the observed contrast inversion with respect to the bias polarity in Fig. 3.3.2.

3.3.4 Comparison between simulations and experiment

In experimental STM images of HOPG, it is possible to identify the $\langle 1\bar{1}00 \rangle$ direction (assuming that the brightest features lie along this direction), however, the order of h , α and β sites is unknown, see figures 3 and 4 of [51]. The only possible way to determine the $h - \alpha - \beta$ or $h - \beta - \alpha$ order along the $\langle 1\bar{1}00 \rangle$ direction is the direct comparison of experimental and simulated brightness profiles. Since the experimental profiles are obtained by averaging numerous sections of the scan lines (for more information, see [51]), the comparison at different bias voltages can be performed if the profiles are transformed to start with their corresponding maximum or minimum. While in [51] the relative brightness profiles are shifted to start with their maximum, we transform them to start with their global minimum. The motivation for changing the reference point is the following: the experimental brightness profiles at each bias voltage have one minimum only, while at certain voltages they have two local maxima very close in magnitude to each other: $B(x_{max_1}, V) \approx B(x_{max_2}, V)$, similarly to the simulated brightness profiles using the rW_{blunt} tip at larger bias voltages, see Fig. 3.3.2. If the profiles are shifted to start with the global maximum then the correlation coefficient strongly depends on the actual position (x_{max_1} or x_{max_2}) of the global maximum. For example, when comparing two almost identical brightnesses with two local maxima at α and β sites, if the global maximum in one profile is α and is β in the other, then the correlation coefficient of the two profiles shifted to the corresponding global maximum can be negative, instead of the value of close to 1. Rigidly shifting the brightness profiles to start with their global minimum value solves this problem.

Following this convention, Fig. 3.3.4 shows a comparison between the experimental [51], Bardeen-calculated and 3D-WKB modeled brightness profiles. In the simulations the rW_{blunt} tip was used. We obtain good qualitative agreement on the bias-dependence of the triangular-hexagonal contrast transition between

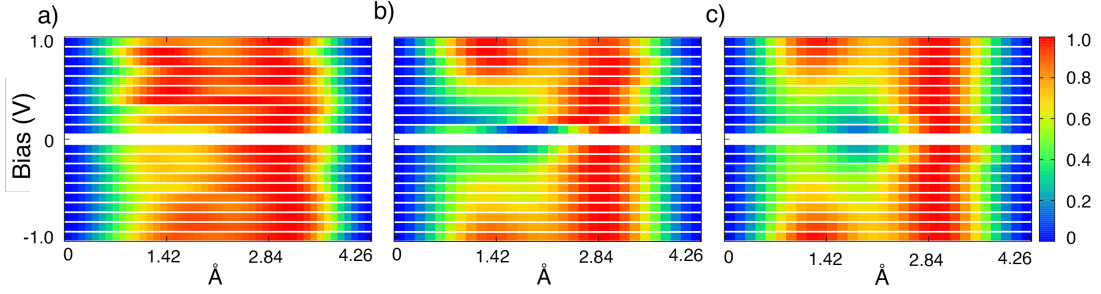


Figure 3.3.4: Experimental and simulated relative brightness profiles ($B(\mathbf{x}, V)$) along the $\langle 1\bar{1}00 \rangle$ direction ($h - \alpha - \beta - h$ line) of the HOPG(0001) surface: (a) experiment [51], (b) Bardeen [51], (c) 3D-WKB. All profiles are rigidly shifted to start with their global minimum value. In the simulations the rW_{blunt} tip was used. Adapted from Ref. [P4]

the experiments and simulations. To quantify the agreement the correlation coefficients between the experimental and simulated brightness profiles are reported in Table 3.3.2 using all of the previously introduced tip models.

Bardeen vs. Exp.	W_{blunt}	rW_{blunt}	W_{sharp}	rW_{sharp}	$W_{C-\text{apex}}$	$rW_{C-\text{apex}}$
Negative bias	91.3	92.6	89.8	84.6	93.5	91.9
Positive bias	90.6	88.2	67.2	69.8	87.8	78.8
Full bias range	90.9	90.2	77.6	75.0	90.5	85.1

3D-WKB vs. Exp.	W_{blunt}	rW_{blunt}	W_{sharp}	rW_{sharp}	$W_{C-\text{apex}}$	$rW_{C-\text{apex}}$
Negative bias	90.7	92.5	89.9	85.3	93.6	91.9
Positive bias	89.9	87.9	66.1	68.1	87.4	78.5
Full bias range	90.3	90.0	77.0	74.3	90.3	84.9

Table 3.3.2: Percentual relative brightness correlations according to Eq. (3.3.2) between the simulated results (Bardeen, 3D-WKB) using different tip models and the experimental data (see Fig. 3.3.4(a) and [51]) in the negative ($-1 \text{ V} \leq V < 0 \text{ V}$), positive ($0 \text{ V} < V \leq 1 \text{ V}$) and full ($-1 \text{ V} \leq V \leq 1 \text{ V}$) bias ranges. Adapted from Ref. [P4]

The two tunneling methods produce almost the same correlation coefficients when comparing the simulated brightness profiles with the experimental results, the difference between them is always less than 2%. This finding is independent of the applied tip model or bias polarity. Based on the correlation values, we

also find that brightness profiles of the $(r)W_{\text{blunt}}$ and $(r)W_{\text{C-apex}}$ tips are very similar to the experimental ones, while the $(r)W_{\text{sharp}}$ tip models perform better at negative compared to positive bias polarity.

3.3.5 Simulated STM images

To investigate the STM contrast changes depending on the bias voltage and on the tip orientation, constant-current STM images are simulated. The calculated images shown in Figures 3.3.5–3.3.7 are taken in the rectangular scan area shown in Fig. 3.3.1 and all contours have the same minimum apparent height of 5.5 Å. We use the convention for the definition of the two different contrast patterns as in [51]: A triangular pattern has two brightness maxima in the scan area and beside these a hexagonal pattern has two secondary maxima with relative brightness larger than 0.7.

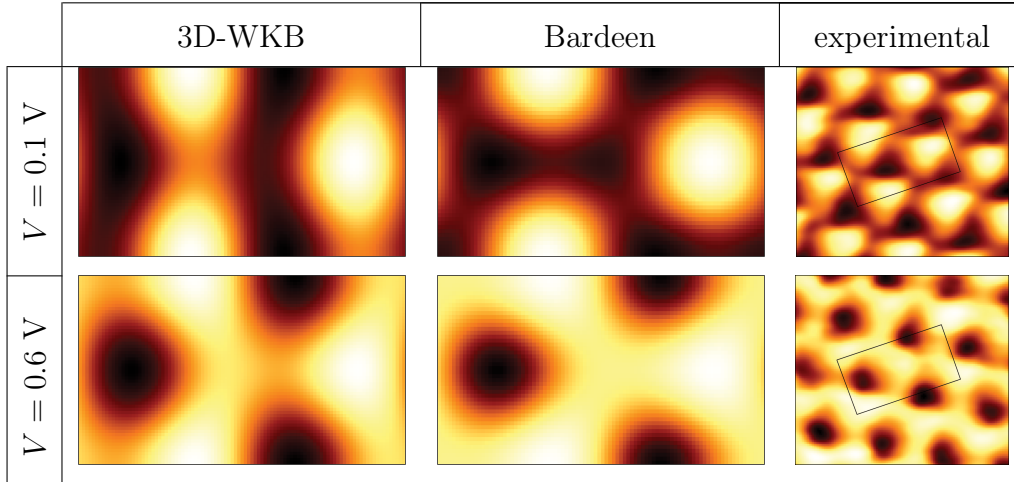


Figure 3.3.5: Bias voltage effect on the simulated STM image contrast of HOPG at a fixed ($\vartheta_0 = 0^\circ$, $\varphi_0 = 0^\circ$, $\psi_0 = 0^\circ$) tip orientation using the blunt W tip at 0.1 V, and 0.6 V bias voltages using 3D-WKB and Bardeen methods. For comparison, experimental STM images [51] are also shown, with the rectangular scan area for the simulations (see also Fig. 3.3.1). The qualities of the STM image contrasts correspond to the results of Fig. 3.3.4. Adapted from Ref. [P4]

In Fig. 3.3.5 we demonstrate the bias-dependent contrast change at two characteristic bias voltages for both 3D-WKB and Bardeen methods employing a rW_{blunt} tip and compare the simulation results to experiments [51]. From the brightness profiles of Fig. 3.3.4 we expect a triangular pattern of bright spots for 0.1 V bias voltage as these profiles have one global maximum. On the other hand,

a hexagonal honeycomb pattern is expected for 0.6 V bias as the corresponding profiles have two local maxima. These expectations are in accordance with the simulated constant-current STM images of Fig. 3.3.5 and we obtain a qualitatively good agreement for the primary contrast in comparison with experiments shown in Fig. 3.3.5. Thus, the results confirm that the bias voltage has a major influence on the apparent height of the atoms in the STM images of HOPG [51].

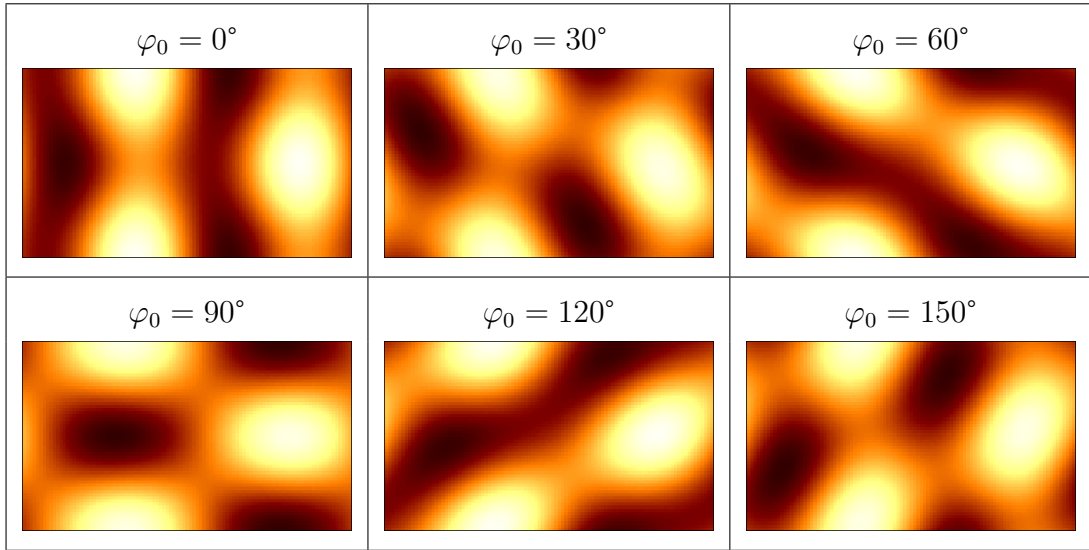


Figure 3.3.6: Tip rotation effect on the simulated STM images of HOPG at $V = 0.1$ V using the blunt W tip. $\vartheta_0 = \psi_0$ are fixed at 0° in each part. The rectangular scan area is shown in Fig. 3.3.1. Adapted from Ref. [P4]

To investigate the effect of the tip orientation on the STM contrast, we simulate constant-current STM images of the HOPG surface at 0.1 V bias voltage using the W_{blunt} tip with different local orientations of the apex. First, tip rotations around the $z = z'$ -axis are considered, *i.e.* we fix the Euler angles $\vartheta_0 = \psi_0 = 0^\circ$ and change φ_0 from 0° to 150° in 30° steps. This way, no orientational change of the dominating $d_{3z^2-r^2}$ tip-apex orbital state is present. The obtained constant-current STM images are shown in Fig. 3.3.6. We find that the primary features of the images do not change with such kind of tip rotations: the maxima of the contours are always located at the same carbon- β positions, thus the images preserve the symmetry of the HOPG surface and the tip is stable using the experimentalist terminology. At the selected bias voltage and tip-sample distance we observe a triangular pattern with the apparent height of the β atoms significantly larger

than that of the α atoms. The effect of the tip rotation shows up as a secondary feature in the STM images. There are certain lateral directions where the apparent heights are larger and elongated, thus we can identify ‘stripes’ in the images. The direction of these ‘stripes’ is independent of the underlying atomic structure of the HOPG surface, thus it is clearly the rotational effect of the blunt W(110) tip having C_{2v} symmetry. Note that similar elongated features are also reported in figure 15(b) of [89] for the HOPG surface using a blunt W(110) cluster model for the STM tip. Similar ‘stripes’ can also be observed in experimental STM images, see *e.g.* figure 3 of [51]. It was even found that the ‘stripes’ can change their lateral orientation depending on the bias voltage (compare figures 3(f) and (i) of [51]). According to our interpretation, this suggests two differently rotated local tip apex geometries at the two bias voltages. We note that in-plane low-barrier sub-apex atomic rearrangements, while maintaining the tip-apex, can lead to an effective rotation of the tip-apex structure (see for instance the models in figures 1(b) and (d) in [51]), causing the simulated and measured changes in the STM ‘stripes’.

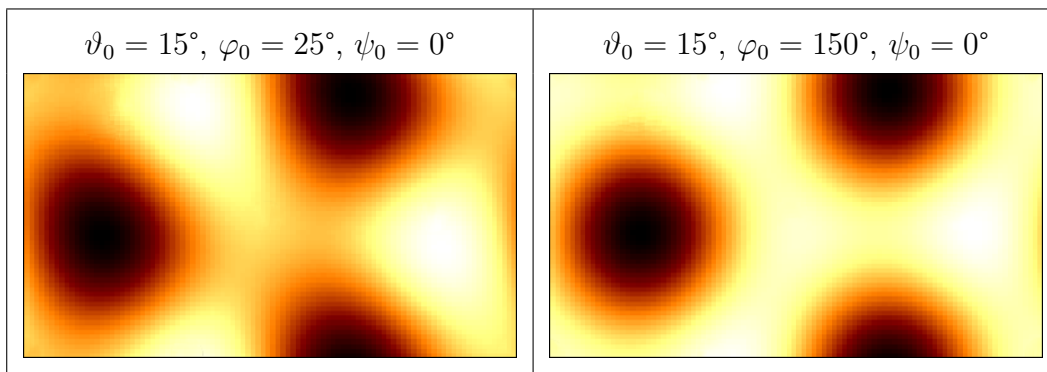


Figure 3.3.7: Tip rotation effect on the simulated STM image contrast of HOPG at $V = 0.7$ V using the blunt W tip. Parts correspond to $(\vartheta_0 = 15^\circ, \varphi_0 = 25^\circ, \psi_0 = 0^\circ)$ and $(\vartheta_0 = 15^\circ, \varphi_0 = 150^\circ, \psi_0 = 0^\circ)$ tip orientations, respectively. The rectangular scan area is shown in Fig. 3.3.1. A triangular-hexagonal contrast change is observed due to the tip rotation. Adapted from Ref. [P4]

On the other hand, it is interesting to find that the primary features of the STM image can change by the same kind of local tip rotation around the z' -axis by φ_0 . The requirement for this is a non-zero ϑ_0 , *i.e.* a tilted $d_{3z^2-r^2}$ tip-apex orbital with respect to the surface normal of the substrate. Figure 3.3.7 demonstrates that the STM image contrast can change between the triangular

and hexagonal patterns above the HOPG surface solely due to the change of the tip orientation by fixing all other tunneling parameters. For this case we selected 0.7 V bias voltage and two orientations of the W_{blunt} tip: ($\vartheta_0 = 15^\circ$, $\varphi_0 = 25^\circ$, $\psi_0 = 0^\circ$) and ($\vartheta_0 = 15^\circ$, $\varphi_0 = 150^\circ$, $\psi_0 = 0^\circ$). Note that the modelled contrast change is obtained at a 125° difference in φ_0 and is expected to be due to enhanced contributions from $m \neq 0$ tip-apex electronic states to the tunneling current upon tip-rotation, as we have seen in Sec. 3.2. As a further consequence, our simulations indicate that tip instabilities in STM experiments are likely found for local tip-apex geometries described by non-zero ϑ_0 angles that also result in distorted STM images.

Note that tip-surface interactions can further complicate the STM contrast. In [76] it was shown that multiple scattering effects can induce a contrast change shifting the maximum brightness from β carbon to the hollow position above the HOPG surface in the near contact regime (below 4 Å of tip-sample separation). Since our minimum tip-sample distance is always 5.5 Å, *i.e.* we are in the pure tunneling regime, we expect that the tip-surface force is monotonically decreasing with decreasing current by moving the tip away from the surface. Thus force related changes in the contrast do not modify our conclusions on the effect of the tip orientations observed in STM images in pure tunneling regimes for tip-surface distances larger than 4 Å. However, close to the contact substantial effects of the tip-surface force on the STM contrast can be expected upon tip rotation, which could be interesting to study in the future using an appropriate method.

3.4 What is the orientation of the tip?

The atomic structure and electronic properties of the tip apex can strongly affect the contrast of STM images. This is a critical issue given the – to date unsolved –, experimental limitations in the precise control of the tip apex atomic structure. Definition of statistically robust procedures to indirectly obtain information on the tip apex structure is highly desirable as it would open up for more rigorous interpretation and comparison of STM images from different experiments. To this end, here we introduce a statistical correlation analysis method to obtain information on the local geometry and orientation of the tip used in STM experiments based on large scale simulations. The key quantity is the relative brightness correlation of constant-current topographs between experimental and simulated data.

This correlation can be analyzed statistically for a large number of modeled tip orientations and geometries. Assuming a stable tip during the STM scans and based on the correlation distribution, it is possible to determine the tip orientations that are most likely present in an STM experiment, and exclude other orientations. This is especially important for substrates such as HOPG since its STM contrast is strongly tip dependent, which makes the interpretation and comparison of STM images very challenging.

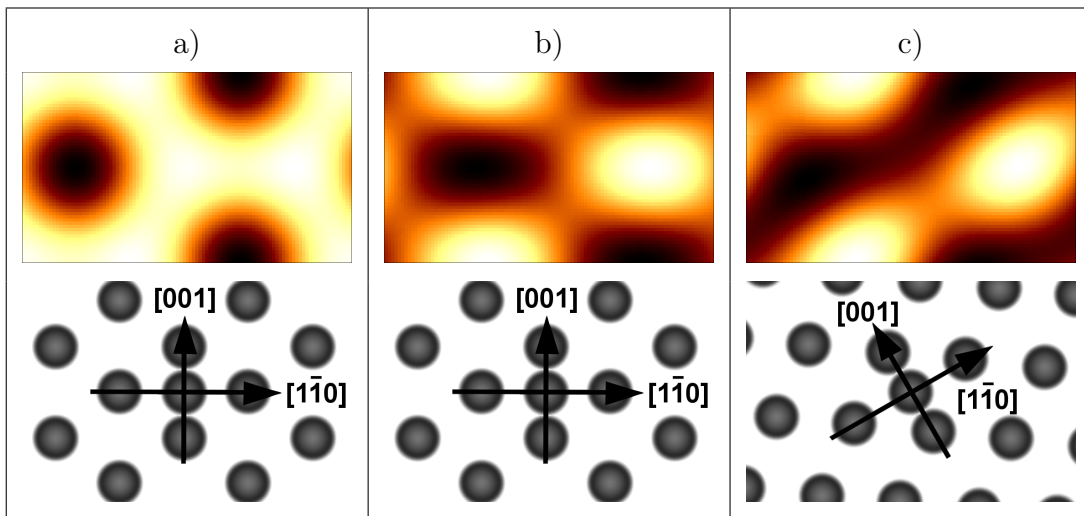


Figure 3.4.1: Constant-current STM images illustrating the variety of observed STM contrasts above the HOPG(0001) surface in the tunneling regime for $\vartheta_0 = \varphi_0 = 0$: (a) hexagonal contrast (both α - and β -carbons are bright; $V = 1$ V, $\psi_0 = 90^\circ$), (b) triangular contrast (only β -carbons are bright; $V = 0.1$ V, $\psi_0 = 90^\circ$), (c) triangular contrast with striped feature ($V = 0.1$ V, $\psi_0 = 120^\circ$). The STM images are calculated above the shaded rectangular area shown in Fig. 3.3.1 using the W_{blunt} tip model. The relative orientation of the W_{blunt} tip with respect to the HOPG(0001) surface is shown in each subfigure. Adapted from Ref. [P5]

A characteristic set of the possible STM contrasts in the tunneling regime is shown in Fig. 3.4.1. Here, the two nonequivalent carbon atoms of HOPG (α and β) are primarily responsible for the different STM contrasts [hexagonal contrast in Fig. 3.4.1(a) and triangular contrast in Fig. 3.4.1(b)]. Particular rotations of the STM tip were shown to result in striped STM images, affecting the secondary contrast features [Fig. 3.4.1(c)]. In the near contact regime multiple scattering effects and tip-sample forces also play an important role in the STM contrast appearance [18], *e.g.* a shift of the maximum brightness from the β -carbon to the hollow (h) position of HOPG was demonstrated by Ondráček *et al.* [76]. Note that we restrict our study to the pure tunneling regime corresponding to the used

experimental data [51] and to the validity of the 3D-WKB method. The diversity of the observed STM contrasts above the HOPG(0001) surface surely contains information about the local geometry of the tip apex in STM measurements, therefore HOPG(0001) is an ideal candidate to illustrate the applicability of our statistical correlation analysis method combining large scale STM simulations with experiments.

3.4.1 Method

To quantitatively compare the experimental ($M = EXP$) and simulated ($M = SIM$) constant-current topographs, we use the previously defined relative brightness (see equation (3.3.1)). Assuming that all contours of method M consist of $N_x \times N_y$ points ($x \in \{x_{ij}\}$, $i = 1 \dots N_x$, $j = 1 \dots N_y$), the mean value of the relative brightness in a given bias voltage range of N_V bias values ($k = 1 \dots N_V$) can be calculated as

$$\bar{B}_M = \frac{1}{N_x N_y N_V} \sum_{i=1}^{N_x} \sum_{j=1}^{N_y} \sum_{k=1}^{N_V} B_M(x_{ij}, V_k). \quad (3.4.1)$$

Using the same resolution of the scanning area in the experiment and in the simulations resulting in relative brightness contours of $N_x \times N_y$ lateral points in both cases, it is possible to quantitatively compare the B_{EXP} and B_{SIM} contours in the corresponding bias voltage range of N_V bias values by calculating their correlation coefficient as

$$r = \frac{\sum_{i,j,k} [B_{EXP}(x_{ij}, V_k) - \bar{B}_{EXP}] [B_{SIM}(x_{ij}, V_k) - \bar{B}_{SIM}]}{\sqrt{\sum_{i,j,k} [B_{EXP}(x_{ij}, V_k) - \bar{B}_{EXP}]^2} \times \sqrt{\sum_{i,j,k} [B_{SIM}(x_{ij}, V_k) - \bar{B}_{SIM}]^2}}. \quad (3.4.2)$$

Another statistical measure for the difference between experimental and simulated contours is the mean squared error,

$$MSE = \frac{1}{N_x N_y N_V} \sum_{i=1}^{N_x} \sum_{j=1}^{N_y} \sum_{k=1}^{N_V} [B_{EXP}(x_{ij}, V_k) - B_{SIM}(x_{ij}, V_k)]^2. \quad (3.4.3)$$

A perfect agreement of contours is obtained at $\text{MSE} = 0$, and it is desired that MSE is minimal comparing experimental and simulated contours for obtaining the best agreement. For selected contours and bias voltages we found good correspondence between minimal MSE and maximal correlation. However, MSE is not bounded from above, and this makes the analysis of MSE distribution and the interpretation of maximal MSE difficult. Therefore, we excluded using this measure in our statistical analysis. The calculation of the correlation coefficient in Eq. (3.4.2) was presented in the more general case of taking 2D relative brightness contours. However, the same method can be specifically applied to one-dimensional (1D) relative brightness profiles by setting $N_y = 1$. This approach will be used in the following for the $\langle 1\bar{1}00 \rangle$ direction of the HOPG(0001) surface since experimental data is available for such a case [51], similarly as in sections 3.3.3 and 3.3.4. To calculate the relative brightness correlations between the experiment and simulations, profiles shifted to start with their minimum value, $B(x_{i=1}, j=1, V_k) = 0$ are taken, as we have discussed in the section 3.3.4.

Since in the simulations the tip material, atomic arrangement/geometry, and orientation described by the Euler angles $(\vartheta_0, \varphi_0, \psi_0)$ can be chosen in practically infinite ways, the corresponding relative brightness profiles are dependent on these parameters, as well as the correlation coefficient r . Based on the results of HOPG imaging (see Sec. 3.3) we only consider W_{blunt} and W_{sharp} tip models, since carbon-contaminated tips with a C atom at the apex can be excluded due to a dramatic decrease of the tunneling current.

Constant-current brightness profiles are calculated along the $\langle 1\bar{1}00 \rangle$ direction (x -axis of Fig. 3.3.1) containing the three characteristic positions of the HOPG(0001) surface: hollow (h), carbon- α and carbon- β sites. The experimental averaged brightness data with $N_y = 1$ and $N_x = 46$ points are taken from Fig. 4 of Ref. [51] in the interval of $[-1 \text{ V}, 1 \text{ V}]$ with 0.1 V steps. In the simulations the current values are chosen for each corresponding bias voltage in such a way that the lowest apparent height of each constant-current contour is $z_{\text{SIM}}(\mathbf{x}_{\text{min}}, V_k) = 5.5 \text{ \AA}$. The relative brightness profiles are calculated by using the introduced W_{blunt} and W_{sharp} tip models for a set of tip orientations described by the Euler angles: $\vartheta_0 = 0^\circ \dots 30^\circ$, $\varphi_0 = 0^\circ \dots 175^\circ$, $\psi_0 = 0^\circ \dots 355^\circ$ with 5° steps. The Euler angles are visualized in Fig. 2.2.2. ϑ_0 angle describes the rotation with respect to the x axis, transforming the z axis to z' . Additionally, φ_0 and ψ_0 are rotation angles around the z and z' axes, respectively, as Fig. 2.2.2 shows. The

exact meaning of the Euler angles is mathematically formulated in the rotation matrix in Eq. (2.2.7). Altogether $7 \times 36 \times 72 = 18144$ tip orientations are considered. For this selection we used the general symmetry property of the rotation matrix in Eq.(2.2.7): $(\vartheta_0, \varphi_0, \psi_0) = (-\vartheta_0, \varphi_0 + \pi, \psi_0 + \pi)$ and the mirror symmetry of the HOPG surface above the $h - \alpha - \beta$ line: $(\vartheta_0, \varphi_0, \psi_0) = (-\vartheta_0, -\varphi_0, -\psi_0)$. Correlation coefficients in Eq. (3.4.2) are calculated between the experimental and a large number of simulated relative brightness profiles in the negative ($-1 \text{ V} \leq V < 0 \text{ V}$), positive ($0 \text{ V} < V \leq 1 \text{ V}$) and full ($-1 \text{ V} \leq V \leq 1 \text{ V}$) bias ranges.

3.4.2 Correlation analysis

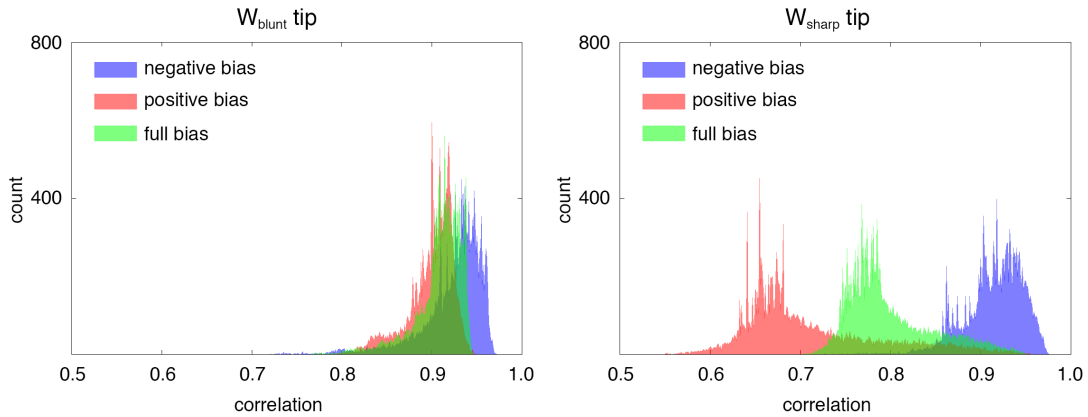


Figure 3.4.2: $|V| \leq 1 \text{ V}$ relative brightness correlation histograms calculated by using 18144 tip orientations for the W_{blunt} tip and W_{sharp} tip models. The correlation histograms for the negative, positive and full bias ranges are shown using Eq. (3.4.2) in the $r = [0.5, 1]$ range with 0.001 resolution. Adapted from Ref. [P5]

Fig. 3.4.2 shows the calculated relative brightness correlation histograms for the two considered tungsten tip models in 18144 tip orientations. The maximal correlation between the experiment and simulations is found at approximately 0.97 in the negative and at approximately 0.95 in the positive bias range for both tips. However, we cannot conclude that the tip orientations belonging to the maximal correlation are the best since there is a large number of other orientations within a few percent from the maximum correlation well above 0.9. Analyzing the correlation distribution, it is clearly seen that much more tip orientations provide better correlation values in the negative compared to the positive bias range for both tip models. This effect is even more evident for the W_{sharp} tip, where the correlation distributions have two distinct peaks for the negative and positive

bias at around 0.93 and 0.66, respectively. The presented statistics for the relative brightness correlation taking a large number of tip orientations confirm the significance of the findings of the previous section (Sec. 3.3), where the simulated brightness profiles obtained at positive bias for the W_{sharp} tip model in high symmetry orientations resulted in much lower correlation with the experiment than in the negative bias voltage range. No such large differences were found for the W_{blunt} tip at either bias polarities. This suggests that the W_{blunt} tip is more likely to be present in a wide range of bias voltages in the experiment than the W_{sharp} tip. The minimal correlation between the experimental and simulated brightness profiles is found at 0.55 for the W_{sharp} tip at positive bias voltages, whereas for the W_{sharp} tip at negative bias voltages and for the W_{blunt} tip at all considered bias voltage ranges the minimal correlation is above 0.7. Once more, this suggests a more likely W_{blunt} than W_{sharp} tip in the experiment since various local rotations of the W_{blunt} tip do not give worse correlations with the experiment than 0.7, whereas there are particular local rotations of the W_{sharp} tip at positive bias voltages with much worse correlations. The presented relative brightness correlation histograms provide information about the distribution of the correlation values in terms of the number of simulated tip orientations within a particular correlation range with the experimental brightness data. This presentation of the correlation statistics, however, cannot tell which specific tip orientations give the best or worst correlations with the experiment. To assign the most or least likely orientations of the STM tip in the experiment for the given tip model, we need another representation of the correlation data. Therefore, we complement our analysis by calculating *correlation maps*.

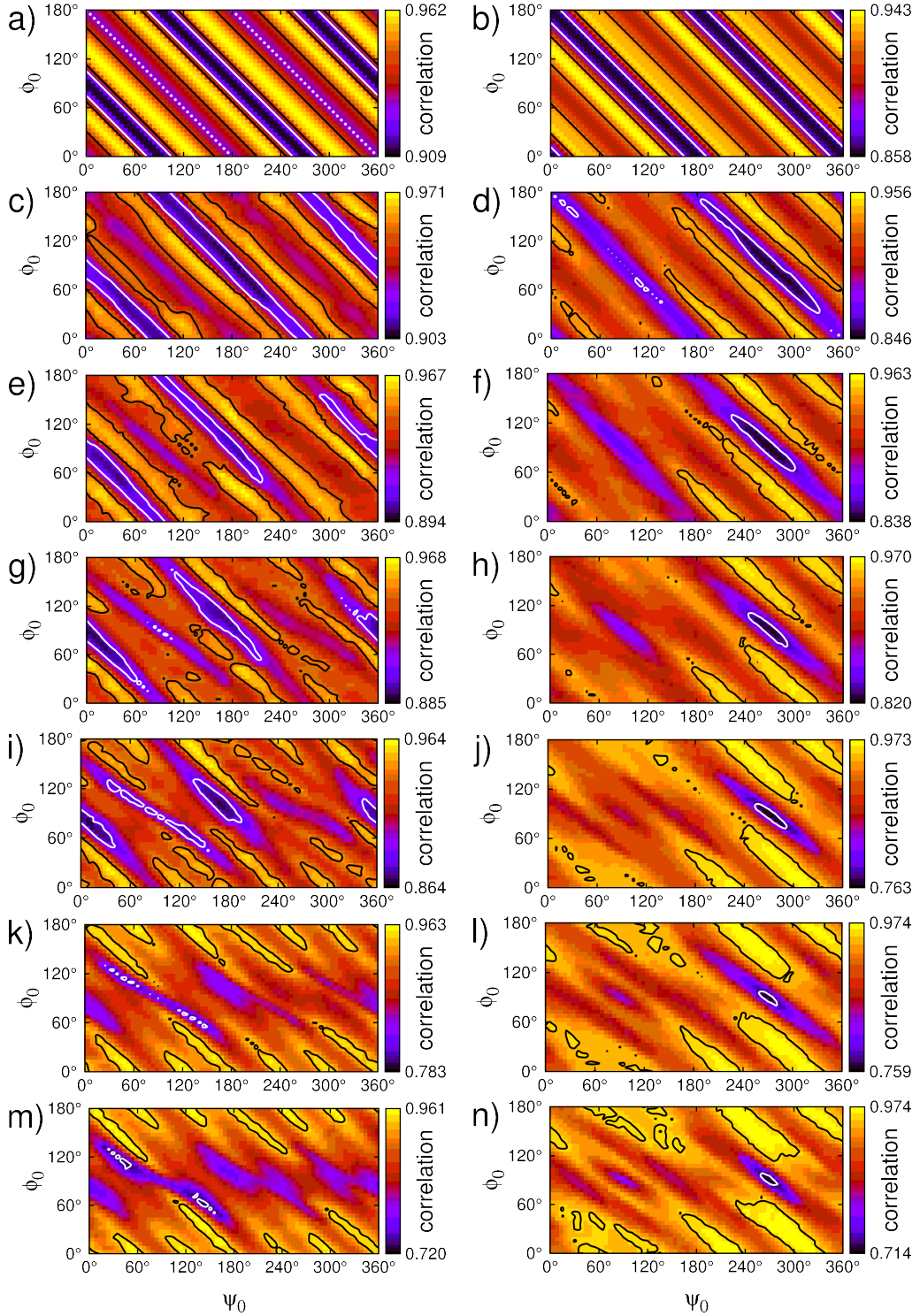


Figure 3.4.3: $-1 \text{ V} \leq V < 0 \text{ V}$ negative bias range correlation analysis. Relative brightness correlation distributions $r(\vartheta_0, \varphi_0, \psi_0)$ for W_{blunt} tip (first column) and W_{sharp} tip (second column) for the following fixed ϑ_0 angles: (a and b) 0° , (c and d) 5° , (e and f) 10° , (g and h) 15° , (i and j) 20° , (k and l) 25° , (m and n) 30° . Most (least) likely tip orientations in the experiment in the given bias interval correspond to bright (dark) regions bounded by black (white) contours within 2% relative to the maximum (minimum) correlation value in each subfigure. Adapted from Ref. [P5]

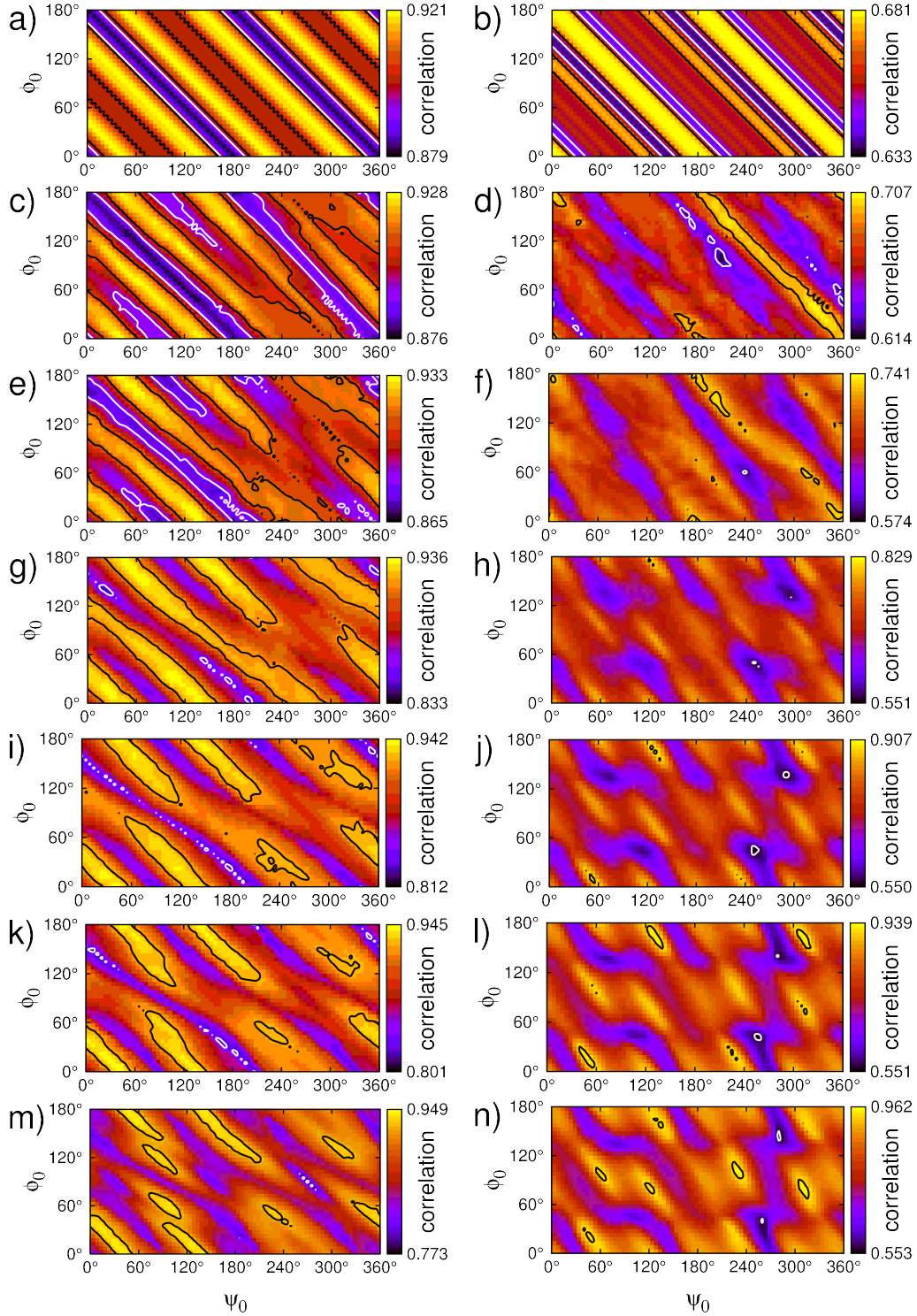


Figure 3.4.4: $0 \text{ V} < V \leq 1 \text{ V}$ positive bias range correlation analysis. Relative brightness correlation distributions $r(\vartheta_0, \varphi_0, \psi_0)$ for W_{blunt} tip (first column) and W_{sharp} tip (second column) for the following fixed ϑ_0 angles: (a and b) 0° , (c and d) 5° , (e and f) 10° , (g and h) 15° , (i and j) 20° , (k and l) 25° , (m and n) 30° . Most (least) likely tip orientations in the experiment in the given bias interval correspond to bright (dark) regions bounded by black (white) contours within 2% relative to the maximum (minimum) correlation value in each subfigure. Adapted from Ref. [P5]

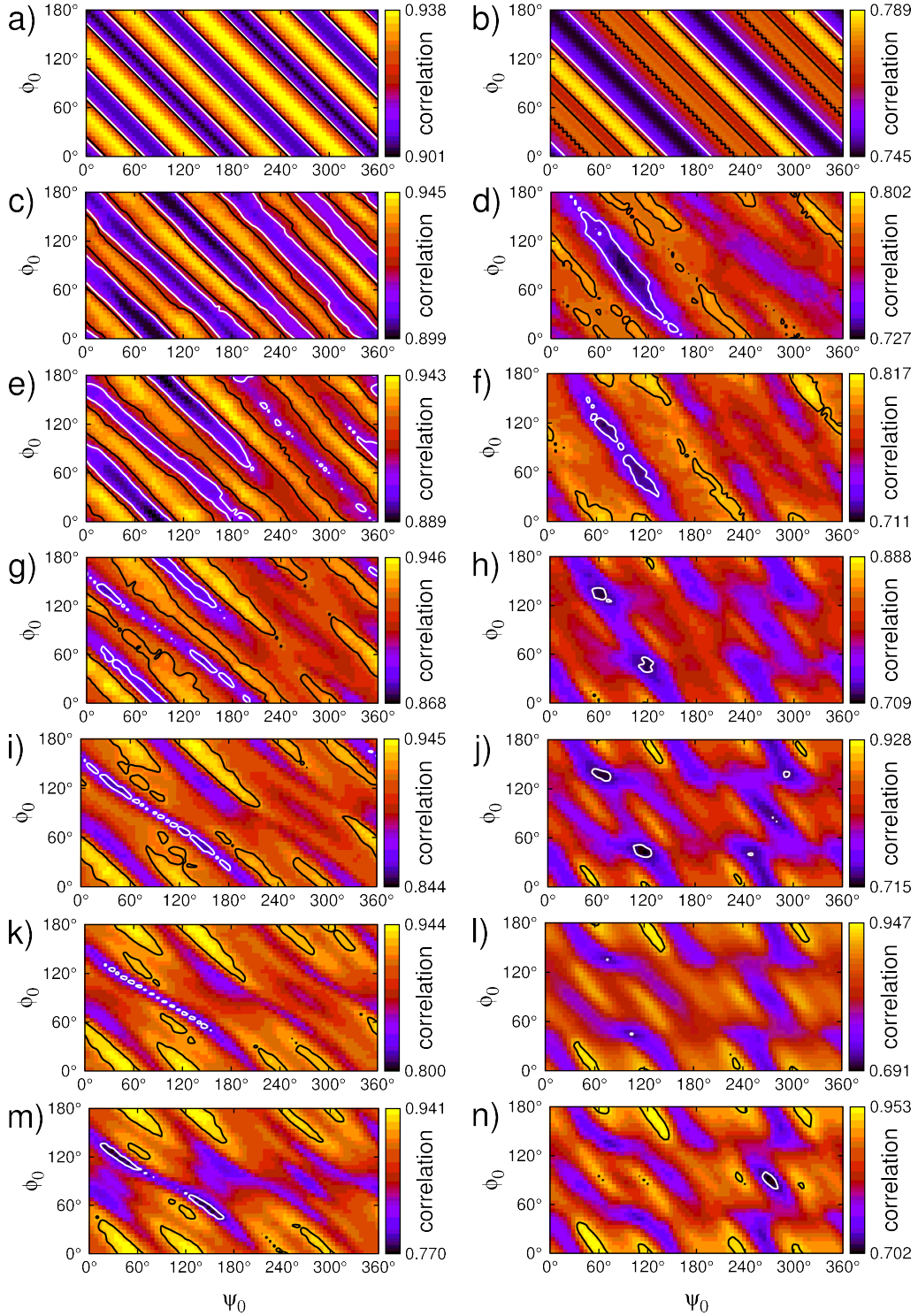


Figure 3.4.5: $-1 \text{ V} \leq V \leq 1 \text{ V}$ full bias range correlation analysis. Relative brightness correlation distributions $r(\vartheta_0, \varphi_0, \psi_0)$ for W_{blunt} tip (first column) and W_{sharp} tip (second column) for the following fixed ϑ_0 angles: (a and b) 0° , (c and d) 5° , (e and f) 10° , (g and h) 15° , (i and j) 20° , (k and l) 25° , (m and n) 30° . Most (least) likely tip orientations in the experiment in the given bias interval correspond to bright (dark) regions bounded by black (white) contours within 2% relative to the maximum (minimum) correlation value in each subfigure. Adapted from Ref. [P5]

Figs. 3.4.3–3.4.5 show the calculated relative brightness correlation maps for the two considered tungsten tip models in the negative, positive and full bias voltage range, respectively. $r(\varphi_0, \psi_0)$ two-dimensional maps are shown as a function of ϑ_0 . Note that $\vartheta_0 = 0$ corresponds to the same z -axis of the surface and the tip, and in this case φ_0 and ψ_0 denote the same type of rotations around the common z -axis. As a result, we obtain striped $r(\varphi_0, \psi_0)$ correlation maps for $\vartheta_0 = 0$ [panels (a) and (b)]. For $\vartheta_0 > 0$ these maps quickly change to show more complicated correlation distributions [panels (c–n)]. Most importantly, Figs. 3.4.3–3.4.5 show the most (least) likely tip orientations $(\vartheta_0, \varphi_0, \psi_0)$ in the experiment in the given bias interval corresponding to bright (dark) regions bounded by black (white) contours within 2% relative to the maximum (minimum) correlation value for each ϑ_0 assuming the model tip apex geometry. Overall, we find that the regions close to the maximal and minimal correlations can be differently affected by the bias range considered for the mapping for different tip apex geometries. These results emphasize the importance of a large experimental dataset for reliable application of the proposed procedure. Considering the favorable and unfavorable orientations for the given tip models, we find that the (φ_0, ψ_0) positions of the indicated regions close to the maximum and minimum correlations in the $r(\varphi_0, \psi_0)$ maps are fairly stable with respect to the change of ϑ_0 . This means that the specific (φ_0, ψ_0) Euler angles are representative for the likely (bright regions) and unlikely (dark regions) tip orientations in the STM experiment, irrespective of ϑ_0 . Based on our results, we find that the favored tip-sample relative orientations are far from being symmetric.

We introduce the area ratios as the number of tip orientations (area) within the denoted regions in Figs. 3.4.3–3.4.5 divided by the area of the $r(\varphi_0, \psi_0)$ maps (36×72). These area ratios at fixed ϑ_0 can be interpreted as the likelihood of favorable or unfavorable tip orientations in the experiment assuming the considered tip geometry in the given bias range. The area ratios alone, however, are not sufficient to identify the most or least likely tip orientations in the experiment since the maximum and minimum correlation values vary considerably depending on ϑ_0 .

To further analyze the correlation maps, the evolutions of the maximum and minimum correlation values and the calculated area ratios with ϑ_0 are reported in Fig. 3.4.6. This figure also allows for the comparison between the different bias voltage ranges and the two considered tip models. We find that the maximum correlation is increasing and the minimum correlation is decreasing with increas-

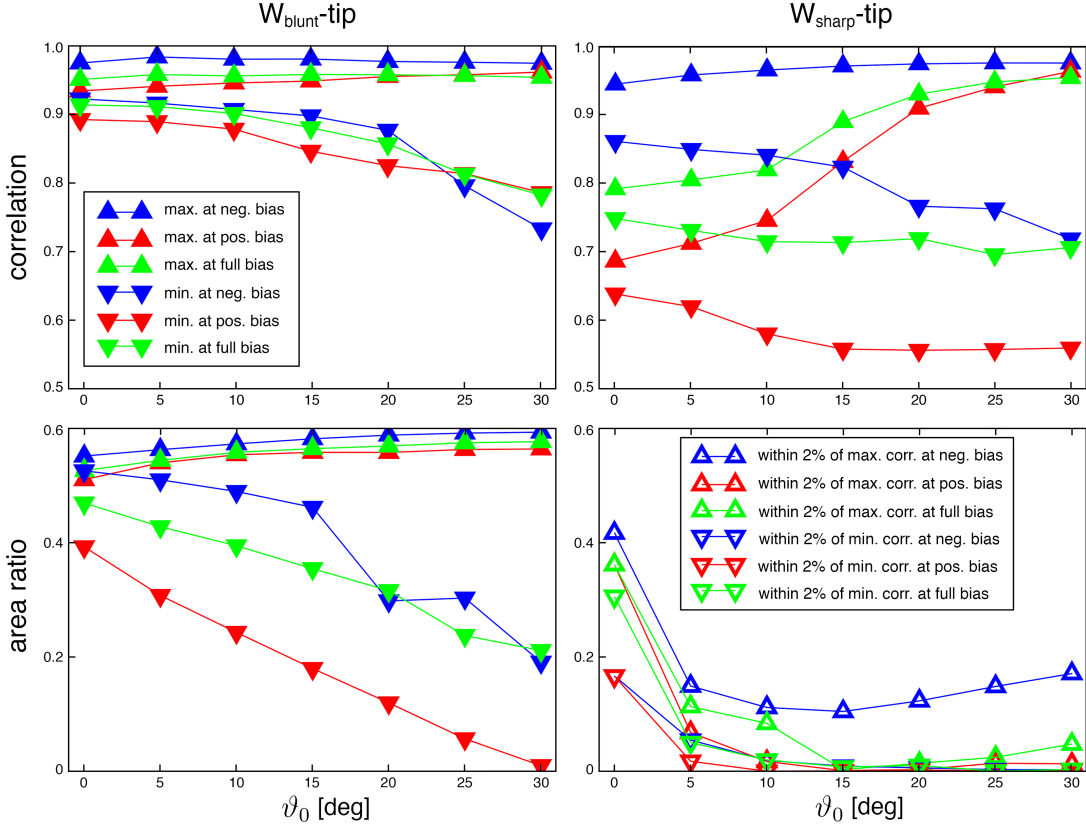


Figure 3.4.6: Analysis of the correlation maps in Fig. 3.4.3 (at negative bias), Fig. 3.4.4 (at positive bias) and Fig. 3.4.5 (at full bias) in the $|V| \leq 1$ V bias range. Top row: The evolution of the maximum and minimum correlation value in the $r(\vartheta_0, \varphi_0, \psi_0)$ maps with ϑ_0 . Bottom row: The ϑ_0 -evolution of the area within 2% relative to the maximum and minimum correlation values (respectively bounded by the black and white contours in Figs. 3.4.3–3.4.5) in relation to the area of the $r(\varphi_0, \psi_0)$ map (36×72). These area ratios at fixed ϑ_0 can be interpreted as the likelihood of favorable or unfavorable tip orientations in the experiment assuming the considered tip geometry. Left and right parts respectively correspond to data obtained by W_{blunt} and W_{sharp} tip models. Adapted from Ref. [P5]

ing ϑ_0 for all bias voltage ranges. This results in a larger difference between the maximum and minimum correlations with increasing ϑ_0 . It is interesting to note that the maximum correlation values are always larger than 0.9 for the W_{blunt} tip, whereas this is true only in the negative bias range for the W_{sharp} tip. In the positive and full bias ranges the maximum correlation above 0.9 is achieved for $\vartheta_0 \geq 20^\circ$, *i.e.*, for a much smaller number of considered tip orientations. On the other hand, the minimum correlation values are always smaller for the W_{sharp} compared to the W_{blunt} tip. These findings clearly suggest that the W_{blunt} tip is more likely to be present in the experiment in an enhanced bias voltage range than the W_{sharp} tip.

In Fig. 3.4.6, at negative bias voltages the two tips provide similar maximum correlation values as a function of ϑ_0 . In such case the area ratios can be used to decide which tip is more likely in the experiment since the corresponding area ratios are proportional to the number of tip orientations within the maximum correlation, and such larger area ratios favor a given tip. We find that the area ratios are generally larger for the W_{blunt} compared to the W_{sharp} tip. Area ratios close to the correlation maximum mean that more orientations can provide better correlation values for the W_{blunt} than for the W_{sharp} tip. On the other hand, area ratios close to the correlation minimum mean that more orientations provide correlations close to the minimum for the W_{blunt} compared to the W_{sharp} tip. This is, however, not a problem in the present case since the minimum correlations are always larger for the W_{blunt} compared to the W_{sharp} tip. Therefore, based on the number of favorable tip orientations, we can also conclude that the blunt tungsten tip is indeed more likely in the experiment than the sharp tip in the $|V| \leq 1$ V bias voltage range.

In order to check the robustness of our results we performed the correlation analysis with simulated brightness profiles obtained by taking the contributions of four extra next-neighbor atoms of the tip apex atom in the tunneling current calculations using the 3D-WKB method. We find that the correlation maps are quantitatively very similar to those obtained by the one-apex tip for $\vartheta_0 \leq 20^\circ$. For larger ϑ_0 —tilting the emergence of multiple tip apices distorts the simulated brightness profiles and consequently worsens the agreement with the experiment, manifesting as dramatically reduced correlation values (down to 0.35 at $\vartheta_0 = 25^\circ$ and 0.13 at $\vartheta_0 = 30^\circ$) for particular (φ_0, ψ_0) ranges. Based on this, we can conclude that our findings are robust for $\vartheta_0 \leq 20^\circ$, *i.e.* for a small tilting of the tip z -axis.

To investigate the effect of the bias voltage on the obtained results, we recalculated the correlation statistics in the $|V| \leq 0.3$ V bias voltage range that corresponds to the low bias regime used in typical STM imaging experiments of HOPG. This analysis used redefined negative ($-0.3 \text{ V} \leq V < 0 \text{ V}$; $N_V = 3$), positive ($0 \text{ V} < V \leq 0.3 \text{ V}$; $N_V = 3$) and full ($-0.3 \text{ V} \leq V \leq 0.3 \text{ V}$; $N_V = 6$) bias ranges. Fig. 3.4.7 shows the recalculated relative brightness correlation histograms for the two considered tungsten tip models in 18144 tip orientations. We find qualitatively similar results as in the $|V| \leq 1$ V bias range reported in Fig. 3.4.2. The main differences in Fig. 3.4.7 in comparison to Fig. 3.4.2 are: (i) there

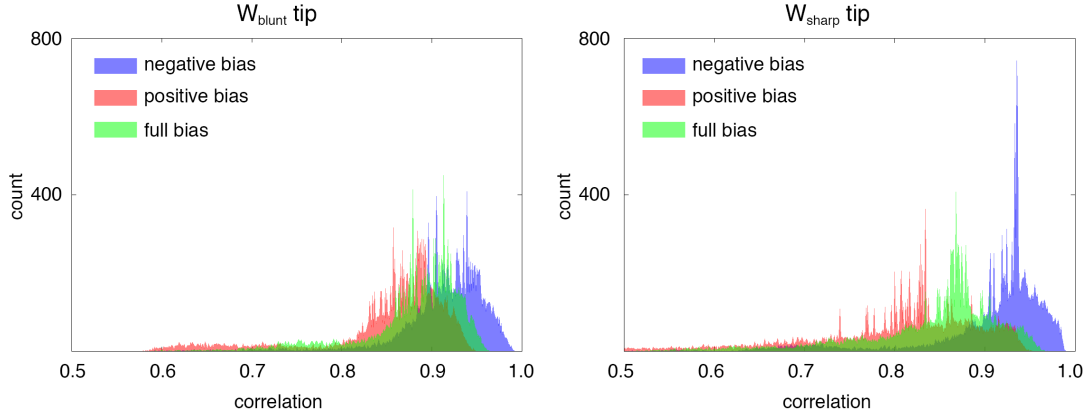


Figure 3.4.7: $|V| \leq 0.3$ V relative brightness correlation histograms calculated by using 18144 tip orientations for the W_{blunt} tip and W_{sharp} tip models. The correlation histograms for the negative, positive and full bias ranges are shown using Eq. (3.4.2) in the $r = [0.5, 1]$ range with 0.001 resolution. Adapted from Ref. [P5]

is a longer tail of the correlation distributions extending toward lower values for both tips, resulting in much lower minimum correlations (*e.g.*, 0.26 for the W_{sharp} tip at positive bias voltages and 0.58 for the W_{blunt} tip at all bias ranges), (ii) the maximum correlations are increased to 0.99 at negative bias for both tips, (iii) the difference between the two distinct peaks of the correlation distributions for the negative and positive bias in case of the W_{sharp} tip is reduced, but still significant (above 0.1).

Fig. 3.4.8 shows the evolutions of the maximum and minimum correlation values and the calculated area ratios with ϑ_0 obtained from the $r(\vartheta_0, \varphi_0, \psi_0)$ correlation maps in the $|V| \leq 0.3$ V bias voltage range. We find that the main discussed tendencies in Fig. 3.4.6 are not affected in the low bias regime. However, the area ratios within 2% of the maximum correlation are systematically larger for the W_{sharp} than for the W_{blunt} tip in the negative bias range. Since the maximum correlations are above 0.93 for for both type of tips in this bias interval, this suggests that more tip orientations of the W_{sharp} tip result in better agreement with the experiment than of the W_{blunt} tip at low negative bias, $-0.3\text{V} \leq V < 0\text{V}$. The indications of a favored W_{blunt} tip in the experiment are, however, not affected in the other considered low bias regimes.

Although using larger bias ranges is better for the statistical analysis, the tip may become unstable in the experiment at larger bias voltages, thus making the assignment of the tip geometry and orientation more difficult. In general, we suggest that the primary decision for the quality of the STM tip in an experiment

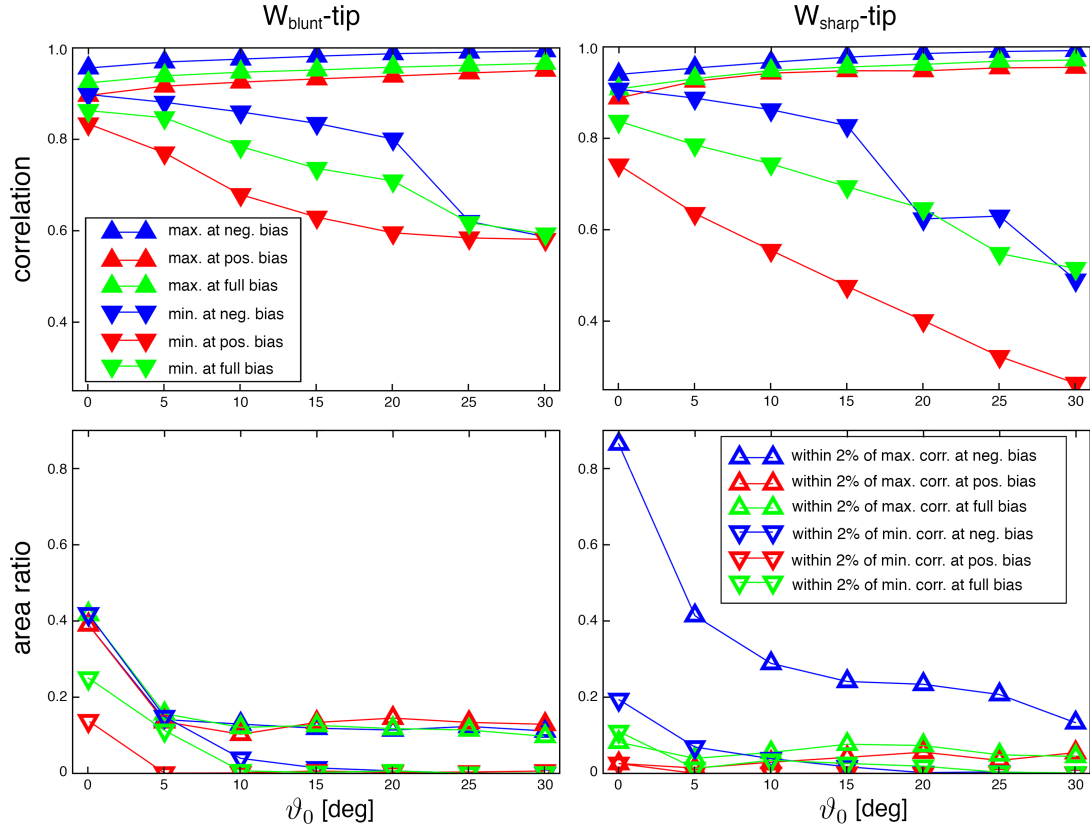


Figure 3.4.8: Extracted data from the correlation maps in the $|V| \leq 0.3$ V bias voltage range. Top row: The evolution of the maximum and minimum correlation value in the $r(\vartheta_0, \varphi_0, \psi_0)$ maps with ϑ_0 . Bottom row: the ϑ_0 -evolution of the area ratio, for explanation see the caption of Fig. 3.4.6. Left and right parts respectively correspond to data obtained by W_{blunt} and W_{sharp} tip models. Adapted from Ref. [P5]

has to be based on the comparison between the maximum and minimum relative brightness correlations between two (or more) tip models, and the secondary decisive factor should be the introduced area ratio measure that gives information on the number of likely or unlikely tip orientations.

Chapter 4

bSKAN-Chen results

In recent years there were several studies concerned with the role of the tip geometry, orbital character, and functionalization on the STM imaging. In the previous sections we investigated the effect of the bias voltage and tip electronic structure on the STM contrast formation of HOPG surface using tungsten tips with different terminations and sharpnesses following the work of Teobaldi *et al.* [51]. Chaika *et al.* demonstrated that by using oriented single-crystalline tungsten tips, it is possible to select a particular tip electron orbital for high-resolution imaging of HOPG [74, 75]. Channel-selective tunneling was also examined by Wong *et al.* using tip functionalization with hexa-peri-hexabenzocoronene (HBC) molecules [90]. Employing Chen’s derivative rule, Gross *et al.* simulated STM images of pentacene and naphthalocyanine molecules using CO-functionalized tips [36]. The increased lateral resolution achieved by these tips demonstrated the significant contribution of p -type tip states. Siegert *et al.* studied the influence of s - and p -wave tip symmetries on the STM maps of π -conjugated molecules using the reduced density matrix formalism combined with Chen’s derivative rule [37]. The effect of tip-orbital symmetries on the scanning tunneling spectra was also investigated by probing the cuprate high-temperature superconductor $\text{Bi}_2\text{Sr}_2\text{CaCu}_2\text{O}_{8+\delta}$. Suominen *et al.* found that the symmetry of the tip can radically change the topographic image due to the overlap of sample and tip orbitals [91], while da Silva Neto *et al.* stated that the apparent nematic behavior of the lattice is likely related to a realistic STM tip probing the band structure of the material [92]. They also pointed out the importance of tunneling interference effects in the STM junction.

The effect of inter- and intra-atomic interference of electron orbitals has also

been in the focus of several studies. Telychko *et al.* investigated the nitrogen-doped graphene surface with tungsten and diamond tips and found significantly smaller current (dip) above the nitrogen atom than above the neighboring carbon atoms at constant height [93]. This finding has been explained by a destructive quantum interference essentially resulting from the C – N π -bond. Using the Keldysh Green’s-function formalism, Jurczyszyn and Stankiewicz and Mingo *et al.* extensively investigated interorbital interference effects in various tip-sample combinations and found that the interference has a considerable influence on STM images and STS spectra [40, 41, 16]. Sachse *et al.* showed that an antiferromagnetic alignment of Mn spin moments in a Mn_2H complex on the Ag(111) surface explains the experimental STM observation of a dip above the middle of the Mn dimer [94]. In the following, we will point out that a destructive quantum interference between s and p_z tip orbitals contributes to the emergence of such a dip in the STM image.

In this chapter we demonstrate the reliability of the revised Chen’s derivative rule (see Sec. 2.2.2) for the mentioned N-doped graphene and antiferromagnetic Mn_2H complex on the Ag(111) surface, where quantum interference effects play an important role in the STM imaging process. This demonstration is done by qualitative and quantitative comparisons of simulated STM images with corresponding results obtained by Tersoff-Hamann and Bardeen tunneling methods. Quantitative comparison is facilitated by calculating Pearson product-moment correlation coefficients between the STM data sets as we have seen in Sec. 3.3. Importantly, we find that the revised Chen’s model is 25 times faster than the Bardeen method concerning computational time taking the same tunneling channels, while maintaining good agreement. The effects of electronic structure, orbital interference, and spatial orientation of the tip on the STM images are highlighted. Since the detailed analysis of quantum interference effects and arbitrary tip orientations in STM junctions is presently highly demanding and enormously time consuming using the Bardeen method, the implementation of the revised Chen’s derivative rule in the bSKAN code [38, 39] is a very promising tool for more efficient STM simulations, providing a deeper understanding of a wide variety of physical phenomena in STM junctions, *e.g.*, quantum interference and tip geometry effects.

4.1 Computational details

Using the revised Chen’s derivative rule implemented in the bSKAN code [39, 38], STM imaging of two functionalized surfaces of recent interest is investigated: N-doped graphene and an antiferromagnetic Mn_2H complex on the $\text{Ag}(111)$ surface in combination with several tip models. Geometrical relaxations and electronic structure calculations of the surface and tip models were performed separately using the VASP code [42], employing the projector augmented wave (PAW) method [48].

N-doped graphene is modeled as a free-standing single-layer graphene sheet in a 7×7 surface unit cell following Ref. [93] and 16 Å wide vacuum perpendicular to the surface to avoid unphysical interactions between neighboring slabs. One carbon atom is replaced by nitrogen in the given supercell. The generalized gradient approximation (GGA) and the exchange-correlation (XC) functional parametrized by Perdew and Wang (PW91) [49] were used together with a plane-wave basis-set energy cutoff of 400 eV and an $11 \times 11 \times 1$ Monkhorst-Pack [50] k -point sampling of the Brillouin zone. We found a planar lattice structure after geometrical relaxation following N doping, in agreement with Ref. [93].

For the revised Chen’s derivative rule, idealized model tips of pure s , pure p_z , and a combination of $(s + p_z)/\sqrt{2}$ orbitals are initially considered. Since N-doped graphene has been experimentally probed with tungsten tips [93], we consider the previously introduced three tungsten tip models with different sharpnesses and compositions: W_{blunt} , W_{sharp} and $W_{\text{C-apex}}$.

Geometrical relaxations, search for the magnetic ground state, and electronic structure calculations of an Mn monomer, Mn dimer, and Mn_2H on the $\text{Ag}(111)$ surface have been reported in Ref. [94], and an antiferromagnetic ground state for the $\text{Mn}_2\text{H}/\text{Ag}(111)$ system has been found. We use their electronic structure results in the present paper; for more details on the modeled geometries and DFT calculations, please refer to Ref. [94]. In their STM experiments, silver tips have been used. Therefore, we consider blunt tips as an adatom adsorbed on the hollow site of the silver surface in two different orientations, *i.e.*, $\text{Ag}(001)$ and $\text{Ag}(111)$, in a 3×3 surface unit cell and at least 15 Å wide vacuum perpendicular to the surface to avoid unphysical interactions due to the slab geometry. The GGA and XC functional parametrized by Perdew, Burke, and Ernzerhof (PBE) [84] are employed. Moreover, a plane-wave basis-set energy cutoff of 250 eV and

an $11 \times 11 \times 1$ Monkhorst-Pack [50] k -point grid centered on the Γ -point are used. The convergence criterion for the forces acting on relaxed atoms (adatom and first full layer) is $0.01 \text{ eV}/\text{\AA}$.

4.2 Graphene – N

Experimental studies have shown that in the constant-height STM images of N-doped graphene, the tunneling current above the N atom is significantly lower than above the neighboring C atoms [93]. At first sight, this seems to be in contradiction to the fact that the density of states of the N atom is larger than that of the neighboring C atoms close to the Fermi level. The current dip above the N atom has been explained by a destructive interference between the orbitals of the N and the nearest-neighbor C atoms, *i.e.*, a pure sample effect [93]. Such a quantum interference effect is an ideal candidate to study with the revised Chen’s method.

4.2.1 Comparison of simulation methods

We have calculated constant-height STM images of the N-doped graphene surface using four different tunneling models: 3D-WKB, Tersoff-Hamann, revised Chen, and Bardeen. The constant-height STM simulations were performed at relatively small tip-sample distance (4 \AA) at two selected bias voltages ($\pm 0.4 \text{ V}$) corresponding to the STM experiments by Telychko *et al.* [93]. First, the 3D-WKB method has been used. This model takes into account the orbital characteristics and electronic structure of the sample and the tip as well, but uses the atom-projected density of states (amplitudes) instead of the explicit wave functions (amplitudes and phases); thus, electron interference effects are not considered. Using the 3D-WKB method, the N atom always shows up as a protrusion in the STM image as is expected from the relation of the density of states of the N and C atoms [93].

Next, we focus on the comparison of the revised Chen’s method with two conventional STM simulation models: Tersoff-Hamann and Bardeen. Fig. 4.2.1 shows that the STM images obtained by the revised Chen’s method using a pure s tip quantitatively agree with those calculated by the Tersoff-Hamann model, *i.e.*, a correlation value of 1 between the corresponding STM images is found. We

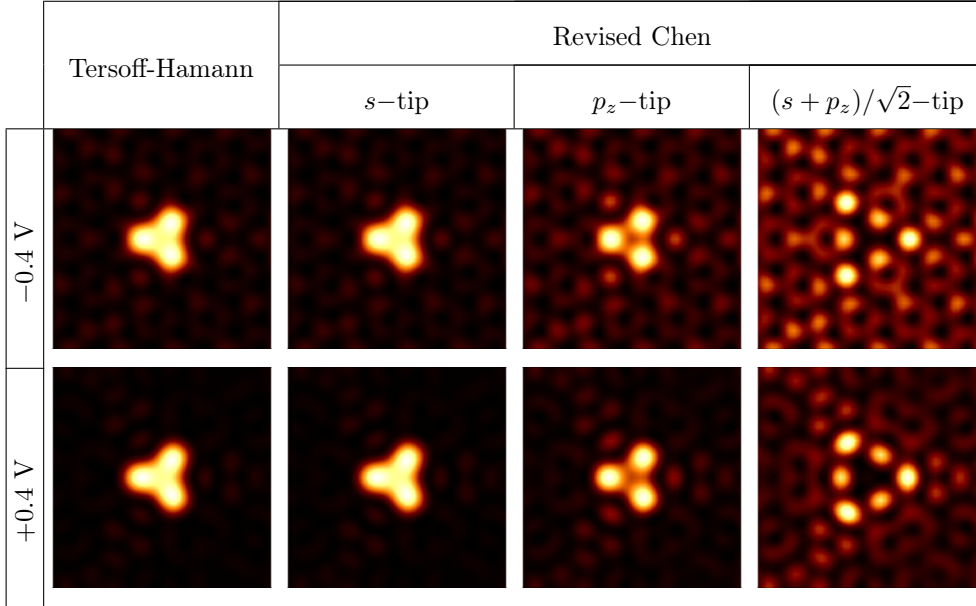


Figure 4.2.1: Constant-height STM images of N-doped graphene at 4 Å tip-sample distance and ± 0.4 V bias. Comparison between the Tersoff-Hamann model and revised Chen method with selected tip orbitals: s , p_z , $(s + p_z)/\sqrt{2}$. The N defect is located in the middle of the images. Adapted from Ref. [P6]

obtain qualitatively similar STM images assuming an ideal tip of pure p_z orbital, where the current dip above the N atom is slightly more pronounced than with the s tip. For these tip models, the energy-independent weighting factors were used (for more details see Sec. 2.2.2.3 (i)). Furthermore, we point out the importance of quantum interference of tip orbitals in Fig. 4.2.1. Therefore, we consider an ideal tip of a linear combination of s and p_z orbitals of equal weights. As can be seen, the $(s + p_z)/\sqrt{2}$ -tip shows a remarkable contrast change compared to the STM images of pure s or pure p_z orbitals, where the current dip above the N atom is even more pronounced and the bright triangle showing C atoms is larger and reversed. This effect is clearly related to the orbital interference of the tip's s and p_z states, and shows an additional effect to the destructive quantum interference arising from the sample's C – N bond in the formation of the STM contrast of N-doped graphene. We stress again that the $s - p_z$ tip-orbital interference results in a much more pronounced current dip above the N atom than the destructive quantum interference of the sample itself; the latter is imaged by the Tersoff-Hamann method. Interestingly, STM images obtained by the $(s + p_z)/\sqrt{2}$ -tip resemble results calculated by a C(111) tip model (see Ref. [93]) having these

dominant orbitals in the electronic structure. Note that both types of STM contrast of N-doped graphene in Fig. 4.2.1 have been experimentally observed in Ref. [93].

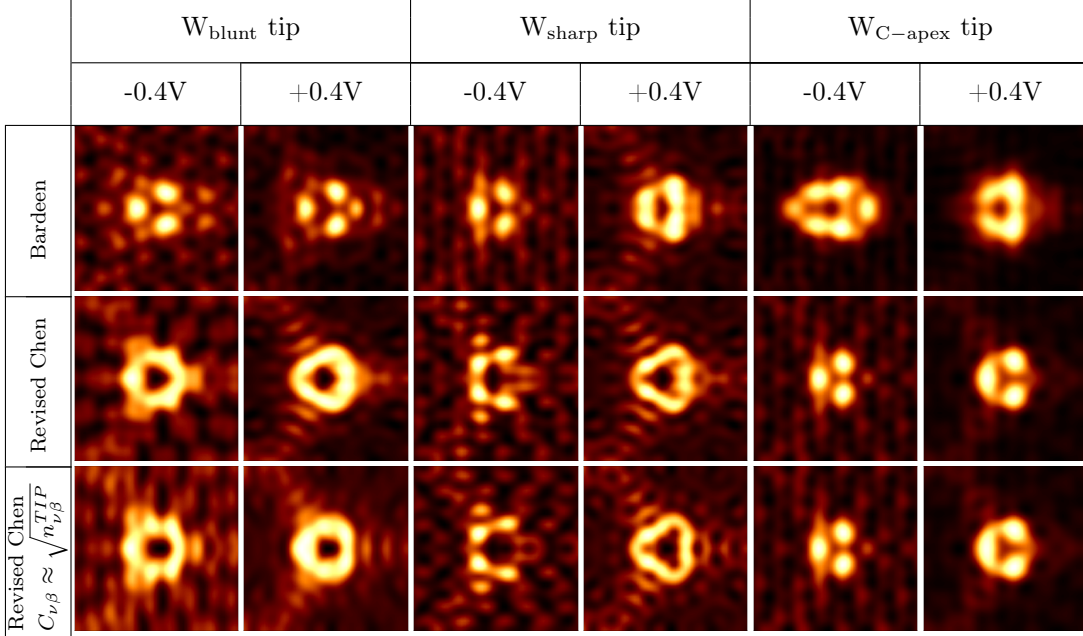


Figure 4.2.2: Constant-height STM images of N-doped graphene at 4 Å tip-sample distance and ± 0.4 V bias. Comparison between the Bardeen’s model and revised Chen’s method with two different choices of the $C_{\nu\beta}$ weighting coefficients in Eq. (2.2.16) for three tungsten tip models: W_{blunt} , W_{sharp} and $W_{\text{C-apex}}$. Room temperature was assumed, corresponding to the STM experiments in Ref. [93]. The N defect is located in the middle of the images. Adapted from Ref. [P6]

Fig. 4.2.2 and Table 4.2.1 show qualitative and quantitative comparisons of the revised Chen’s method with Bardeen’s method using three different tungsten tip models, which have also been used in previous studies of STM imaging of HOPG (see Secs. 3.3.3 and 3.3.4). Moreover, we compare two different choices of the $C_{\nu\beta}$ weighting coefficients of the revised Chen’s method [see Secs. 2.2.2.3 (ii) and 2.2.2.3 (iii)] and good qualitative agreement is obtained.

We find that using these methods, the current dip above the N atom is always present in the STM images in Fig. 4.2.2. The degree of agreement between the Bardeen’s and revised Chen’s methods, reported as correlation coefficients between corresponding STM images in Table 4.2.1, depends on the actual tip geometry and electronic structure, and hence the bias voltage. Let us recall that we expand the tip wave functions/density of states around the tip-apex atom and calculate the $C_{\nu\beta}$ coefficients in the Wigner-Seitz sphere of the tip-apex atom in

Bardeen vs. Chen	W _{blunt} tip		W _{sharp} tip		W _{C–apex} tip	
	–0.4 V	+0.4 V	–0.4 V	+0.4 V	–0.4 V	+0.4 V
$C_{\nu\beta}$ in Eq. (2.2.16)	0.81	0.82	0.78	0.89	0.73	0.91
$C_{\nu\beta} \approx \sqrt{n_{\nu\beta}^{TIP}}$	0.71	0.81	0.62	0.79	0.74	0.92

Table 4.2.1: Quantitative comparison between Bardeen’s model and the revised Chen’s method: calculated correlation coefficients between STM images in Fig. 4.2.2. Adapted from Ref. [P6]

the revised Chen’s method. The accuracy of such an expansion depends strongly on the neighboring sub-apex atoms’ electronic structure and on the tip-sample distance. For example, for sharp tips, the contribution of sub-apex atoms to the tunneling current is more important than for blunt tips. On the other hand, the larger the tip-sample distance, the better the agreement of STM images between the two methods. The reason is that with increasing tip-sample separation, the effect of the local tip geometry decreases. At larger tip-sample distances, we find that the current dip above the N atom vanishes and a rounded triangular pattern is obtained, leaving the three nearest-neighbor C atoms visible, similarly to the Tersoff-Hamann results in Fig. 4.2.1.

Overall, we find good agreement between the Bardeen’s and revised Chen’s methods in Fig. 4.2.2 and Table 4.2.1. Calculated correlation values are above 0.7, except for the W_{sharp} tip at –0.4 V bias and $C_{\nu\beta} \approx \sqrt{n_{\nu\beta}^{TIP}}$. We find better correlation for $C_{\nu\beta}$ in Eq. (2.2.16) than for the $C_{\nu\beta} \approx \sqrt{n_{\nu\beta}^{TIP}}$ approximation used in the revised Chen’s method, with the exception of the W_{C–apex} tip. Moreover, systematically better correlation between the Bardeen’s and the revised Chen’s methods is found for +0.4 V than for –0.4 V bias voltage. Note that the large difference between STM images of the W_{sharp} tip with different bias polarities can be explained by the asymmetric electronic structure of the tip apex around the Fermi level [51].

4.2.2 The effect of strain

It is interesting to investigate the effect of strain on the obtained STM contrast. Figure 4.2.3 shows a comparison between STM images calculated for three dif-

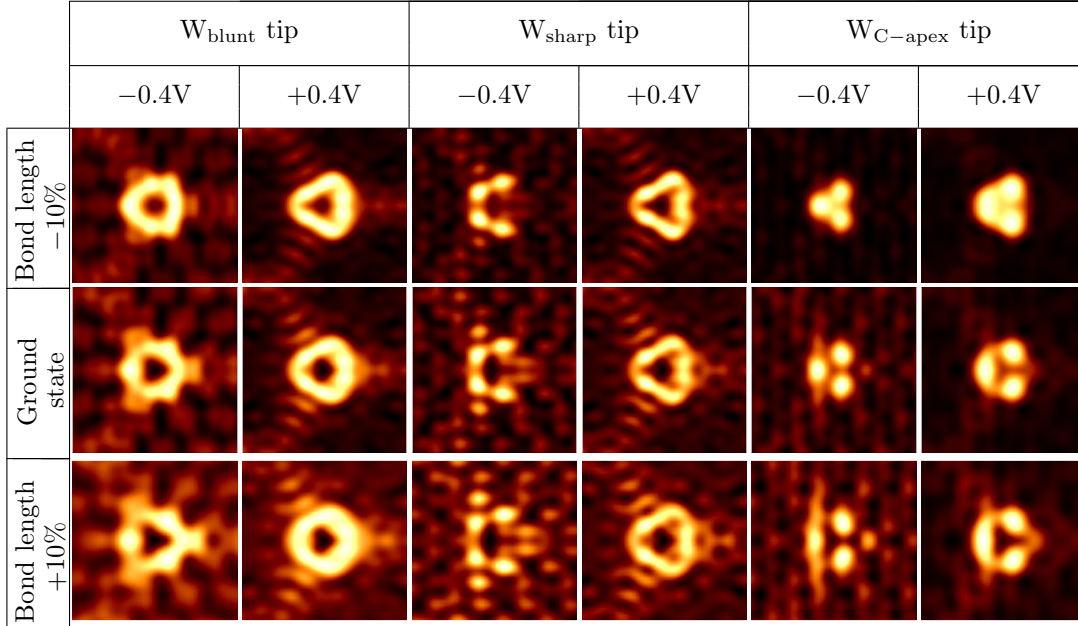


Figure 4.2.3: Effect of strain on constant-height STM images of N-doped graphene at 4 Å tip-sample distance and ± 0.4 V bias using the revised Chen’s method with three tungsten tip models: W_{blunt} , W_{sharp} , and $W_{\text{C-apex}}$. The ground-state N-doped graphene geometry obtained by DFT and two other structures with bond lengths varied by $\pm 10\%$ relative to the ground state are compared. Adapted from Ref. [P6]

ferent N-doped graphene geometries with bond lengths varying by $\pm 10\%$ relative to the ground-state structure, which has been obtained by DFT calculation with C – N and C – C bond lengths of 1.42 Å. Generally, we observe that the main features of the STM contrast do not change with the applied strain. This is quantitatively confirmed by correlation coefficients being above 0.93 for each tip and bias combination calculated between images within each column of Fig. 4.2.3. We find a tendency of spatially extended brighter features in the STM images upon elongation of the bonds.

4.2.3 The effect of tip rotation

Constant-height STM images have been calculated above the N-doped graphene surface with the tungsten tip models at 4 Å tip-sample distance. We considered tip rotations around the axis perpendicular to the sample surface. This corresponds to $\vartheta_0 = 0^\circ$, and in this case rotations with respect to φ_0 and ψ_0 are equivalent; thus, we fixed $\psi_0 = 0^\circ$ and rotated the tip by φ_0 in 10° steps. Since a more asymmetric tip is expected to have a larger tip rotational effect, we present

results obtained by the W_{sharp} tip at +0.4 V bias voltage. Selected STM images are shown in Fig. 4.2.4.

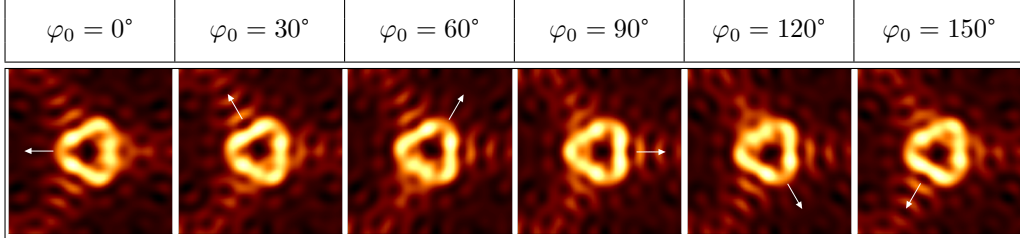


Figure 4.2.4: Tip rotation effect on the constant-height STM images of N-doped graphene calculated with W_{sharp} tip at 4 Å tip-sample distance and +0.4 V bias voltage. The rotation axis of the tip is perpendicular to the surface ($\vartheta_0 = \psi_0 = 0^\circ$). The orientations of the brightest features are indicated by white arrows in each STM image. Adapted from Ref. [P6]

Due to the C_{2v} symmetry of the tip, the same image is obtained for $\varphi_0 = 180^\circ$ as for $\varphi_0 = 0^\circ$. We find that the current dip above the N atom is always present independently of the degree of tip rotation by φ_0 , but the intensity of the current above the surrounding C atoms changes with the tip rotation. There are certain directions denoted by white arrows in Fig. 4.2.4, where the brightest features occur that correspond to the largest currents above or close to nearest-neighbor C atoms. These indicated directions rotate two times faster than the tip rotation by φ_0 itself. The finding that such kind of tip rotations, where the z axis of the tip is not tilted with respect to the z axis of the sample ($\vartheta_0 = 0^\circ$), affect the secondary features of the STM image is in agreement with previous results using the 3D-WKB method, *e.g.* for HOPG sample, see Sec. 3.3.

In Fig. 4.2.5, we extracted line sections of the constant-height STM images presented in Fig. 4.2.4. The line along the x direction contains the N atom and its nearest-neighbor (C_1) and third-nearest-neighbor (C_3) carbon atoms. The line along the y direction contains the other two nearest-neighbor carbon atoms (C'_1 and C''_1); see the inset of Fig. 4.2.5(a). The symmetries of the sample and the tip are reflected in these line sections as well. We find indeed that the current value above the N atom is insensitive to the tip rotation, and it is almost the smallest current value in the entire scan area. We can also see that the brightest features, *i.e.*, the largest current values of the STM images, are actually not located above the carbon atoms, but rather above the hollow positions of the honeycomb lattice.

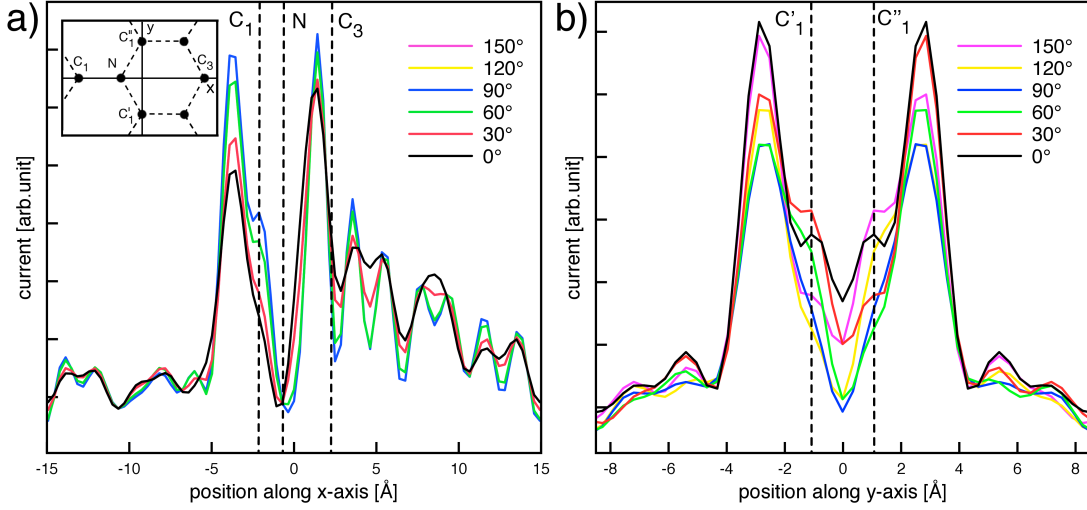


Figure 4.2.5: Current profiles along the x [subfigure (a)] and y [subfigure (b)] directions of the N-doped graphene surface (see inset) as a function of tip rotation with respect to φ_0 ($\vartheta_0 = \psi_0 = 0^\circ$). Adapted from Ref. [P6]

4.3 AgMn₂H

Sachse *et al.* found that Mn₂H on the Ag(111) surface can produce STM images with single or double features, depending on the magnetic coupling between Mn atoms [94]. Double features have been obtained at positive bias employing the Tersoff-Hamann method for an antiferromagnetic Mn-Mn coupling, which corresponds to the energetically favored ground state. The calculated relaxed geometry of antiferromagnetic Mn₂H on the Ag(111) surface is shown in Fig. 4.3.1. We consider this system and perform an investigation of its STM imaging depending on three employed tunneling models: Bardeen, revised Chen, and Tersoff-Hamann. Using the decomposition of the tunneling current in the revised Chen's method, we are able to identify the physical origin of the observed dip above Mn₂H.

The calculated constant-height STM images at small bias voltages (± 0.1 V) using two silver blunt tip models (Ag(001) and Ag(111)) are shown in Fig. 4.3.2. Correlation coefficients between STM images obtained by the Bardeen's and revised Chen's methods are reported in Table 4.3.1. First of all, we find excellent quantitative agreement between the STM images obtained by the Bardeen's and revised Chen's methods for the Ag(111) tip and good agreement for the Ag(001) tip. Recalling that the revised Chen's method is 25 times faster than Bardeen's

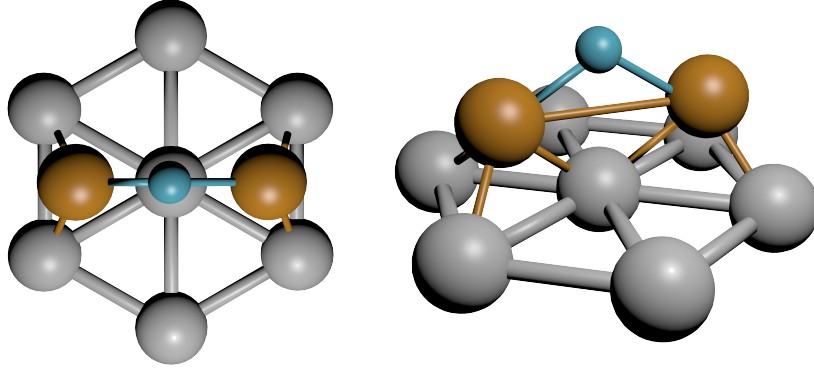


Figure 4.3.1: Calculated relaxed geometry of antiferromagnetic Mn₂H on the Ag(111) surface. Data is taken from Ref. [94]. The figure is adapted from Ref. [P6]

Bardeen vs. Chen	Ag(001) tip		Ag(111) tip	
	-0.1 V	+0.1 V	-0.1 V	+0.1 V
$C_{\nu\beta}$ in Eq. (2.2.16)	0.72	0.88	0.97	0.95

Table 4.3.1: Quantitative comparison between Bardeen’s model and the revised Chen’s method: calculated correlation coefficients between STM images in Fig. 4.3.2. Adapted from Ref. [P6]

method in practical STM calculations, this clearly indicates that our proposed model is a very promising tool for STM simulations in the future. Moreover, the results in Fig. 4.3.2 show that the geometry and electronic structure of the tip have a considerable effect on the STM imaging of Mn₂H/Ag(111): the Ag(001) tip provides single protrusion and the Ag(111) tip provides double features of the STM images at both bias polarities using both the Bardeen’s and revised Chen’s methods. However, the Tersoff-Hamann model provides qualitative agreement with these at selected bias voltages only: At -0.1 V, a single protrusion is obtained, while at +0.1 V, a double feature is visible. The comparison of the Tersoff-Hamann results with those obtained by the revised Chen’s method suggests a contradiction with the general assumption of Ag tips being of *s* orbital character [94]. In order to understand the components of the tunneling current above the H atom, the decomposition according to Eq. (2.2.11) in the revised Chen’s method is employed.

Figure 4.3.3 shows the results of the current decomposition according to tip

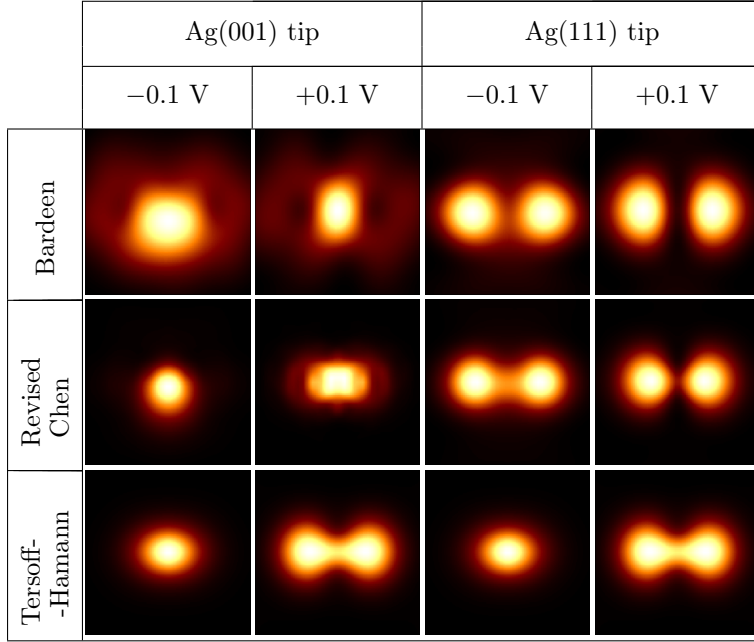


Figure 4.3.2: Constant-height STM images of antiferromagnetic Mn₂H on the Ag(111) surface simulated at 5 Å Ag surface-tip distance and ± 0.1 V bias with three different methods (Bardeen, revised Chen, and Tersoff-Hamann) and two blunt tip models: Ag(001) and Ag(111). A temperature of 7 K was assumed, corresponding to the STM experiments in Ref. [94]. Note that results of the Tersoff-Hamann model are shown for comparison reasons only, and no explicit tip electronic structure is considered there. Adapted from Ref. [P6]

orbital characters. Interestingly, we find that the Ag(001) tip does not behave as an s -type tip at +0.1 V bias [see Fig. 4.3.3(a)]. The major contributions are from the p_x , p_y , d_{xz} and d_{yz} tip orbitals, and there are destructive interferences arising from $p_x - d_{xz}$ and $p_y - d_{yz}$ tip orbitals. This explains the qualitative disagreement between the Tersoff-Hamann and revised Chen’s results for the Ag(001) tip at +0.1 V bias. On the other hand, using the Ag(111) tip at -0.1 V bias, the major contribution is clearly from the tip’s s orbital (see Fig. 4.3.3(b)). Apart from that, there is a strong $s - p_z$ destructive tip interference that is missing in the Tersoff-Hamann model, causing the observed qualitative difference in the STM images for the Ag(111) tip at -0.1 V bias. Moreover, we find similar current decomposition characteristics for the Ag(001) tip at -0.1 V bias and for the Ag(111) tip at +0.1 V bias, as Fig. 4.3.3(b) shows, with a dominating s orbital contribution from the tip. For these tip and bias-voltage combinations, a good qualitative agreement of the STM images between the revised Chen’s and Tersoff-Hamann results is obtained. Our findings suggest that although the quality of the STM contrast (single or double feature) is mainly determined by the electronic states of the

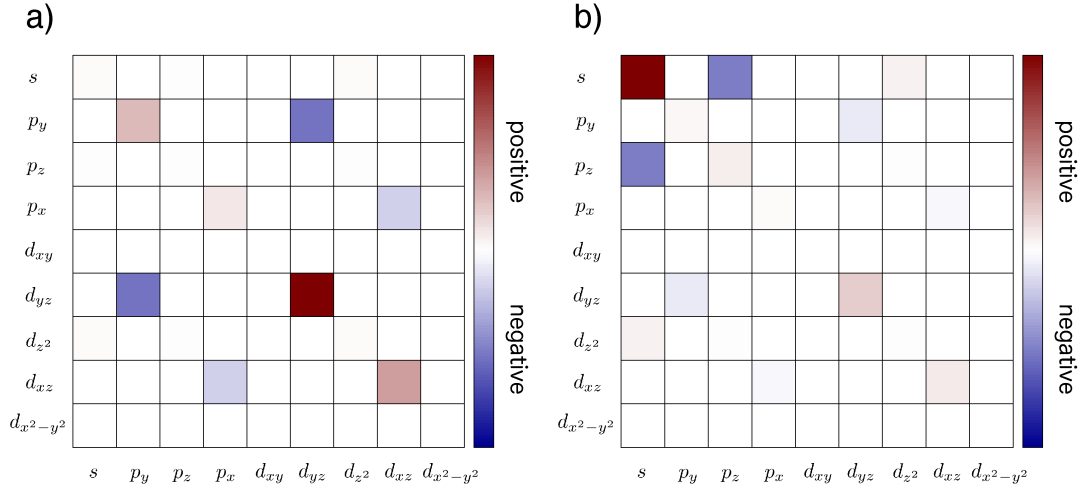


Figure 4.3.3: Decomposition of the tunneling current 1.83 \AA above the H atom in $\text{Mn}_2\text{H}/\text{Ag}(111)$ (corresponding to Fig. 4.3.2) using Eq. (2.2.11). Diagonal: direct (positive) contributions; off-diagonal: interference (positive or negative) contributions to the current. (a) Ag(001) tip at bias voltage $V = +0.1$ V; (b) Ag(111) tip at bias voltage $V = -0.1$ V. Adapted from Ref. [P6]

sample surface that can be captured by employing the Tersoff-Hamann model, the tip electronic structure and, in the present case, an $s - p_z$ destructive tip interference can cause a contrast change.

4.3.1 The effect of temperature

It is important to highlight the effect of temperature on the obtained STM contrast. Temperature enters into the tunneling model in two ways: (i) the energy window for calculating the tunneling channels, where nonzero temperature results in an extension of the energy window due to the Fermi distribution [see Eq. (2.1.5)] and (ii) the thermal broadening of the electron states. In the Bardeen model the tunneling is assumed to be elastic and energy conservation is ensured by the Dirac- δ in Eq. (2.1.5). At finite temperature, the thermal broadening of the electron states has to be taken into account. This is usually done by approximating the Dirac- δ with a Gaussian function:

$$\delta(E_\nu - E_\mu - eV) \sim \frac{1}{\sqrt{2\pi\Delta^2}} \exp\left[-\frac{(E_\nu - E_\mu - eV)^2}{2\pi\Delta^2}\right]. \quad (4.3.1)$$

In Eq. (2.1.5), in principle, all $\mu - \nu$ transitions have to be considered with the probability given by this Gaussian factor (and $|M_{\mu\nu}|^2$) when calculating the tunneling current, but, practically, transitions with significantly low probability can be neglected, *e.g.*, if $|E_\mu - E_\nu - eV| > 3\Delta$ where $\Delta = k_B T$ is the thermal broadening of the states at T temperature, with k_B the Boltzmann constant.

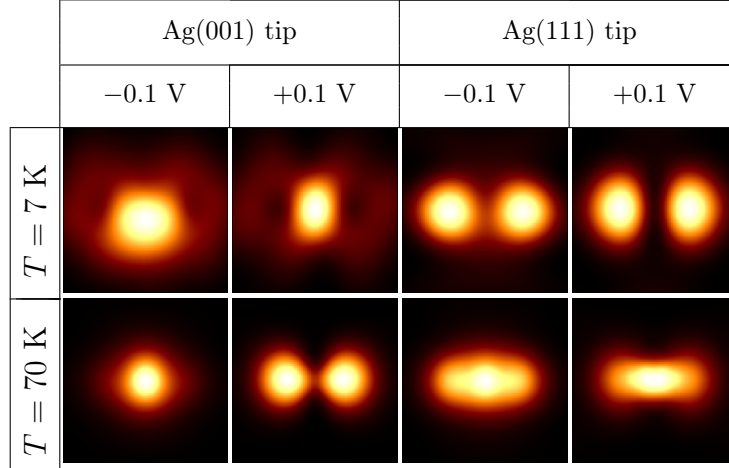


Figure 4.3.4: Effect of temperature on constant-height STM images of antiferromagnetic Mn₂H on the Ag(111) surface simulated at 5 Å Ag surface-tip distance and ± 0.1 V bias using the revised Chen’s method with two blunt tip models: Ag(001) and Ag(111). Temperatures of $T = 7$ K and 70 K are compared. Adapted from Ref. [P6]

Figure 4.3.4 shows a comparison between STM images calculated at $T = 7$ K and 70 K, with the former corresponding to the temperature used in the experiments of Ref. [94]. We find a diverse behavior of the STM contrast at the higher temperature depending on the tip and bias voltage. The contrast (single protrusion) is preserved for the Ag(001) tip at -0.1 V bias only. The other three images show different contrasts at the two temperatures. Upon increasing the temperature, for the Ag(001) tip at $+0.1$ V, the single protrusion contrast changes to double features, while for the Ag(111) tip at both bias voltages, the double protrusion contrast changes to an elongated single feature with the maximal current above the H atom of Mn₂H. This diversity of simulated STM contrasts points to the importance of the correct choice of temperature in STM simulations if a meaningful explanation of given experimental STM data is desired.

Chapter 5

Summary, concluding remarks

5.1 Summary

We introduced an orbital-dependent electron tunneling model and implemented it within the atom superposition approach based on 3D-WKB theory, for simulating STM and STS. We analyzed the convergence and the orbital contributions to the tunneling current above the W(110) surface. We found that the $d_{3z^2-r^2} - d_{3z^2-r^2}$ contribution is the largest, and depending on the tip position other d states can gain importance as well. We also studied the corrugation-inversion effect. Using the independent orbital approximation no corrugation reversal was obtained at all. Employing the orbital-dependent model we found corrugation reversals depending on the bias voltage in accordance with the work of Heinze et al. [45] and also on the tip-sample distance. Explaining this effect we highlighted the role of the real-space shape of the orbitals involved in the tunneling. Moreover, we calculated corrugation-inversion maps considering different tip models and found two qualitatively different behaviors based on the tip orbital composition. Our results indicate that using a W-tip anticorrugation can be observed not only at negative bias voltages but also at positive bias at reasonably short tip-sample distances. Simulation of STM images made the corrugation-inversion effect more apparent. A good agreement has been found by comparing STM images calculated by our model to Tersoff-Hamann and Bardeen results. The computational efficiency of our model is remarkable as the k -point samplings of the surface and tip Brillouin zones do not affect the computation time, in contrast to the Bardeen method.

Our model is capable of simulating STM images with arbitrary tip orienta-

tions. We highlighted the role of the real-space shape of the electron orbitals involved in the tunneling, and analyzed the convergence and the orbital contributions of the tunneling current above the W(110) surface depending on the orientation of a model tungsten tip. We found that tip rotations around the z -axis of the tip apex atom do not change the dominant current contributions, while other rotations can change the tip character of the dominant transitions. We also studied atomic contrast changes upon tip rotation. We found that the zero contours of the current difference above the surface top and hollow positions have a complex tip-sample distance and bias voltage dependence on the tip orientation. The relative apparent heights of these two surface positions are directly related to the calculated current difference. Simulating STM images at constant-current condition, we found that their quality depends very much on the tip orientation. Some orientations result in protrusions on the images that do not occur above W atoms. The presence of such apparent atom positions makes it difficult to identify the exact position of surface atoms. It is suggested that this tip orientation effect should be considered in the evaluation of experimental STM images on other surfaces as well. We concluded that our computationally efficient tunneling model could prove to be useful in obtaining more information on the local tip geometry and orientation by comparing STM experiments to a large number of simulations with systematically varied tip orientations.

As a next case study we simulated spin-polarized scanning tunneling microscopy (SP-STM) above magnetic surfaces. Applying our method, we analyzed the bias-dependence of the orbital contributions to the tunneling current above the Fe(110) surface, and found a shift of the relevant tip s contributions close to zero bias toward $d-d$ tunneling at higher bias. We showed that spin-polarized tunneling has a considerable effect on the tip-sample distance where atomic contrast inversion occurs, and the tip magnetization direction and tip orbital composition play a crucial role as well. Taking an s -tip, our findings showed qualitative agreement with the Tersoff-Hamann method and with Ref. [45] concerning the corrugation character of the Fe(110) surface. We explained our results based on the complex interplay of the real-space orbital shapes involved in the tunneling and the energy-dependent orbital-decomposed PDOS of the sample and the tip. We also demonstrated the contrast inversion by simulating SP-STM images.

To test our model on a bit more complex surfaces combined with different realistic tip models we turned to HOPG. We studied the STM image contrast of

the HOPG(0001) surface in the tunneling regime as a function of the local orientation of a set of tungsten tips. Employing the 3D-WKB tunneling approach, we demonstrated that the relative local orientation of the STM-tip apex with respect to the HOPG substrate can have a considerable effect on the HOPG STM contrast. Depending on the STM tip-apex structure and composition, applied bias and relative orientation with respect to the substrate, substantially different effects, ranging from conservation to inversion of the STM contrast, were observed. These results were rationalised in terms of the tip-rotation mediated contribution of tip-apex electronic states of different orbital characters to the tunneling current. For a sharp tungsten tip the HOPG contrast inversion between opposite bias polarities was explained by the different weights of the tip orbital characters involved in the tunneling that is due to the asymmetry of the tip electronic structure with respect to its Fermi level. We also compared the 3D-WKB and Bardeen STM simulation models with each other and with experiments in terms of bias-voltage-dependent STM topography brightness correlations. We found quantitatively good agreement for particular tip models and bias voltage ranges and discussed the identified differences in view of the construction of the two tunneling models. In view of the experiments, we can also conclude that the two tunneling methods perform at the same quantitative reliability. Importantly for experimental STM analysis of HOPG, the simulations indicate that particular local tip-reconstructions with no orientational change of the dominating $d_{3z^2-r^2}$ tip-apex orbital state affect only the secondary features of the HOPG STM contrast, leaving the primary contrast unchanged, thus resulting in a stable tip. Such tip orientations are found to be responsible for ‘striped’ images observed in experiments. Conversely, tip-rotations leading to enhanced contributions from $m \neq 0$ tip-apex electronic states can cause a triangular- hexagonal change in the primary contrast, indicating a likely tip instability.

In scanning probe experiments the scanning tip is the source of one of the largest uncertainty as very little is known about its precise atomic structure and stability. Since the atomic structure and electronic properties of the tip apex can strongly affect the contrast of STM images, it is very difficult to experimentally obtain predictive STM images in certain systems. To tackle this problem we proposed a statistical correlation analysis method to obtain information on the local geometry and orientation of the tip used in STM experiments. We defined the relative brightness correlation of constant-current topographs between exper-

imental and simulated data, and analyzed it statistically for the HOPG(0001) surface in combination with two tungsten tip geometries in 18144 orientations each. The simulations were performed using the 3D-WKB electron tunneling theory based on first principles electronic structure calculations. We found that a blunt tip model provides better correlation with the experiment for a wider range of tip orientations and bias voltages than a sharp tip model. A favored sharp tip is indicated at low negative bias only. From the correlation distribution we proposed particular tip orientations that are most likely present in the STM experiment, and likely excluded other orientations. Importantly, we find that the favored relative tip-sample orientations do not correspond to high symmetry setups that are routinely used in standard STM simulations. The demonstrated combination of large scale simulations with experiments is expected to open up the way for a more reliable interpretation of STM data in the view of local tip geometry effects. Moreover, the introduced correlation analysis method could be useful for other scanning probe imaging techniques as well.

Finally, we revised Chen's derivative rule for the purpose of computationally efficient STM simulations. The revised Chen's model includes the electronic structure and arbitrary spatial orientation of the tip by taking appropriate weighting coefficients of tunneling matrix elements of different tip-orbital characters. Interference of tip orbitals in the STM junction is included in the model by construction. We demonstrated the reliability of the model by applying it to two functionalized surfaces of recent interest where quantum interference effects play an important role in the STM imaging process: N-doped graphene and an anti-ferromagnetic Mn_2H complex on the $\text{Ag}(111)$ surface. We found that the revised Chen's model is 25 times faster than the Bardeen method concerning computational time, while maintaining good agreement. Our results show that the electronic structure of the tip has a considerable effect on STM images, and the Tersoff-Hamann model does not always provide sufficient results in view of quantum interference effects. For both studied surfaces, we highlighted the importance of interference between s and p_z tip orbitals that can cause a significant contrast change in the STM images. Moreover, our findings show that stretched bonds have a minor effect on the main features of the STM contrast of the Graphene – N system, and temperature is an important factor to be taken into account in STM simulations if aiming at accuracy in comparison with experiments, as we demonstrated for the AgMn_2H system. Our method, implemented in the bSKAN code,

thus provides a fast and reliable tool for calculating STM images based on Chen's derivative rule, taking into account the electronic structure and local geometry of the tip apex.

5.2 Outlook

The introduced tunneling models, methodology and code base turned out to be an efficient and useful tool for STM/SP-STM simulation and analysis. Some applications are out of the scope of this thesis, but worth mentioning to get an idea of the possible fields of applications.

The tunneling model was also extended to calculate spin transfer torque (STT) in magnetic STM junctions. Palotás *et al.* studied the Fe/W(110) surface and showed that the ratio between the STT and the spin-polarized charge current is not constant, and more importantly, it can be tuned by the bias voltage, tip-sample distance, and magnetization rotation, hence it can be enhanced by selecting the proper bias voltage [P8].

Using the revised Chen method Walls *et al.* simulated (110)-terminated magnetite surface and investigated oxygen induced surface stabilization [95]. Liu *et al.* studied the surface defects of $\text{CH}_3\text{NH}_3\text{PbBr}_3$ perovskite [96], Turansky *et al.* studied the limits of SPM subatomic resolution in imaging orbital magnetic features [97]. Lee *et al.* used the Chen method for comparing experimental and simulated STM images of thin layers of Mo-oxides on Au(111) [98]. The nitrogen-doped graphene system was also studied by Neilson *et al.* focusing on doping-induced variations of the local work function [99] while Ly *et al.* carried out a detailed investigation of $\text{Cu}_2\text{O}(111)$ surface [100]. Cossu *et al.* studied a strain-induced stripe phase in the charge-ordered single layer NbSe_2 , and STM images were calculated to visualize the charge density waves [101]. Szitás *et al.* investigated the adsorption of azobenzene molecules on hexagonal boron nitride on Rh(111), and predicted low-temperature bias-voltage-dependent STM images by using the revised Chen method [102]. Lee *et al.* simulated STM images of ultrathin CuI layers on Cu(111), and compared them to experimental results [103].

The 3D-WKB method was intensively used for studying skyrmionic spin structures by Palotás *et al.* High resolution SP-STM calculations were used to characterize metastable spin structures in the $(\text{Pt}_{1-x}\text{Ir}_x)\text{Fe} / \text{Pd}(111)$ ultrathin magnetic

film [104]. The tunneling spin transport characteristics of a magnetic skyrmion in SP-STM were described theoretically in [105]. The spin-polarized charge current and tunneling spin transport vector quantities (such as the longitudinal spin current and the spin transfer torque), were calculated within the same theoretical framework. A connection between the conventional charge current SP-STM image contrasts and the magnitudes of the spin transport vectors was shown, that enables the estimation of tunneling spin transport properties based on experimentally measured SP-STM images. Using the same theoretical framework, the high-resolution tunneling electron charge and coupled spin transport properties of a variety of Néel- and Bloch-type skyrmions were investigated in [106]. Recently, the tip-position-dependence of the spin transfer torque efficiency was reported above skyrmionic spin textures with various topologies [107]. This enables the optimization of the creation and annihilation of topological magnetic objects on surfaces by the SP-STM tip.

As the above list indicates the developed theoretical and computational STM methods presented in this dissertation are already being actively used for solving a wide range of surface science problems, and due to their computational efficiency they are expected to be key methods in the future as well.

5.3 Thesis points

The major achievements of my research are summarized in the following thesis statements:

1. I made essential contributions to the theoretical development and implementation of the orbital-dependent 3D-WKB electron tunneling model for the simulation of high-resolution STM and SP-STM images in a computationally efficient way since the k -point samplings of the surface and the tip Brillouin zones do not affect the computational time in this new model [P1]. I demonstrated the validity of the model by investigating the corrugation inversion phenomenon depending on the tip-sample distance and bias voltage observed on the nonmagnetic W(110) [P1] and on the magnetic Fe(110) surfaces [P3]. I explained the observed STM contrast inversion based on the real-space shape of the electron orbitals involved in the tunneling, and in the magnetic SP-STM case based on the interplay of the real-space electron orbitals and the spin- and energy-dependent orbital-decomposed projected

- electron densities of states of the sample and the tip. In both cases, I found a good agreement by comparing STM images calculated by the 3D-WKB model to results obtained by Tersoff-Hamann and Bardeen theories [P1,P3].
2. I developed and implemented the treatment of asymmetric tips in the STM junction in a novel way by considering arbitrary tip orientations in the orbital-dependent 3D-WKB electron tunneling model [P2]. Focusing on the corrugation inversion phenomenon, I studied the W(110) surface with numerous tip orientations, and the complex dependence of the contrast inversion on the tip-sample distance, bias voltage, and tip orientation was uncovered and explained. I showed that – even in this case of a relatively simply structured surface – the relative orientation of the tip and sample has a considerable effect on characteristics of the corrugation inversion as well as on the STM images [P2]. I also studied the tip-rotational effects on the STM images of the highly oriented pyrolytic graphite (HOPG) surface. Focusing on the favorable conditions for tip stability, I pointed out that local tip-rotations maintaining a major contribution of the $d_{3z^2-r^2}$ tip-apex state to the STM current affect only the secondary features of the HOPG STM contrast resulting in ‘stripe’ formation and leaving the primary contrast unaltered [P4]. Conversely, tip-rotations leading to enhanced contributions from $m \neq 0$ tip-apex electronic states can cause a triangular-hexagonal change in the primary contrast [P4].
 3. I introduced a novel correlation analysis method to quantitatively evaluate the degree of agreement between STM images obtained by different theoretical methods or experimental data [P5]. I applied the method on the HOPG surface in combination with different tungsten tips, and a detailed comparison among 3D-WKB and Bardeen theoretical methods and experimental data was provided. I found that both theoretical methods provide the same quantitative reliability of correlation coefficients in comparison with the experimental STM images [P5]. Moreover, I introduced a statistical correlation analysis method to obtain information on the local geometry and orientation of the tip used in STM experiments based on large scale simulations. I demonstrated the applicability of the method considering the HOPG surface in combination with tungsten tip models of two different apex geometries, each in close to 20000 different orientations. I found that a

blunt tip model provides better correlation with the experiment for a wider range of tip orientations and bias voltages than a sharp tip model [P5].

4. I revised Chen's derivative rule for electron tunneling for the purpose of computationally efficient simulations of STM based on first-principles electronic structure data and implemented it in the bSKAN code [P6]. The revised model allows the weighting of tunneling matrix elements of different tip-orbital characters by an arbitrary energy-independent choice or based on energy-dependent weighting coefficients obtained by an expansion of the tip single-electron wave functions/density of states projected onto the tip-apex atom. The reliability of the model was demonstrated by applying it to two functionalized surfaces where quantum interference effects play an important role in the STM imaging process: N-doped graphene and a magnetic Mn_2H complex on the Ag(111) surface [P6]. I showed that the electronic structure of the tip has a considerable effect on STM images, especially the interference between s and p_z tip orbitals that can cause a significant contrast change in both studied systems, which cannot be captured by the widely used Tersoff-Hamann method [P6]. Moreover, the revised Chen's model turned out to be 25 times faster than the Bardeen method concerning computational time, while maintaining good agreement, thus proved to be a fast and reliable tool for calculating STM images taking into account the electronic structure and local geometry by arbitrary tip orientations [P6].

List of publications

Publications related to the thesis points

- [P1] K. Palotás, **G. Mándi**, L. Szunyogh, “Orbital-dependent electron tunneling within the atom superposition approach: Theory and application to W(110)” *Physical Review B* **86**, 235415/1-11 (2012)
- [P2] **G. Mándi**, N. Nagy, and K. Palotás, “Arbitrary tip orientation in STM simulations: 3D WKB theory and application to W(110)” *Journal of Physics: Condensed Matter* **25**, 445009/1-10 (2013)
- [P3] **G. Mándi** and K. Palotás, “STM contrast inversion of the Fe(110) surface” *Applied Surface Science* **304**, 65-72 (2014)
- [P4] **G. Mándi**, G. Teobaldi, and K. Palotás, “Contrast stability and “stripe” formation in Scanning tunneling Microscopy imaging of highly oriented pyrolytic graphite: The role of STM-tip orientations” *Journal of Physics: Condensed Matter* **26**, 485007/1-11 (2014)
- [P5] **G. Mándi**, G. Teobaldi, and K. Palotás, “What is the orientation of the tip in a scanning tunneling microscope?” *Progress in Surface Science* **90**, 223–238 (2015)
- [P6] **G. Mándi** and K. Palotás, “Chen’s derivative rule revisited: Role of tip-orbital interference in STM” *Physical Review B* **91**, 165406/1-12 (2015)

Other publications

- [P7] K. Palotás, **G. Mándi**, and W. A. Hofer, “Three-dimensional Wentzel-Kramers-Brillouin approach for the simulation of scanning tunneling microscopy and spectroscopy” *Frontiers of Physics* **9**, 711-747 (2014)
- [P8] K. Palotás, **G. Mándi**, L. Szunyogh, “Enhancement of the spin transfer torque efficiency in magnetic STM junctions” *Physical Review B* **94**, 064434/1-13 (2016)

Bibliography

- [1] G. Binnig, H. Rohrer, Ch. Gerber, E. Weibel. Surface studies by scanning tunneling microscopy. *Phys. Rev. Lett.*, 49:57, 1982.
- [2] R. Wiesendanger. Spin mapping at the nanoscale and atomic scale. *Rev. Mod. Phys.*, 81:1495, 2009.
- [3] K. von Bergmann, A. Kubetzka, O. Pietzsch, R. Wiesendanger. Interface-induced chiral domain walls, spin spirals and skyrmions revealed by spin-polarized scanning tunneling microscopy. *J. Phys.: Condens. Matter*, 26:394002, 2014.
- [4] R. Wiesendanger. Nanoscale magnetic skyrmions in metallic films and multilayers: A new twist for spintronics. *Nat. Rev. Mater.*, 1:16044, 2016.
- [5] K. S. Mali, N. Pearce, S. De Feyter, N. R. Champness. Frontiers of supramolecular chemistry at solid surfaces. *Chem. Soc. Rev.*, 46:2520–2542, 2017.
- [6] J. Winterlin. Scanning tunneling microscopy studies of catalytic reactions. *Advances in Catalysis*, 45:131–206, 2000.
- [7] B. Hulsken, R. Van Hameren, J. W. Gerritsen, T. Khoury, P. Thordarson, M. J. Crossley, A. E. Rowan, R. J. M. Nolte, J. A. A. W. Elemans, S. Speller. Real-time single-molecule imaging of oxidation catalysis at a liquid–solid interface. *Nat. Nanotechnol.*, 2:285–289, 2007.
- [8] D. M. Eigler, E. K. Schweizer. Positioning single atoms with a scanning tunnelling microscope. *Nature*, 344:524–526, 1990.
- [9] M. F. Crommie, C. P. Lutz, D. M. Eigler. Confinement of electrons to quantum corrals on a metal surface. *Science*, 262:218–220, 1993.

- [10] H. Kim, A. Palacio-Morales, T. Posske, L. Rózsa, K. Palotás, L. Szunyogh, M. Thorwart, R. Wiesendanger. Toward tailoring Majorana bound states in artificially constructed magnetic atom chains on elemental superconductors. *Science Advances*, 4:eaar5251, 2018.
- [11] S. N. Kempkes, M. R. Slot, S. E. Freney, S. J. M. Zevenhuizen, D. Vanmaekelbergh, I. Swart, C. M. Smith. Design and characterization of electrons in a fractal geometry. *Nature Physics*, 15:127–131, 2019.
- [12] J. Bardeen. Tunnelling from a many-particle point of view. *Phys. Rev. Lett.*, 6:57–59, 1961.
- [13] J. Tersoff, D.R. Hamann. Theory and application for the scanning tunneling microscope. *Phys. Rev. Lett.*, 50:1998–2001, 1983.
- [14] J. Tersoff, D.R. Hamann. Theory of the scanning tunneling microscope. *Phys. Rev. B*, 31:805–13, 1985.
- [15] C. J. Chen. Tunneling matrix elements in three-dimensional space: The derivative rule and the sum rule. *Phys. Rev. B*, 42:8841–57, 1990.
- [16] N. Mingo, L. Jurczyszyn, F.J. Garcia-Vidal, R. Saiz-Pardo, P.L. De Andres, F. Flores, S.Y. Wu, W. More. Theory of the scanning tunneling microscope: Xe on Ni and Al. *Phys. Rev. B*, 54:2225–35, 1996.
- [17] C. Sirvent, J. G. Rodrigo, S. Vieira, L. Jurczyszyn, N. Mingo, F. Flores. Conductance step for a single-atom contact in the scanning tunneling microscope: Noble and transition metals. *Phys. Rev. B*, 53:16086, 1996.
- [18] J. M. Blanco, C. González, P. Jelínek, J. Ortega, F. Flores, R. Pérez. First-principles simulations of STM images: from tunneling to the contact regime. *Phys. Rev. B*, 70:085405, 2004.
- [19] S. Lounis. Theory of scanning tunneling microscopy. <http://arxiv.org/abs/1404.0961>, 2014.
- [20] N. Lorente, M. Persson. Theory of single molecule vibrational spectroscopy and microscopy. *Phys. Rev. Lett.*, 85:2997, 2000.

- [21] T. Frederiksen, N. Lorente, M. Paulsson, M. Brandbyge. From tunneling to contact: Inelastic signals in an atomic gold junction from first principles. *Phys. Rev. B*, 75:235441, 2007.
- [22] G. Teobaldi, M. Peñalba, A. Arnau, N. Lorente, W. A. Hofer. Including the probe tip in theoretical models of inelastic scanning tunneling spectroscopy: CO on Cu(100). *Phys. Rev. B*, 76:235407, 2007.
- [23] M. Persson. Theory of inelastic electron tunneling from a localized spin in the impulsive approximation. *Phys. Rev. Lett.*, 103:050801, 2009.
- [24] Nicolás Lorente, Jean-Pierre Gauyacq. Efficient spin transitions in inelastic electron tunneling spectroscopy. *Phys. Rev. Lett.*, 103:176601, 2009.
- [25] R. Korytár, N. Lorente, J.-P. Gauyacq. Many-body effects in magnetic inelastic electron tunneling spectroscopy. *Phys. Rev. B*, 85:125434, 2012.
- [26] A. D. Gottlieb, L. Wesoloski. Bardeen’s tunneling theory as applied to scanning tunneling microscopy: a technical guide to the traditional interpretation. *Nanotechnology*, 17:R57, 2006.
- [27] D. Wortmann, S. Heinze, Ph. Kurz, G. Bihlmayer, S. Blügel. Resolving complex atomic-scale spin structures by spin-polarized scanning tunneling microscopy. *Phys. Rev. Lett.*, 86:4132, 2001.
- [28] C. J. Chen. Effect of $m \neq 0$ tip states in scanning tunneling microscopy: The explanation of corrugation reversal. *Phys. Rev. Lett.*, 69:1656–1659, 1992.
- [29] K. Palotás, W. A. Hofer, L. Szunyogh. Simulation of spin-polarized scanning tunneling microscopy on complex magnetic surfaces: Case of a Cr monolayer on Ag(111). *Phys. Rev. B*, 84:174428, 2011.
- [30] K. Palotás, W. A. Hofer, L. Szunyogh. Simulation of spin-polarized scanning tunneling spectroscopy on complex magnetic surfaces: Case of a Cr monolayer on Ag(111). *Phys. Rev. B*, 85:205427, 2012.
- [31] M. Passoni, F. Donati, A. Li Bassi, C. S. Casari, C. E. Bottani. Recovery of local density of states using scanning tunneling spectroscopy. *Phys. Rev. B*, 79:045404, 2009.

- [32] H. Yang, A. R. Smith, M. Prikhodko, W. R. L. Lambrecht. Atomic-scale spin-polarized scanning tunneling microscopy applied to $\text{Mn}_3\text{N}_2(010)$. *Phys. Rev. Lett.*, 89:226101, 2002.
- [33] A. R. Smith, R. Yang, H. Yang, W. R. L. Lambrecht, A. Dick, J. Neugebauer. Aspects of spin-polarized scanning tunneling microscopy at the atomic scale: experiment, theory, and simulation. *Surface Science*, 561:154–170, 2004.
- [34] S. Heinze. Simulation of spin-polarized scanning tunneling microscopy images of nanoscale non-collinear magnetic structures. *Appl. Phys. A*, 85:407, 2006.
- [35] J. H. A. Hagelaar, C. F. J. Flipse, J. I. Cerdá. Modeling realistic tip structures: Scanning tunneling microscopy of NO adsorption on Rh(111). *Phys. Rev. B*, 78:161405, Oct 2008.
- [36] L. Gross, N. Moll, F. Mohn, A. Curioni, G. Meyer, F. Hanke, M. Persson. High-resolution molecular orbital imaging using a p-wave STM tip. *Phys. Rev. Lett.*, 107:086101, 2011.
- [37] B. Siegert, A. Donarini, M. Grifoni. The role of the tip symmetry on the STM topography of π -conjugated molecules. *Phys. Stat. Sol. B*, 250:2444–51, 2013.
- [38] W. A. Hofer. Challenges and errors: interpreting high resolution images in scanning tunneling microscopy. *Prog. Surf. Sci.*, 71:147–83, 2003.
- [39] K. Palotás, W. A. Hofer. Multiple scattering in a vacuum barrier obtained from real-space wavefunctions. *J. Phys.: Condens. Matter*, 17:2705–13, 2005.
- [40] L. Jurczyszyn, B. Stankiewicz. Inter-orbital interference in STM tip during electron tunneling in tip–sample system: influence on STM images. *Progress in Surface Science*, 74:185 – 200, 2003.
- [41] L. Jurczyszyn, B. Stankiewicz. The role of interorbital interference in the formation of STS spectra. *Applied Surface Science*, 242:70 – 81, 2005.

- [42] G. Kresse, J. Furthmüller. Efficient iterative schemes for ab initio total-energy calculations using a plane-wave basis set. *Phys. Rev. B*, 54:11169–86, 1996.
- [43] X. Gonze et al. ABINIT: First-principles approach of materials and nanosystem properties. *Computer Phys. Commun.*, 180:2582–2615, 2009.
- [44] P. Giannozzi et al. QUANTUM ESPRESSO: a modular and open-source software project for quantum simulations of materials. *J. Phys.: Condens. Matter*, 21:395502, 2009.
- [45] S. Heinze, S. Blügel, R. Pascal, M. Bode, R. Wiesendanger. Prediction of bias-voltage-dependent corrugation reversal for STM images of bcc (110) surfaces: W(110), Ta(110), and Fe(110). *Phys. Rev. B*, 58:16432, 1998.
- [46] M. Bode, M. Heide, K. von Bergmann, P. Ferriani, S. Heinze, G. Bihlmayer, A. Kubetzka, O. Pietzsch, S. Blügel, R. Wiesendanger. Chiral magnetic order at surfaces driven by inversion asymmetry. *Nature*, 447:190–193, 2007.
- [47] S. Heinze, X. Nie, S. Blügel, M. Weinert. Electric-field-induced changes in scanning tunneling microscopy images of metal surfaces. *Chem. Phys. Lett.*, 315:167–172, 1999.
- [48] G. Kresse, D. Joubert. From ultrasoft pseudopotentials to the projector augmented-wave method. *Phys. Rev. B*, 59:1758–75, 1999.
- [49] J. P. Perdew, Y. Wang. Accurate and simple analytic representation of the electron-gas correlation energy. *Phys. Rev. B*, 45:13244–49, 1992.
- [50] H. J. Monkhorst, J. D. Pack. Special points for Brillouin-zone integrations. *Phys. Rev. B*, 13:5188–92, 1976.
- [51] G. Teobaldi, E. Inami, J. Kanasaki, K. Tanimura, A.L. Shluger. Role of applied bias and tip electronic structure in the scanning tunneling microscopy imaging of highly oriented pyrolytic graphite. *Phys. Rev. B*, 85:085433, 2012.
- [52] M. Ondracek, C. Gonzalez, P. Jelinek. Reversal of atomic contrast in scanning probe microscopy on (111) metal surfaces. *J. Phys.: Condens. Matter*, 24:084003, 2012.

- [53] R. Yang, H. Yang, A. R. Smith, A. Dick, J. Neugebauer. Energy-dependent contrast in atomic-scale spin-polarized scanning tunneling microscopy of $\text{Mn}_3\text{N}_2(010)$: experiment and first-principles theory. *Phys. Rev. B*, 74:115409, 2006.
- [54] K. Palotás. Prediction of the bias voltage dependent magnetic contrast in spin-polarized scanning tunneling microscopy. *Phys. Rev. B*, 87:024417, 2013.
- [55] W. A. Hofer, K. Palotás, S. Rusponi, T. Cren, H. Brune. Role of hydrogen in giant spin polarization observed on magnetic nanostructures. *Phys. Rev. Lett.*, 100:026806, 2008.
- [56] D. E. Jiang, E. A. Carter. Adsorption and diffusion energetics of hydrogen atoms on Fe(110) from first principles. *Surface Science*, 547:85–98, 2003.
- [57] P. Ferriani, C. Lazo, S. Heinze. Origin of the spin polarization of magnetic scanning tunneling microscopy tips. *Phys. Rev. B*, 82:054411, 2010.
- [58] J. Kanasaki, E. Inami, K. Tanimura, H. Ohnishi, K. Nasu. Formation of sp^3 -bonded carbon nanostructures by femtosecond laser excitation of graphite. *Phys. Rev. Lett.*, 102:087402, 2009.
- [59] K. S. Novoselov, V. I. Fal’ko, L. Colombo, P. R. Gellert, M. G. Schwab, Kim K. A roadmap for graphene. *Nature*, 490:192–200, 2012.
- [60] D. Jariwala, V. K. Sangwan, L. J. Lauhon, T. J. Marks, M. C. Hersam. Carbon nanomaterials for electronics, optoelectronics, photovoltaics and sensing. *Chem. Soc. Rev.*, 42:2824–60, 2013.
- [61] U. N. Maiti, W. J. Lee, J. M. Lee, Y. Oh, J. Y. Kim, J.E. Kim, J. Shim, T. H. Han, S. O. Kim. 25th anniversary article: chemically modified/doped carbon nanotubes and graphene for optimized nanostructures and nanodevices. *Adv. Mater.*, 26:40–67, 2014.
- [62] Y. X. Liu, X. C. Dong, P. Chen. Biological and chemical sensors based on graphene materials. *Chem. Soc. Rev.*, 41:2283–07, 2012.

- [63] A. P. Pandey, K. P. Karande, M. P. More, S. G. Gattani, P. K. Deshmukh. Graphene based nanomaterials: diagnostic applications. *J. Biomed. Nanotechnol.*, 10:179–204, 2014.
- [64] L. Tapasztó, G. Dobrik, P. Lambin, L. P. Biró. Tailoring the atomic structure of graphene nanoribbons by scanning tunnelling microscope lithography. *Nat. Nanotechnol.*, 3:397–401, 2008.
- [65] J. Otsuki. STM studies on porphyrins. *Coord. Chem. Rev.*, 254:2311–41, 2010.
- [66] S. Ayissi, P. A. Charpentier, N Farhangi, J. A. Wood, K. Palotás, W. A. Hofer. Interaction of titanium oxide nanostructures with graphene and functionalized graphene nanoribbons: a DFT study. *J. Phys. Chem. C*, 117:25424–32, 2013.
- [67] M. Ruben, J. M. Lehn, P. Müller. Addressing metal centres in supramolecular assemblies. *Chem. Soc. Rev.*, 35:1056–67, 2006.
- [68] H. Hövel, I. Barke. Morphology and electronic structure of gold clusters on graphite: scanning-tunneling techniques and photoemission. *Prog. Surf. Sci.*, 81:53–111, 2006.
- [69] J. Tersoff, N.D. Lang. Tip-dependent corrugation of graphite in scanning tunneling microscopy. *Phys. Rev. Lett.*, 65:1132–5, 1990.
- [70] G. Binnig, H. Fuchs, C. Gerber, H. Rohrer, E. Stoll, E. Tosatti. Energy-dependent state-density corrugation of a graphite surface as seen by scanning tunneling microscopy. *Europhys. Lett.*, 1:31–6, 1986.
- [71] S. I. Park, C. F. Quate. Tunneling microscopy of graphite in air. *Appl. Phys. Lett.*, 48:112–4, 1986.
- [72] J. I. Paredes, A. Martínez-Alonso, J. M. D. Tascón. Triangular versus honeycomb structure in atomic-resolution STM images of graphite. *Carbon*, 39:476–9, 2001.
- [73] Y. Wang, Y. Ye, K. Wu. Simultaneous observation of the triangular and honeycomb structures on highly oriented pyrolytic graphite at room temperature: an STM study. *Surface Science*, 600:729–34, 2006.

- [74] A. N. Chaika, S.S. Nazin, V. N. Semenov, S. I. Bozhko, O. Lübben, S. A. Krasnikov, K. Radican, I. V. Shvets. Selecting the tip electron orbital for scanning tunneling microscopy imaging with sub-ångström lateral resolution. *EPL*, 92:46003, 2010.
- [75] A. N. Chaika, S.S. Nazin, V. N. Semenov, N. N. Orlova, S. I. Bozhko, O. Lübben, S. A. Krasnikov, K. Radican, I. V. Shvets. High resolution STM imaging with oriented single crystalline tips. *Applied Surface Science*, 267:219–23, 2013.
- [76] M. Ondráček, P. Pou, V. Rozsival, C. González, P. Jelínek, R. Pérez. Forces and currents in carbon nanostructures: Are we imaging atoms? *Phys. Rev. Lett.*, 106:176101, 2011.
- [77] L. Tapasztó, G. Dobrik, P. Nemes-Incze, G. Vertesy, Ph. Lambin, L. P. Biró. Tuning the electronic structure of graphene by ion irradiation. *Phys. Rev. B*, 78:233407, 2008.
- [78] L. Tapasztó, T. Dumitrică, S. J. Kim, P. Nemes-Incze, C. Hwang, L. P. Biró. Breakdown of continuum mechanics for nanometre-wavelength rippling of graphene. *Nature Physics*, 8:739–742, 2012.
- [79] P. Nemes-Incze, Z. Osváth, K. Kamarás, L. P. Biró. Anomalies in thickness measurements of graphene and few layer graphite crystals by tapping mode atomic force microscopy. *Carbon*, 46:1435–1442, 2008.
- [80] P. Simonis, C. Goffaux, P. A. Thiry, L. P. Biro, Ph. Lambin, V. Meunier. Stm study of a grain boundary in graphite. *Surface Science*, 511:319–322, 2002.
- [81] L. P. Biró, Ph. Lambin. Nanopatterning of graphene with crystallographic orientation control. *Carbon*, 48:2677–2689, 2010.
- [82] G. Zs. Magda, X. Jin, I. Hagymási, P. Vancsó, Z. Osváth, P. Nemes-Incze, C. Hwang, L. P. Biró, L. Tapasztó. Room-temperature magnetic order on zigzag edges of narrow graphene nanoribbons. *Nature*, 514:608–611, 2014.
- [83] M. Wasniowska, S. Schröder, P. Ferriani, S. Heinze. Real space observation of spin frustration in Cr on a triangular lattice. *Phys. Rev. B*, 82:012402, 2010.

- [84] J. P. Perdew, K. Burke, M. Ernzerhof. Generalized gradient approximation made simple. *Phys. Rev. Lett.*, 77:3865–68, 1996.
- [85] G. Kresse, J. Furthmüller. Efficiency of ab-initio total energy calculations for metals and semiconductors using a plane-wave basis set. *Comput. Mater. Sci.*, 6:15–50, 1996.
- [86] G. Kresse, D. Joubert. From ultrasoft pseudopotentials to the projector augmented-wave method. *Phys. Rev. B*, 59:1758–75, 1999.
- [87] M. Shiraishi, M. Ata. Work function of carbon nanotubes. *Carbon*, 39:1913–7, 2001.
- [88] G. Rodary, J. C. Girard, L. Largeau, C. David, O. Mauguin, Z. Z. Wang. Atomic structure of tip apex for spin-polarized scanning tunneling microscopy. *Appl. Phys. Lett.*, 98:082505, 2011.
- [89] M. Tsukada, K. Kobayashi, N. Isshiki, H. Kageshima. First-principles theory of scanning tunneling microscopy. *Surf. Sci. Rep.*, 13:267–304, 1991.
- [90] H. S. Wong, X. Feng, K. Müllen, N. Chandrasekhar, C. Channel Durkan. Channel selective tunnelling through a nanographene assembly. *Nanotechnology*, 23:095601, 2012.
- [91] I. Suominen, J. Nieminen, R. S. Markiewicz, A. Bansil. Effect of orbital symmetry of the tip on scanning tunneling spectra of $\text{Bi}_2\text{Sr}_2\text{CaCu}_2\text{O}_{8+\delta}$. *Phys. Rev. B*, 84:014528, 2011.
- [92] E. H. da Silva Neto, P. Aynajian, R. E. Baumbach, E. D. Bauer, J. Mydosh, S. Ono, A. Yazdani. Detection of electronic nematicity using scanning tunneling microscopy. *Phys. Rev. B*, 87:161117, 2013.
- [93] M. Telychko, P. Mutombo, M. Ondracek, P. Hapala, F. C. Bocquet, J. Kolorenc, M. Vondracek, P. Jelinek, M. Svec. Achieving high-quality single-atom nitrogen doping of Graphene/SiC(0001) by ion implantation and subsequent thermal stabilization. *ACS NANO*, 8:7318–24, 2014.
- [94] T. Sachse, N. Néel, S. Meierott, R. Berndt, W. A. Hofer, J. Kröger. Electronic and magnetic states of Mn_2 and Mn_2H on Ag(111). *New Journal of Physics*, 16:063021, 2014.

- [95] B. Walls, O. Lübben, K. Palotás, K. Fleischer, K. Walshe, I. V. Shvets. Oxygen vacancy induced surface stabilization: (110) terminated magnetite. *Phys. Rev. B*, 94:165424, 2016.
- [96] Y. Liu, K. Palotas, X. Yuan, T. Hou, H. Lin, Y. Li, S.-T. Lee. Atomistic origins of surface defects in $\text{CH}_3\text{NH}_3\text{PbBr}_3$ perovskite and their electronic structures. *ACS NANO*, 11:2060, 2017.
- [97] R. Turanský, K. Palotás, J. Brndiar, Y. J. Li, Y. Sugawara, I. Štich. Subatomic-scale resolution with spm: Co adatom on $p(2 \times 1)\text{Cu}(110):\text{O}$. *Nanotechnology*, 30:095703, 2019.
- [98] T. Lee, Y.-J. Lee, K. Palotás, G. Lee, C. Stampfl, A. Soon. Polymorphic expressions of ultrathin oxidic layers of Mo on Au(111). *Nanoscale*, 11:6023, 2019.
- [99] J. Neilson, H. Chinkeziyan, H. Phirke, A. Osei-Twumasi, Y. Li, C. Chichiri, J. Cho, K. Palotás, L. Gan, S. J. Garrett, K. C. Lau, L. Gao. Nitrogen-doped graphene on copper: Edge-guided doping process and doping-induced variation of local work function. *J. Phys. Chem. C*, 123:8802, 2019.
- [100] T. T. Ly, T. Lee, S. Kim, Y.-J. Lee, G. Duvjir, K. Jang, K. Palotás, S.-Y. Jeong, A. Soon, J. Kim. Growing ultrathin Cu_2O films on highly crystalline Cu(111): A closer inspection from microscopy and theory. *J. Phys. Chem. C*, 123:12716, 2019.
- [101] F. Cossu, K. Palotás, S. Sarkar, I. Di Marco, A. Akbari. Strain-induced stripe phase in charge-ordered single layer NbSe_2 . *NPG Asia Materials*, 12:24, 2020.
- [102] Á. Szitás, R. Gubó, T. Pásztor, A. P. Farkas, T. Ajtai, L. Óvári, K. Palotás, A. Berkó, Z. Kónya. Adsorption of azobenzene on hexagonal boron nitride nanomesh supported by Rh(111). *J. Phys. Chem. C*, 124:14182, 2020.
- [103] G. Lee, Y.-J. Lee, K. Palotás, T. Lee, A. Soon. Atomic structure and work function modulations in two-dimensional ultrathin CuI films on Cu(111) from first principles. *J. Phys. Chem. C*, 124:16362, 2020.

-
- [104] K. Palotás, L. Rózsa, E. Simon, L. Udvardi, L. Szunyogh. Spin-polarized scanning tunneling microscopy characteristics of skyrmionic spin structures exhibiting various topologies. *Phys. Rev. B*, 96:024410, 2017.
- [105] K. Palotás, L. Rózsa, L. Szunyogh. Theory of high-resolution tunneling spin transport on a magnetic skyrmion. *Phys. Rev. B*, 97:174402, 2018.
- [106] K. Palotás. High-resolution combined tunneling electron charge and spin transport theory of Néel and Bloch skyrmions. *Phys. Rev. B*, 98:094409, 2018.
- [107] K. Palotás, L. Rózsa, E. Simon, L. Szunyogh. Prediction of maximally efficient spin switching of magnetic skyrmionic textures in spin-polarized stm from theoretical calculations. <http://arxiv.org/abs/2005.13266>, 2020.